



Submitted to: JHEP



CERN-PH-EP-2015-032
22nd September 2015

Measurement of charged-particle spectra in Pb+Pb collisions at $\sqrt{s_{\text{NN}}} = 2.76$ TeV with the ATLAS detector at the LHC

The ATLAS Collaboration

Abstract

Charged-particle spectra obtained in Pb+Pb interactions at $\sqrt{s_{\text{NN}}} = 2.76$ TeV and pp interactions at $\sqrt{s} = 2.76$ TeV with the ATLAS detector at the LHC are presented, using data with integrated luminosities of 0.15 nb^{-1} and 4.2 pb^{-1} , respectively, in a wide transverse momentum ($0.5 < p_{\text{T}} < 150$ GeV) and pseudorapidity ($|\eta| < 2$) range. For Pb+Pb collisions, the spectra are presented as a function of collision centrality, which is determined by the response of the forward calorimeters located on both sides of the interaction point. The nuclear modification factors R_{AA} and R_{CP} are presented in detail as a function of centrality, p_{T} and η . They show a distinct p_{T} -dependence with a pronounced minimum at about 7 GeV. Above 60 GeV, R_{AA} is consistent with a plateau at a centrality-dependent value, within the uncertainties. The value is $0.55 \pm 0.01(\text{stat.}) \pm 0.04(\text{syst.})$ in the most central collisions. The R_{AA} distribution is consistent with flat $|\eta|$ dependence over the whole transverse momentum range in all centrality classes.

Measurement of charged-particle spectra in Pb+Pb collisions at $\sqrt{s_{\text{NN}}} = 2.76$ TeV with the ATLAS detector at the LHC

The ATLAS Collaboration

ABSTRACT:

Charged-particle spectra obtained in Pb+Pb interactions at $\sqrt{s_{\text{NN}}} = 2.76$ TeV and pp interactions at $\sqrt{s} = 2.76$ TeV with the ATLAS detector at the LHC are presented, using data with integrated luminosities of 0.15 nb^{-1} and 4.2 pb^{-1} , respectively, in a wide transverse momentum ($0.5 < p_{\text{T}} < 150 \text{ GeV}$) and pseudorapidity ($|\eta| < 2$) range. For Pb+Pb collisions, the spectra are presented as a function of collision centrality, which is determined by the response of the forward calorimeters located on both sides of the interaction point. The nuclear modification factors R_{AA} and R_{CP} are presented in detail as a function of centrality, p_{T} and η . They show a distinct p_{T} -dependence with a pronounced minimum at about 7 GeV. Above 60 GeV, R_{AA} is consistent with a plateau at a centrality-dependent value, within the uncertainties. The value is $0.55 \pm 0.01(\text{stat.}) \pm 0.04(\text{syst.})$ in the most central collisions. The R_{AA} distribution is consistent with flat $|\eta|$ dependence over the whole transverse momentum range in all centrality classes.

Contents

1	Introduction	1
2	The ATLAS detector	3
3	Datasets	4
4	The centrality of Pb+Pb collisions	7
5	Charged-particle track selection	8
5.1	Modelling of track reconstruction parameters	8
5.2	Requiring pointing to the primary vertex	10
5.3	Matching tracks to calorimetric jets	13
5.4	Merging triggered data samples	15
6	Acceptance and efficiency corrections	17
7	Systematic uncertainties	19
7.1	Absolute normalization	20
7.2	Event selection	20
7.3	Track selection	20
7.4	Correction procedure	21
8	Results	22
9	Summary	31

1 Introduction

High-energy heavy-ion (HI) collisions produce a hot and dense matter, the quark-gluon plasma, in which quarks and gluons become deconfined [1–4]. Charged hadrons of high transverse momentum (p_T) are a tool that can be used to study this strongly interacting matter [5, 6]. Since the start of the LHC operation with heavy ions in 2010, it has been possible to study charged-particle production in HI collisions in a new energy regime.

The first results from the LHC experiments showed that jets emerging from the medium created in such collisions have lower energy than expected in the absence of medium effects [7, 8]. The measurement of fully reconstructed jets by the ATLAS experiment revealed that the energy loss of the high-energy partons in the medium, commonly referred to as jet quenching, results in a lower yield of jets at fixed p_T . The yield is suppressed in

central collisions with respect to the yield in pp collisions by factor of two to four [9, 10]. Additional important information about the energy-loss mechanism is provided by the study of jet fragmentation functions [11, 12]. These show an enhancement in the charged-particle fragment yield in central collisions with respect to those measured in the peripheral ones for transverse momentum $p_T \lesssim 4$ GeV, a reduction for $4 \text{ GeV} \lesssim p_T \lesssim 30$ GeV and a small enhancement for $p_T \gtrsim 30$ GeV.

As jets lose energy and the pattern of jet fragmentation is modified in HI collisions, it is expected that the resulting spectrum of hadrons, which originate from parton fragmentation, is also modified. The results from the LHC experiments [13, 14] established that hadron suppression at the LHC is larger than that measured at RHIC [1–4]. At p_T values of 6–7 GeV the suppression reaches a factor of five for nucleus–nucleus collisions at a centre-of-mass energy per nucleon–nucleon pair $\sqrt{s_{NN}} = 200$ GeV and a factor of seven at $\sqrt{s_{NN}} = 2.76$ TeV. Results from the LHC experiments show that the suppression diminishes at higher p_T .

Several theoretical models attempt to describe the behaviour of the data at high p_T [15, 16], using previous measurements by ALICE and CMS; however the behaviour above $p_T \approx 50$ GeV is not strongly constrained by the data. An attempt was made to predict the behaviour of the suppression at a fixed p_T as a function of rapidity [17], but such dependence has not yet been measured. The ATLAS tracking system has a wide rapidity coverage and thus allows to measure this pseudorapidity dependence.

The suppression of hadron production in HI collisions can be quantified using the nuclear modification factor (R_{AA}), a ratio of the measured charged-particle production yield in HI collisions to the expected rate based on the charged-particle production in nucleon–nucleon collisions. Collisions with complete nuclear overlap are called central collisions, and as the distance between nuclear centres increases, the collisions become more and more peripheral. The hard scattering rate is higher in more central collisions because of greater nuclear overlap where more nucleons in one nucleus can hard-scatter with nucleons in the other. Such an enhancement is expected by the Glauber model to be proportional to the product of nucleon densities in the transverse plane; the ratio is corrected for this by $\langle T_{AA} \rangle$, which is estimated as the number of nucleon–nucleon collisions over their cross section [18]. Neglecting isospin effects, the nucleon–nucleon hadron-production cross section can be approximated by the corresponding pp cross section, $\sigma_{NN} \approx \sigma_{pp}$, and thus the nuclear modification factor can be expressed as

$$R_{AA} = \frac{1}{\langle T_{AA} \rangle} \frac{1/N_{\text{evt}} d^2N_{\text{Pb+Pb}}/d\eta dp_T}{d^2\sigma_{pp}/d\eta dp_T}, \quad (1.1)$$

where N_{evt} is the number of Pb+Pb events, $d^2N_{\text{Pb+Pb}}/d\eta dp_T$ is the differential yield of charged particles in Pb+Pb collisions and $d^2\sigma_{pp}/d\eta dp_T$ is the differential charged-particle production cross section measured in pp collisions. It is expected that in the absence of nuclear effects, the ratio R_{AA} will be unity in the region of p_T where hadron production is dominated by hard scattering processes.

The modifications of the particle spectra can also be studied using the nuclear modification factor R_{CP} , defined as the ratio of the charged-particle yield in each centrality class

to the yield in a chosen peripheral class, both scaled by their corresponding $\langle T_{AA} \rangle$. The nuclear modification factor R_{CP} is defined as

$$R_{CP}(p_T, \eta) = \frac{\langle T_{AA,P} \rangle}{\langle T_{AA,C} \rangle} \frac{1/N_{\text{evt},C}}{1/N_{\text{evt},P}} \frac{d^2 N_{\text{Pb+Pb},C}/d\eta dp_T}{d^2 N_{\text{Pb+Pb},P}/d\eta dp_T}, \quad (1.2)$$

where indices P and C denote quantities obtained in peripheral collisions and for a given centrality, respectively. Measuring R_{CP} is another way to examine the suppression of hadron production in HI collisions.

This paper presents a high-statistics measurement of charged-hadron spectra, R_{AA} and R_{CP} in the transverse momentum range $0.5 < p_T < 150$ GeV in Pb+Pb collisions using data recorded by the ATLAS experiment in the 2010 and 2011 HI physics runs of the LHC at $\sqrt{s_{NN}} = 2.76$ TeV, and the pp data at the same value of \sqrt{s} recorded in the 2011 and 2013 physics runs. The total integrated luminosity of the combined Pb+Pb sample is 0.15 nb^{-1} , and that of the combined pp sample is 4.2 pb^{-1} .

2 The ATLAS detector

The measurements presented in this paper were performed using the ATLAS inner detector (ID), calorimeter, muon spectrometer, and the high-level trigger and data acquisition systems [19]. The ID measures charged-particle tracks within the pseudorapidity¹ interval $|\eta| < 2.5$ using a combination of silicon pixel detectors (Pixel), silicon microstrip detectors (SCT), and a straw tube transition radiation tracker (TRT), all immersed inside a 2 T axial magnetic field. All three tracker systems are composed of a barrel and two symmetrically placed end-cap sections. The Pixel is composed of three layers of sensors with nominal pixel size $50 \mu\text{m} \times 400 \mu\text{m}$. The SCT barrel section contains four layers of double-sided modules with $80 \mu\text{m}$ pitch sensors, while the end-caps consist of nine layers of double-sided modules with radial strips having a mean pitch of $80 \mu\text{m}$. The two sides of each layer in both the barrel and the end-caps have a relative stereo angle of 40 mrad. The TRT contains up to 73 (160) layers of staggered straws interleaved with fibers (foils) in the barrel (end-cap). Charged particles in the barrel region with $p_T \gtrsim 0.5$ GeV and $|\eta| < 1.0$ typically traverse 3 layers of silicon pixel detectors, 4 layers of double-sided microstrip modules, and 36 straws.

The calorimeter system consists of a liquid argon (LAr) electromagnetic (EM) calorimeter covering $|\eta| < 3.2$, a steel-scintillator sampling hadronic calorimeter covering $|\eta| < 1.7$, two LAr hadronic calorimeters covering $1.5 < |\eta| < 3.2$, and two LAr forward calorimeters (FCal) covering $3.1 < |\eta| < 4.9$. The two FCal modules are composed of tungsten and copper absorbers with LAr as the active medium, which together provide ten interaction lengths of material. The hadronic calorimeter has three sampling layers longitudinal in shower depth in $|\eta| < 1.7$ and four sampling layers in $1.5 < |\eta| < 3.2$, with a slight overlap

¹ATLAS uses a right-handed coordinate system with its origin at the nominal interaction point (IP) in the centre of the detector and the z -axis along the beam pipe. The x -axis points from the IP to the centre of the LHC ring, and the y -axis points upward. Cylindrical coordinates (r, ϕ) are used in the transverse plane, ϕ being the azimuthal angle around the beam pipe. The pseudorapidity is defined in terms of the polar angle θ as $\eta = -\ln \tan(\theta/2)$.

of the two regions. It has a $\Delta\eta \times \Delta\phi$ granularity of 0.1×0.1 for $|\eta| < 2.5$ and 0.2×0.2 for $2.5 < |\eta| < 4.9$.² The EM calorimeter is segmented longitudinally in shower depth into three compartments with an additional pre-sampler layer. It has a granularity that varies with layer and pseudorapidity, but which is generally much finer than that of the hadronic calorimeter. The middle sampling layer, in which EM showers typically deposit the largest fraction of their energy, has a granularity of 0.025×0.025 over $|\eta| < 2.5$.

The minimum-bias trigger scintillator (MBTS) counters are located at a distance of 3.56 m along the beamline from the centre of the ATLAS detector and cover $2.1 < |\eta| < 3.9$ on each side. Each MBTS counter consists of 16 scintillator pads. Signals from the pads were used as an input to the trigger system in the 2010 run and the time difference between hits in the two sides of the MBTS was used to select good events in both the 2010 and 2011 runs.

The zero degree calorimeter (ZDC) consists of two arms, positioned at $z = \pm 140$ m from the centre of the ATLAS detector, and detects neutrons and photons with $|\eta| > 8.3$. Signals from the ZDC are used by the trigger systems. The ZDC trigger thresholds were set just below the single-neutron peak on each side.

The selection of events was done in several steps. First, events were required to satisfy a hardware-based level-1 (L1) trigger. The L1 trigger selects events with energy deposition in the calorimeters above a preset level, or events with signals from the ZDC. Such events are further processed by software-based high-level triggers (HLT).

3 Datasets

This analysis uses data from the 2010 and 2011 Pb+Pb data-taking at $\sqrt{s_{\text{NN}}} = 2.76$ TeV and data from the 2011 and 2013 pp data-taking at the same centre-of-mass energy, $\sqrt{s} = 2.76$ TeV. A summary of all data samples used in this analysis is given in table 1.

All 2010 Pb+Pb data were collected with a minimum-bias (MB) trigger. It required a presence of a neutron or photon on either side of the ZDC or presence of a hit in the MBTS on each side of the ATLAS detector.

In the 2011 data-taking, events were recorded with a MB trigger and a jet trigger. The transverse energy measurements used by the trigger system is evaluated at the electromagnetic scale. The MB events were required either to have the transverse energy, E_{T} , in the whole calorimeter exceeding 50 GeV at the L1 trigger or to have an ID track reconstructed in the event in coincidence with the ZDC signals on both sides. For a jet trigger, events were preselected for reconstruction by the HLT if they deposited a transverse energy of $E_{\text{T}} > 10$ GeV in the calorimeters at L1 or if the ZDC produced signals in coincidence on both sides of the detector. Such events were analysed by the HLT using a jet-finding algorithm on calorimeter towers after underlying-event subtraction [20]. All events containing a jet found with the anti- k_t algorithm [21] with radius parameter $R = 0.2$ and with E_{T} , estimated in the trigger system, of at least 20 GeV were accepted. The HLT uses algorithms very similar to those used in the offline jet reconstruction.

²An exception is the third sampling layer which has a segmentation of 0.2×0.1 up to $|\eta| = 1.7$.

Pb+Pb data					
Year	Trigger	Centrality	Recorded	Sampled	NN collisions
2010	MB	0–80%	4.2×10^7	4.2×10^7	1.8×10^{10}
2011	MB	0–80%	4.2×10^7	8.0×10^8	3.4×10^{11}
2011	Jets	0–80%	1.3×10^7	8.0×10^8	3.4×10^{11}
2011	Jets	0–5%	2.5×10^6	5.0×10^7	8.4×10^{10}
2011	Jets	60–80%	3.3×10^6	2.0×10^8	5.3×10^9

<i>pp</i> data				
Year	Trigger	Recorded	Luminosity	Collisions
2011	MB	1.6×10^7	0.2 pb^{-1}	1.3×10^{10}
2011	Jets	6.5×10^7	0.2 pb^{-1}	1.3×10^{10}
2013	MB	5.5×10^6	4.0 pb^{-1}	2.6×10^{11}
2013	Jets	6.8×10^5	4.0 pb^{-1}	2.6×10^{11}

Pb+Pb simulation samples			
Year	Underlying event	Hard scattering	Total events
2010	HIJING	PYTHIA	5×10^6
2011	Data	PYTHIA	2.2×10^7

<i>pp</i> simulation samples		
Year	Hard scattering	Total events
2011	PYTHIA	3.5×10^7
2013	PYTHIA	1.9×10^7

Table 1. Summary of the data and simulation samples used in the analysis. “MB” stands for minimum bias. For Pb+Pb data, the column “Recorded” lists how many events for a given data-taking period, trigger and centrality interval were written to disk. “Sampled” is the total number of events, of which only a fraction were recorded. The “NN collisions” column in Pb+Pb lists the number of binary nucleon–nucleon collisions equivalent to the “Sampled” events based on the Glauber model [18]. For *pp* data, the meaning of the column “Recorded” is analogous. “Luminosity” is the total luminosity for a given run, while “Collisions” gives the equivalent number of proton–proton collisions for that luminosity. For the simulation samples, the tables specify the origin of the underlying event (for the Pb+Pb samples) and the hard scattering event. The last columns sum up the total number of generated events. These events may be further broken down, such as by kinematic selection on the underlying hard scattering (see text).

The *pp* data with $\sqrt{s} = 2.76 \text{ TeV}$ were obtained in two designated runs in 2011 and 2013. In 2011, the MB trigger required a coincidence of MBTS signals. Events selected with the jet trigger in 2011 were required either to satisfy the requirement of MBTS signals in coincidence and a jet with $E_T > 10 \text{ GeV}$ or to have an area of $\Delta\eta \times \Delta\phi = 0.8 \times 0.8$ in the calorimeters with deposited transverse energy more than 10 GeV at L1.

In 2013, the MB trigger required an event to be randomly selected at L1 in filled bunch crossings and a track to be reconstructed in the ID system. Due to a different

trigger menu designed to take advantage of the higher instantaneous luminosity, only a small fraction of MB events was recorded in 2013 compared to 2011. The jet triggers in the 2013 data-taking used different jet E_T thresholds. For the jet-triggered samples with the lowest thresholds, jet $E_T = 10$ GeV and 20 GeV, events were randomly selected by the L1 trigger and then by the HLT using anti- k_t jet algorithm with a radius parameter of $R = 0.4$ and requiring an energy estimate above the corresponding E_T threshold. For the jet-triggered samples with thresholds of $E_T = 40$ GeV and 50 GeV, events at L1 were required to deposit transverse energy above 5 GeV and 10 GeV, respectively, in an area of $\Delta\eta \times \Delta\phi = 0.8 \times 0.8$ in the ATLAS calorimeters. For the jet-triggered samples with thresholds $E_T = 60$ GeV and 75 GeV, events were selected by requiring a transverse energy deposition above 15 GeV at L1. Due to the limited DAQ bandwidth, the jet-triggered samples were recorded with different prescales depending on the E_T threshold, and these prescales were chosen to evolve with the instantaneous luminosity in the LHC fill. The prescale indicates which fraction of events that passed the trigger selection were selected for recording by the data acquisition system.

The integrated luminosities of the pp samples, after application of the event selection criteria, are given in table 1. After accounting for the nuclear thickness, the luminosities in Pb+Pb and pp samples are comparable, as can be seen in the “NN collisions” column.

A Monte Carlo (MC) simulation was used to correct the detector-level charged-particle spectrum for track reconstruction efficiency loss, detector resolution and the contribution of tracks not produced by primary particles. The track reconstruction performance was simulated in the HI environment. The particles were generated by the PYTHIA event generator [22] version 6.423 with parameters chosen according to the so-called AUET2B parameter set (“tune”) [23]. Five samples of $\sqrt{s} = 2.76$ TeV pp hard scattering events were produced in exclusive intervals of transverse momentum of outgoing partons in the $2 \rightarrow 2$ hard scattering process, with boundaries at 17, 35, 70, 140, 280 and 560 GeV. Each PYTHIA event was embedded in the underlying event of a HI collision, which was obtained using different techniques for the 2010 and 2011 data analyses.

In the 2010 data analysis the environment of Pb+Pb collisions was simulated using 10^6 events, the same for all five samples, with $\sqrt{s_{NN}} = 2.76$ TeV. They were produced by the HIJING event generator [24] with default parameters, except that jet quenching was disabled. To simulate the effects of elliptic flow in Pb+Pb collisions, a parameterized centrality-, η - and p_T -dependent $\cos 2\phi$ modulation with randomly selected event plane based on previous ATLAS measurements [25] was imposed on the particles after generation. The detector response in the resulting MC events was evaluated using GEANT4 [26] configured with geometry and digitization parameters matching those of the 2010 Pb+Pb run [27].

In the 2011 data-taking a separate Pb+Pb event sample was recorded which contained approximately 3×10^6 MB events to be used as the underlying events in the MC samples. Approximately 4.3×10^6 hard scattering PYTHIA events (for each of the five different kinematic selections) were overlaid on these data. Thus, the simulations for the 2011 analysis contains an underlying event contribution identical to the data.

The pp simulated events were generated by PYTHIA, using the same tune as for

Pb+Pb, and reconstructed with the detector conditions matching those from the data-taking period. Minimum-bias and hard scattering samples were simulated for both runs. The MB simulation contained 30×10^6 and 2×10^6 events corresponding to 2011 and 2013 runs respectively. The hard scattering samples were produced in several kinematic regions similarly to the HI samples. For the 2013 samples, the kinematic regions were defined using generated leading jet p_T . The total number of events in the hard scattering samples was 5×10^6 and 17×10^6 for 2011 and 2013 conditions, respectively.

4 The centrality of Pb+Pb collisions

The centrality of Pb+Pb collisions is characterized using the total transverse energy ($\sum E_T$) measured at the electromagnetic scale by the FCal [25]. A detailed study based on a Glauber Monte Carlo model [18] using pp data at $\sqrt{s} = 2.76$ TeV estimated the fraction of the total Glauber cross section passing the trigger and the event selection cuts used in this analysis as $f = (98 \pm 2)\%$. Taking into account the visible fraction of the total cross section and using the $\sum E_T$ distribution, the Pb+Pb event sample is divided into different centrality classes, defined by the percentiles shown in table 2. For the measurement of R_{CP} defined in eq. (1.2), the “peripheral” reference class is chosen to be 60–80% while the “central” class refers to the remaining classes of more central collisions.

The mean number of participating nucleons, $\langle N_{\text{part}} \rangle$, as well as T_{AA} are estimated for each centrality class with the same Glauber calculation. The values are shown in table 2, with uncertainties determined by varying the geometric description, as well as the value of f , used in the Glauber calculation. The last column of table 2 shows the ratio of $\langle T_{AA} \rangle$ in each centrality class to that in the most peripheral (60–80%) centrality class.

Centrality	$\langle N_{\text{part}} \rangle$	$\langle T_{AA} \rangle$ [mb $^{-1}$]	$\frac{\langle T_{AA} \rangle}{\langle T_{AA}^{60-80\%} \rangle}$
0–1%	401 ± 1	29.0 ± 0.5	70.2 ± 8.2
0–5%	382 ± 2	26.3 ± 0.4	63.6 ± 7.4
5–10%	330 ± 3	20.6 ± 0.3	49.8 ± 5.6
10–20%	261 ± 4	14.4 ± 0.3	34.9 ± 3.7
20–30%	186 ± 4	8.73 ± 0.26	21.1 ± 2.4
30–40%	129 ± 4	5.05 ± 0.22	12.2 ± 1.0
40–50%	85.6 ± 3.5	2.70 ± 0.17	6.5 ± 0.4
50–60%	53.0 ± 3.5	1.34 ± 0.12	3.2 ± 0.1
60–80%	22.6 ± 2.3	0.41 ± 0.05	

Table 2. Centrality classes used in this analysis. The mean number of participants, $\langle N_{\text{part}} \rangle$, the mean value of nuclear overlap function, $\langle T_{AA} \rangle$, and its ratio to the most peripheral 60–80% centrality class as estimated using a Glauber Monte Carlo model are also presented.

5 Charged-particle track selection

Charged-particle tracks are reconstructed using the ID system in the pseudorapidity region $|\eta| < 2.5$ and over the full azimuth. The minimum p_T of reconstructed tracks in the Pb+Pb samples is 0.5 GeV. The abundance of particles produced in HI collisions results in increased occupancies in the ID subsystems causing a deterioration of the ID tracking performance in the most central HI collisions. The degradation of the tracking performance at high occupancy manifests itself in three different ways: a decrease of the tracking efficiency, a worsening in the track momentum resolution and the reconstruction of fake tracks. Fake tracks are composed of randomly associated hits in the detector layers. These phenomena are discussed in this section.

The analysis of the charged-particle spectra presented in this paper refers to primary charged particles directly produced in the nucleus–nucleus interactions with a mean lifetime greater than 0.3×10^{-10} s, or long-lived charged particles created by subsequent decays of particles with a shorter lifetime [28]. All other particles are considered secondary. Tracks produced by primary and secondary particles are referred to in what follows as primary and secondary tracks, respectively. An exception is made for muons and electrons coming from the decays of W and Z bosons, whose contributions are excluded from the results, as these leptons follow binary scaling [29–32] and they would affect results with different behaviour. Reconstructed tracks arising from a spurious association of detector-layer hits which originate from different particles and result in a reconstructed track are considered to be fake tracks.

In the MC simulation the categorisation of a particle relies on the matching of a reconstructed track to a generated particle. The matching is done based on contributions of generated particles to the hits in the detector layers. A reconstructed track is matched to a generated particle if it contains hits produced primarily by this particle. The matching procedure is explained in ref. [27]. In addition, the reconstructed track p_T is required to be within the range from $0.5p_T^{\text{gen}}$ to $1.5p_T^{\text{gen}}$ to be considered as successfully reconstructed, where p_T^{gen} is the generated transverse momentum of the particle.

5.1 Modelling of track reconstruction parameters

In HI collisions, the occupancies of the three tracking subsystems increase to different degrees. The Pixel detector occupancy is below 1% even in the most central collisions. The corresponding number for the SCT detector is below 10%, while the occupancy in the TRT reaches 90%. To account for the high occupancy in Pb+Pb events, the track reconstruction is configured differently from that in pp collisions [33, 34]. In Pb+Pb reconstruction, a larger weight is assigned to hits in the Pixel and SCT detectors, thus resulting in a procedure more robust against fake track production. All tracks reconstructed in HI collisions are extensions of the track candidates from these two subsystems; TRT-based tracks are not used.

The simulation reasonably reproduces the centrality dependence of the track reconstruction parameters which define the quality of the track. Figure 1 shows the average number of Pixel, SCT and TRT hits and the average number of SCT holes in Pb+Pb

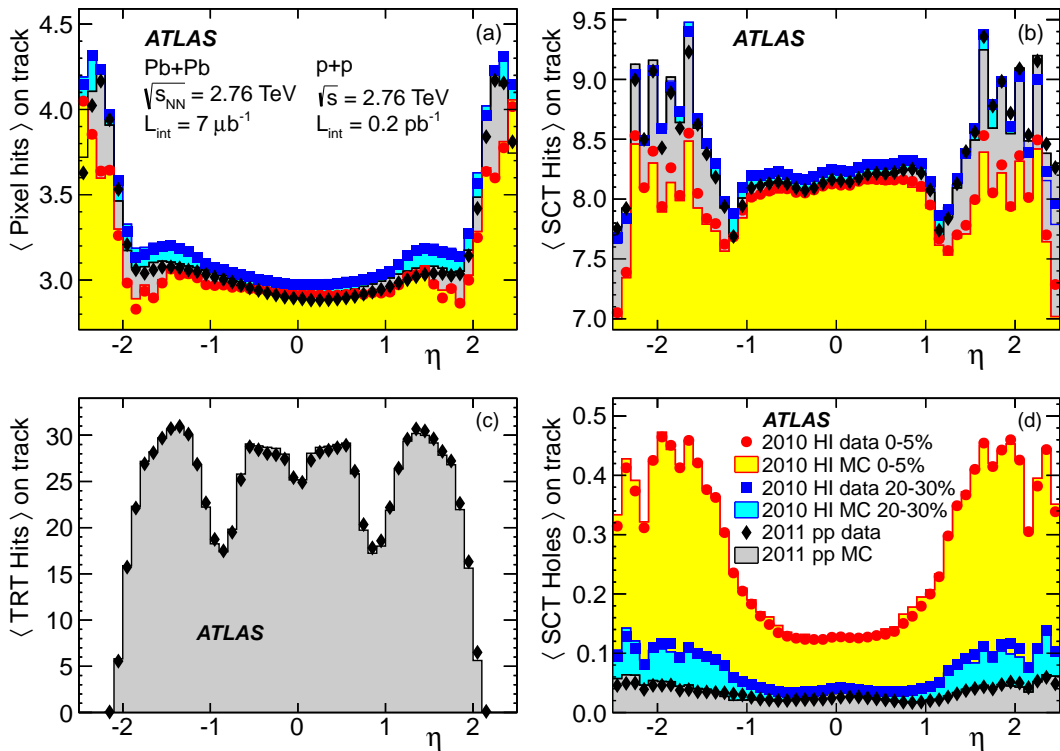


Figure 1. (a) The average number of Pixel hits per track, (b) the average number of SCT hits per track, (c) the average number of TRT hits per track, (d) the average number of SCT holes per track, measured in Pb+Pb events in 0–5% (circles) and 20–30% (squares) centrality classes and in pp events (diamonds) as a function of η . The data from the 2010 Pb+Pb run and 2011 pp runs are compared to the corresponding distributions obtained from simulations shown with filled histograms.

events for the 0–5% and 20–30% centrality classes and in the pp data. An SCT hole is defined by the absence of a hit, predicted by the track trajectory, in a given detector layer. The prediction takes both the detector geometry and the active detector area into account. In HI data processing, tracks with holes in the Pixel detector are rejected at earlier stages by the ID track reconstruction. The number of TRT hits is shown only for the pp data, where it plays the most important role.

All parameters shown in figure 1 are sensitive to the momentum distribution of the tracks; therefore the MC tracks were reweighted in p_T to match the distributions measured in the data. The TRT covers the pseudorapidity interval $|\eta| < 2$, which limits the analysis of the pp data and R_{AA} to this interval, but the TRT hits requirement is necessary to improve track sample purity at high p_T . To avoid possible bias at low p_T , only tracks above p_T of 6 GeV are required to have hits in the TRT. The results with and without such requirement are consistent in the 2–10 GeV interval.

The mean number of Pixel and SCT hits as a function of η shows a relatively weak centrality dependence, whereas the number of SCT holes increases significantly with cent-

Pb+Pb requirements			
	Basic	For systematic uncertainty	
Pixel hits	≥ 2 , BL hit	≥ 1 , BL hit (if exp.)	≥ 3 layers
SCT hits	≥ 7	≥ 6	≥ 8
SCT holes	$=0$		

<i>pp</i> requirements			
	Basic	For systematic uncertainty	
Pixel hits	≥ 1 , BL hit (if exp.)		≥ 2
SCT hits	≥ 6	≥ 5	≥ 7
SCT holes	≤ 1		
TRT hits	≥ 8		≥ 10

Table 3. Track selection criteria for Pb+Pb and *pp* events. “Basic” cuts are used by default in the analysis. Other cuts are used only for estimation of systematic uncertainties. “BL hit” denotes for the requirement of a hit in the innermost pixel layer, so-called B-layer. “BL hit (if exp.)” denotes for the same requirement, but only if such a hit is expected by the track reconstruction algorithm. The TRT hit requirement is applied only to tracks with $p_T > 6$ GeV.

rality. This trend shows the effect of the large occupancy on the SCT pattern-recognition algorithm. A hole on a track may appear if a hit in the SCT is assigned to another track. The fake-track rejection in Pb+Pb collisions requires that there is no hit sharing between tracks. An increased number of SCT holes is an indication of a deterioration of the track quality. Tracks where a SCT hole is present are rejected from the analysis to limit the fake rate.

Tracks are selected for the analysis if they have $p_T > 0.5$ GeV and satisfy all of the quality requirements summarized in table 3. In addition, tracks are required to have $|\eta| < 2.5$ in Pb+Pb samples and $|\eta| < 2.0$ in *pp* samples.

5.2 Requiring pointing to the primary vertex

In Pb+Pb collisions the vertex finding and fitting algorithm [35] provides accurate primary vertex (PV) reconstruction. In the most peripheral collisions used in this analysis, the PV reconstruction precision is better than $20 \mu\text{m}$ in the transverse plane, allowing for efficient separation of tracks that are produced in primary interactions from those that arise from later decays. In more central collisions the PV precision improves inversely proportional to the square root of the number of reconstructed primary tracks in the events. Since the rate of in-time pile-up events in the 0–5% Pb+Pb collisions was less than 5×10^{-3} , only one PV is considered in each event. For each track, the distance of closest approach to the PV is determined in the transverse and longitudinal directions (d_0 and $z_0 \sin \theta$ respectively), along with the errors of these quantities (σ_{d_0} and $\sigma_{z_0 \sin \theta}$) obtained from the covariance matrix of the track fit. They allow for efficient discrimination of tracks arising from secondary particles or tracks with poorly measured p_T .

Figure 2 shows scatter plots of the d_0 parameter versus p_T under different conditions. The distributions of $z_0 \sin \theta$, not shown here, are similar. The widths of the d_0 distributions increase with decreasing p_T due to the increase of multiple scattering. All tracks satisfy the selection criteria listed in section 5.1. Figure 2(a) shows the d_0 versus p_T scatter plot for all tracks in the MB events in the 60–80% centrality interval. The width of the d_0 distribution decreases with increasing transverse momentum of the tracks. At very high p_T it approaches the limit of about $10 \mu\text{m}$ defined by the Pixel detector resolution. At $p_T < 2 \text{ GeV}$ and large $|d_0|$ a significant fraction of tracks originate from weak decays (mainly K_S^0 and Λ^0) inside the pixel detector. At higher p_T , the region with $|d_0|$ exceeding $100 \mu\text{m}$ is unpopulated. The distribution of track parameters shown in figure 2(a) is similar to that in pp collisions, since both systems have relatively low occupancy and thus similar ID tracking performance.

The d_0 distributions in the 0–5% most central collisions, shown in figure 2(b), are different from those in peripheral collisions. In central collisions, the d_0 distribution extends to large values even for high- p_T tracks. To understand the origin of these tracks it is necessary to compare figure 2(b) to a distribution obtained from a sample of events measured under the same occupancy conditions obtained for the jet-triggered sample, shown in figure 2(c).

The tracks included in figure 2(c) satisfy the condition $\Delta R = \sqrt{(\Delta\eta)^2 + (\Delta\phi)^2} < 0.4$, where $\Delta\eta$ and $\Delta\phi$ are the difference in pseudorapidity and azimuthal angle respectively

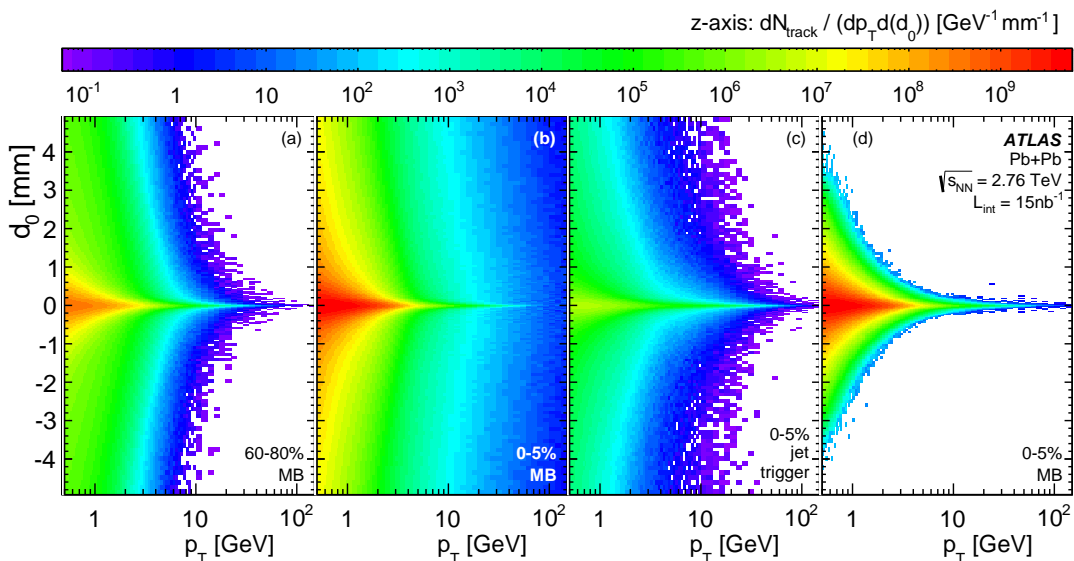


Figure 2. Distance of closest approach of the track trajectory to the PV in the plane transverse to the beam direction, d_0 , (a) in 60–80% peripheral collisions of the MB sample, (b) in 0–5% central collisions of the MB sample, (c) in 0–5% central collisions for the tracks matched to jets in the jet-triggered sample, (d) in 0–5% central collisions of the MB sample after applying cuts on the d_0 and $z_0 \sin \theta$ significances (see text). The z -axis $dN_{\text{track}}/(dp_T dd_0)$ uses a logarithmic scale and is the same for all panels. White areas in the distributions are at least eleven orders of magnitude below the maximum in panel (b).

between the directions of the tracks and the jet axis. Matching tracks to jets is further described in section 5.3. Since most tracks with low p_T are produced via soft interactions, the yield of these tracks is suppressed by the angular matching to jets.

At high p_T , the tracks matched to jets represent a sample with relatively fewer fake tracks compared to the one shown in figure 2(b), which is characterized by the presence of large d_0 values at high p_T . The shape of the d_0 distribution is similar to that seen in peripheral collisions. This leads to the conclusion that in central collisions, tracks populating the region at high p_T and large $|d_0|$ in figure 2(b) are not due to a modification of the d_0 distribution of high- p_T tracks, but rather to mismeasured momentum of low- p_T charged particles caused by increased occupancy in the SCT detector. The d_0 and $z_0 \sin \theta$ parameters of the tracks remain properly measured by the Pixel detector, which has a low occupancy even in most central Pb+Pb collisions.

Accurate estimates of the impact parameter resolution, σ_{d_0} and $\sigma_{z_0 \sin \theta}$, use all hits, including the SCT hits which define the momentum of the track. An overestimated momentum of the track corresponds to a straighter trajectory with lower multiple scattering. The σ_{d_0} and $\sigma_{z_0 \sin \theta}$ for such mismeasured tracks are overestimated with respect to the measured p_T . This effect is seen in figure 3, which shows the average value of the d_0 uncertainty, $\langle \sigma_{d_0} \rangle$, as a function of track p_T , measured in the 0–5% most central collisions. Averaging is done over all tracks in the MB sample. The squares represent all reconstructed tracks. Above p_T of 10 GeV the $\langle \sigma_{d_0} \rangle$ distribution changes very little with p_T due to contamination by tracks from low- p_T charged particles with badly measured p_T . Applying the track selection requirements explained in section 5.1 reduces the average σ_{d_0} as shown by diamond symbols (the same sample as shown in figure 2(b)). At high p_T , $\langle \sigma_{d_0} \rangle$ is still much larger than that for tracks in the jet-triggered sample which are shown with stars.

From these considerations, it can be concluded that the significances, d_0/σ_{d_0} and $z_0 \sin \theta/\sigma_{z_0 \sin \theta}$, for mismeasured tracks from low- p_T particles are much larger than for correctly reconstructed tracks. Rejecting tracks with absolute value of either the transverse or longitudinal impact parameter significance higher than 3.0 from the sample of tracks shown in figure 2(b) produces the scatter-plot presented in figure 2(d). The distribution at high p_T more closely resembles the distribution shown in figure 2(a), except for the low- p_T tracks, where the cuts on the impact parameter significance reject a large fraction of secondary particles. The $\langle \sigma_{d_0} \rangle$ for these tracks, shown with circles in figure 3, is much closer to the values for tracks in jets up to track p_T of 100 GeV and to the results of the MC simulation shown in the figure as a histogram.

Tracks are selected for analysis in Pb+Pb samples if they satisfy the requirements $|d_0|/\sigma_{d_0} < 3.0$ and $|z_0 \sin \theta|/\sigma_{z_0 \sin \theta} < 3.0$. Otherwise tracks are not considered to originate in the primary vertex. In addition $\sigma_{d_0}/\langle \sigma_{d_0} \rangle$ is also required to be < 3.0 .

In pp collisions the PV precision in the transverse plane is about 80 μm for events with 20 tracks and improves to 30 μm for events with 70 tracks [35]. The presence of a jet in an event typically increases the vertex reconstruction precision by contributing tracks. However, using PV pointing cuts similar to those used in the Pb+Pb analysis introduces a correlation between the track selection criteria and the jet multiplicity, which can bias track selection. Therefore, only a loose requirement of $|d_0| < 1.5 \text{ mm}$ is used in the pp track

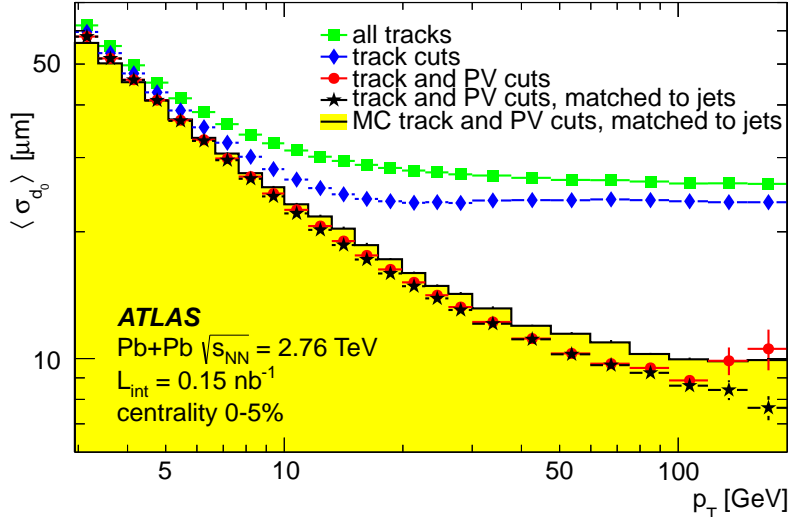


Figure 3. The average uncertainty of the transverse impact parameter, $\langle \sigma_{d_0} \rangle$, as a function of track p_T , measured in the 0–5% central collisions. Squares represent all tracks before applying cuts. Diamonds denote tracks after track selection requirements (section 5.1). The circles, mostly overlapping the stars, are for the tracks satisfying PV pointing requirements, and stars are the same for the tracks also matched to jets above $p_T > 20$ GeV (explained in section 5.3). The filled histogram is the result for the simulated tracks from primary particles plotted as a function of reconstructed track p_T and satisfying the same requirements as in the data.

selection to suppress the contribution of secondary tracks.

5.3 Matching tracks to calorimetric jets

Tracks are required to be matched to jets in order to remove the contribution of fake tracks at high p_T . Calorimetric jets are reconstructed using the anti- k_t algorithm with the radius parameters $R = 0.2, 0.3, 0.4$ and 0.5 . In HI collisions, the jet kinematics are obtained by performing the reconstruction on $\Delta\eta \times \Delta\phi = 0.1 \times 0.1$ towers prior to underlying-event subtraction and then iteratively evaluating and subtracting the estimated underlying-event contribution from each jet at the calorimeter cell level, accounting for the effects of elliptic flow modulation in Pb+Pb collisions [25]. The details of the jet reconstruction in Pb+Pb collisions are described in ref. [20]. The inputs to the jet algorithm are topological clusters of calorimeter cells without a background subtraction procedure, as described in ref. [36]. In both the HI and pp collisions, jets in jet-triggered samples are required to be matched to the online reconstructed jets used by the corresponding jet trigger. This ensures that the tracks correspond to the jets which fired the trigger. No such requirement was used for jets in the MB samples.

High- p_T tracks are produced by particles formed during parton fragmentation to jets, except for those produced by leptons (ℓ) coming from decays of electroweak bosons, primarily $W^\pm \rightarrow \ell^\pm \nu$ and $Z \rightarrow \ell^+ \ell^-$. The contribution of leptons from W and Z decays is removed from the data by identifying tracks corresponding to muons in the ATLAS muon spectrometer and assuming the contribution of electrons is the same. The contribution of

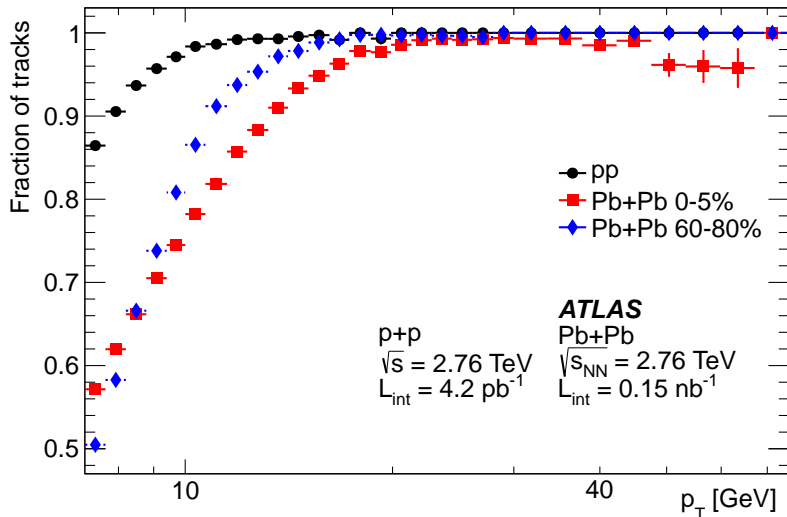


Figure 4. The fraction of tracks in the MB samples, within all tracks in such sample, residing in a cone of size $\Delta R = 0.4$ around the direction of a jet as a function of the track p_T . All tracks satisfy the requirements listed in section 5.1 and 5.2. Circles represent pp data using $R = 0.4$ jets. Squares and diamonds represent Pb+Pb data using $R = 0.2$ jets in the centrality intervals 0–5% and 60–80%, respectively.

leptons is the largest at p_T around 40 GeV and in the most central Pb+Pb collisions where it reaches 5%. The matching of tracks to jets is studied in the data. Figure 4 shows the fraction of tracks, selected by applying the requirements described above, which reside in a cone of size $\Delta R = 0.4$ centred on the jet axis in the Pb+Pb and the pp MB samples. At $p_T < 10$ GeV many tracks cannot be matched to jets due to the limited centrality-dependent reconstruction efficiency for jets with low p_T [37, 38]. At $p_T \gtrsim 15$ GeV all tracks reconstructed in the pp data, shown with circles, reside within the cone around the direction of a jet. In peripheral Pb+Pb collisions, shown with diamond symbols, all tracks with $p_T \gtrsim 20$ GeV are within the cone of a jet. In central collisions, shown with squares, in the same p_T range about 99% of all tracks are found within the cone of a jet; however, above 40 GeV this fraction diminishes due to the contributions of misreconstructed tracks.

Tracks with $p_T > 15$ GeV in pp collisions and $p_T > 20$ GeV in Pb+Pb collisions both in the MB and jet-triggered samples are required to be within a cone of $\Delta R = 0.4$ around the jet direction. The jet is reconstructed with a radius parameter of $R = 0.2$ in Pb+Pb and $R = 0.4$ in pp collisions.

In addition to the requirement of an angular matching, the track p_T is also compared to the E_T of the jet. The track-to-jet energy balance was studied in the MC simulation. The results are sensitive to the description of parton fragmentation in simulation. In Pb+Pb data the jet fragmentation is modified due to medium effects [11] that are not included in the PYTHIA generator. Therefore, the track-to-jet energy balance cut is chosen such that it only rejects very unbalanced pairs of tracks and jets.

The results are shown in figure 5 as a two-dimensional distribution of the track p_T

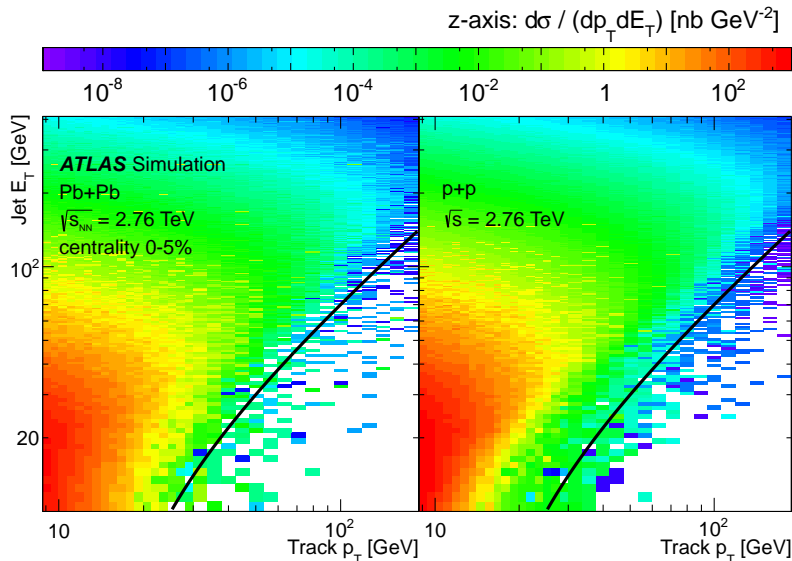


Figure 5. The yield of tracks with reconstructed momentum p_T matched to a jet with measured transverse energy E_T . The left panel shows the Pb+Pb yield divided by $\langle T_{AA} \rangle$ obtained by embedding PYTHIA events into the 0–5% most central Pb+Pb data. The right panel shows the pp cross section as simulated by PYTHIA. Track and jet selections are explained in the text. Lines correspond to the expression $E_T = 0.8 \times p_T - 10 \text{ GeV}$.

versus E_T of the jet in the 0–5% most central Pb+Pb collisions on the left and in pp collisions on the right. The histograms show the E_T of the jet to which the track is matched vs. the track p_T . The reconstructed p_T of the track is typically lower than the measured jet energy, reflecting the fragmentation process. Matches of tracks to jets with E_T less than the track p_T result from the finite resolution of the jet energy measurement or track momentum reconstruction, or from badly reconstructed or fake tracks. The solid line shown in the plot corresponds to $E_T = 0.8 \times p_T - 10 \text{ GeV}$ which was chosen as the cut of the track-to-jet energy balance.

5.4 Merging triggered data samples

The samples obtained with different triggers are combined to construct the spectra, which are equivalent to the unbiased MB spectra and extended to the highest p_T values allowed by the luminosity. This is done separately for each data-taking period. The simulation samples are merged by summing the hard scattering and MB distributions according to their cross sections. The data distributions are corrected using the summed MC samples corresponding to the given run period. After applying corrections described in section 6, the data samples are merged from different running periods.

In the data, tracks with p_T low enough to not require matching to a jet as explained in section 5.3, are taken entirely from the MB samples. They have the proper mixture of all processes presented in the collisions.

Tracks with p_T above the track-to-jet matching requirement are taken from both the MB and jet-triggered samples. These tracks are required to be matched to a jet, including

those from MB samples. Jet-triggered samples are used when the corresponding jet trigger efficiency reaches 90%. Efficiencies of the jet triggers defined with respect to the MB triggers are evaluated in refs. [37, 38]. The jet trigger prescale factor is smaller for triggers with higher thresholds. When a jet trigger with a higher threshold also reaches 90% efficiency its sample is larger than the sample with lower jet threshold, and therefore the use of the jet sample with the lower threshold trigger is discontinued. This procedure guarantees that each track matched to a jet is used only once in all samples, even if the same jet was recorded by more than one trigger.

After correcting for average prescale of each sample, the selected tracks are added to produce a single combined sample as explained above. The contributions of triggered samples to the combined sample are shown in figure 6 for the 2013 pp data. The data are divided by a power-law parameterization to better reveal the contributions from each sample. Open circles around unity depict the combined sample of all tracks. The contribution of the MB sample below the track-to-jet matching p_T threshold (15 GeV), shown with filled circles, coincides with the combined distribution. At higher p_T , the tracks from the MB sample contribute only when they are matched to low-energy jets. This part is also shown with filled circles.

At even higher p_T , tracks come predominantly from the event samples obtained with jet triggers. Their p_T distributions are shown with filled markers; some trigger samples are combined for plot clarity. The contributions from such samples first rise and then decrease, except for the two lowest-threshold trigger samples where only the decrease is

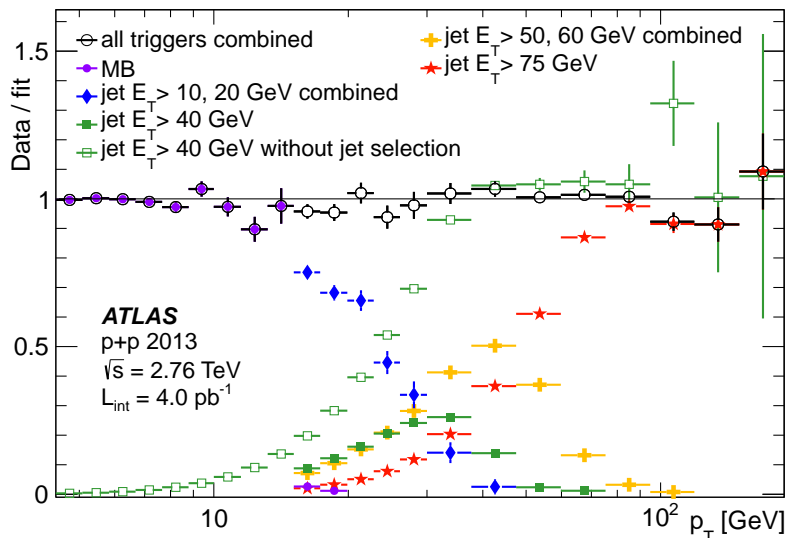


Figure 6. Ratios of the number of tracks from different pp triggered samples to a smooth parameterization (“fit”) describing the combined sample. Open circles show the ratio for the combined sample of all tracks. Filled circles show the MB sample. Other filled markers show the contributions of tracks in jet-triggered samples. Only one sample is used for all jets with the same E_T (see text). Some samples are combined for visibility of the plot. Open squares show the total number of tracks in the sample of the jet trigger $E_T > 40$ GeV.

presented, and for the highest-threshold trigger sample with $E_T > 75$ GeV. Since jets are selected from each trigger only in an exclusive E_T range, the contribution of tracks to the total spectrum rises and falls with E_T . The effect of such a jet trigger interval selection is demonstrated by comparison of closed squares (with selection) and open squares (without selection) corresponding to the jet trigger with E_T threshold of 40 GeV. Without applying a jet trigger interval selection the ratio starts at low p_T at a value significantly below unity. The ratio then rises to unity where it remains flat, consistent with the combined sample of all tracks. However, the statistical uncertainty of the ratio is significantly larger than that for the samples obtained with the higher jet trigger thresholds due to the difference in the integrated luminosity associated with each trigger.

6 Acceptance and efficiency corrections

Corrections to the reconstructed yields in each sample are applied at different stages of the analysis in order to remove detector effects, reconstruction biases and to correct to the particle level. They are derived from data and simulation.

The correction for the fraction of events recorded with different jet and MB triggers is assigned as a weight to each track selected for the analysis. The jet trigger efficiency correction is applied in the same way. The trigger efficiencies are measured in analyses published in refs. [37, 38]. This correction is relatively small, since each jet trigger is used only to select jets for which it is at least 90% efficient. The correction for the MB trigger efficiency in Pb+Pb collisions is negligible in all centrality intervals analysed. In the pp data a correction for the vertex reconstruction efficiency is applied. The vertex reconstruction efficiencies are estimated as a function of number of reconstructed tracks in the same way as in ref. [28]. The correction is very small and reaches unity when four or more tracks are selected within an event. After applying these corrections, samples are merged as described in section 5.4.

After the raw spectra from different triggers are merged, they are corrected for secondary, fake and misreconstructed tracks. The merged spectra are multiplied by the fraction of primary tracks, which is defined as the number of primary tracks divided by the total number of tracks, i.e. including secondary, fake and misreconstructed tracks. The fractions are estimated in the MC simulation for 20 bins in η with a width of 0.25, 9 centrality intervals, and separately for positively and negatively charged particles. They are found to have only a weak dependence on particle charge and the sign of η . However, they are dependent on $|\eta|$ for $|\eta| > 1$. Thus, the corrections were merged into seven $|\eta|$ bins for both charges combined in order to have smaller statistical uncertainty at higher p_T . At low p_T this correction is dominated by secondary particles and reaches 10% at $|\eta| > 2.25$ in the most central Pb+Pb collisions. It decreases at low $|\eta|$ and in more peripheral collisions. In the pp data samples it does not exceed 4% at any measured η . At $p_T > 4$ GeV the contributions of fakes and secondaries do not exceed 1% in any of the samples and remain at this value up to $p_T \approx 70$ GeV. At the highest measured p_T , misreconstructed tracks contribute significantly, as shown in figure 7.

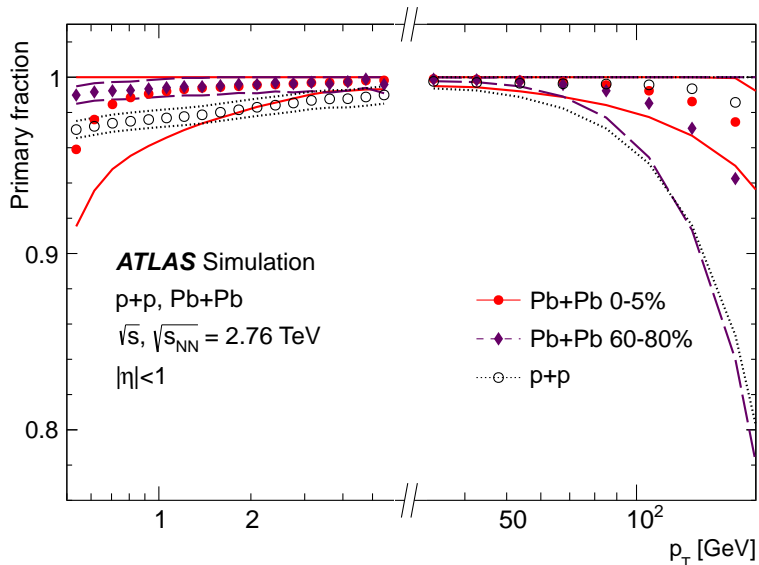


Figure 7. The fraction of reconstructed tracks matched to primary particles for two Pb+Pb centrality classes (solid markers) and pp (open markers) as a function of track p_T . Their systematic uncertainty bands are shown with solid, dashed and dotted lines for Pb+Pb central collisions, peripheral collisions and pp , respectively, and are further discussed in section 7.4.

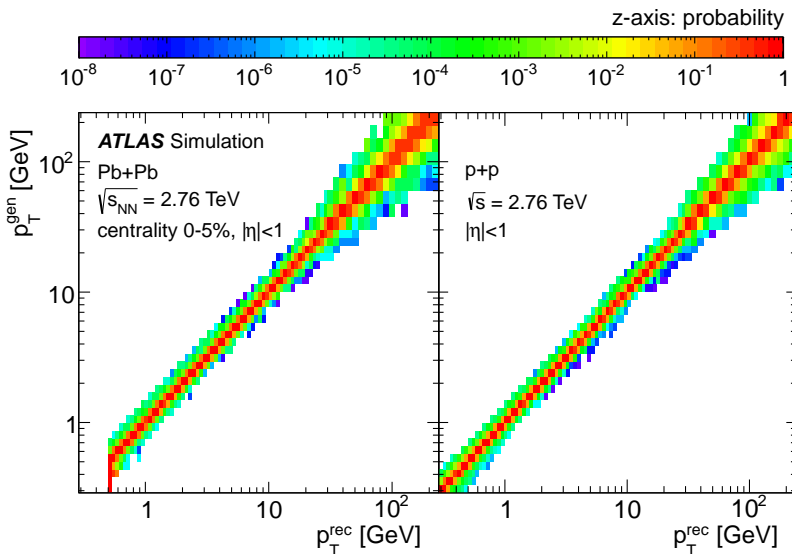


Figure 8. Examples of migrations from generated p_T (p_T^{gen}) to reconstructed p_T (p_T^{rec}) for tracks in the most central collisions in Pb+Pb (left) and for pp (right). The integral of the distribution in each p_T^{gen} bin is normalized to unity.

The spectra are then corrected for the track momentum resolution with an iterative Bayesian unfolding procedure [39]. Results are obtained with two iterations. The migration matrices used are shown in figure 8 as functions of the generated particle transverse momentum (p_T^{gen}) and reconstructed transverse momentum of the associated track (p_T^{rec}).

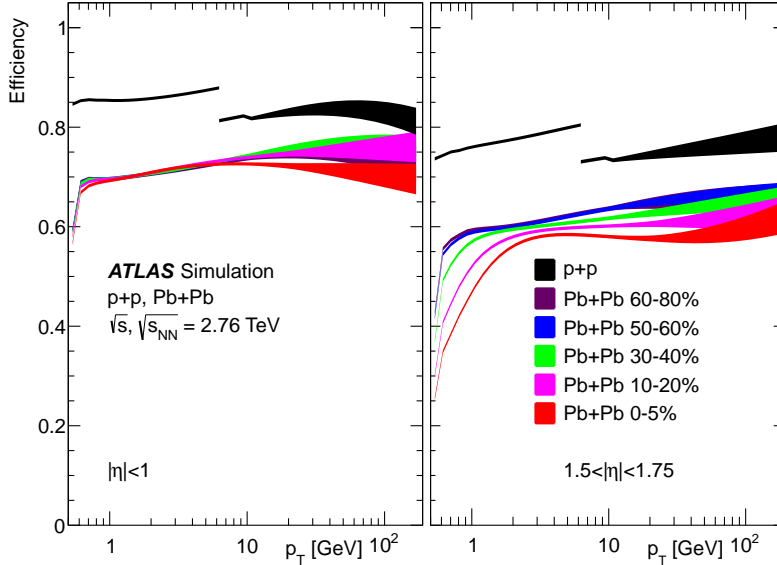


Figure 9. Track reconstruction efficiency as a function of p_T for five centrality classes for Pb+Pb and for pp in two $|\eta|$ regions. The discontinuity of the pp efficiency at 6 GeV is caused by the change in the TRT hit requirements (see section 5.1). The width of the band represents the systematic uncertainty.

The migration matrices are consistent for both particle charges and for the same η ranges as for the primary fraction correction and are therefore combined.

The unfolded spectra are corrected for the reconstruction efficiency using the efficiency estimated in simulation, defined as the number of primary charged particles matched to reconstructed tracks divided by the total number of generated primary particles. The track reconstruction efficiencies are estimated as a function of reconstructed particle p_T , $|\eta|$ and charge. They are found to agree in the same regions as the primary fractions and are also combined for both charges of particles, both sides of $|\eta|$ and for $|\eta| < 1$. The efficiencies are smoothed by fitting to minimize the effect of statistical fluctuations at high p_T in the simulation. A sample of efficiency curves is shown in figure 9.

7 Systematic uncertainties

The systematic uncertainties of the measurements presented in this paper arise from several sources, which are summarized at the end of this section in table 4. Uncertainties related to the absolute normalization of the spectra come from the uncertainties of the integrated luminosity of the pp sample and event selection efficiency in Pb+Pb. The systematic uncertainties related to the event selection include the uncertainties on the jet trigger efficiencies used in the Pb+Pb and pp event samples. Uncertainties related to the selection of tracks include possible differences in the data and in the MC simulation. Finally, there are uncertainties in the determination of the applied corrections.

Systematic uncertainties are evaluated by varying parameters in the analysis for each source and observing the effects on the corrections and yields. Variations are applied

simultaneously to the Pb+Pb and pp data, so that final uncertainties on R_{AA} and R_{CP} properly reflect the correlated changes in the numerator and denominator. The total systematic uncertainties are determined by adding the uncertainties from each source in quadrature.

7.1 Absolute normalization

The uncertainty on the integrated luminosity of the pp samples is 3% and is taken into account in the invariant cross section and in the R_{AA} measurements presented in this paper. It was estimated in a fashion similar to that previously described by ATLAS [40]. The uncertainty on the fraction of events in the MB sample in Pb+Pb collisions is evaluated in ref. [41] to be 2% for both the 2010 and 2011 runs. This uncertainty affects both the boundaries of the centrality intervals and the centrality-related geometric parameters, $\langle T_{AA} \rangle$. The largest effect is in the 90–100% centrality interval, which is not considered in the paper. To avoid double counting in the results presented in this paper, the uncertainty due to the event fraction in the MB sample is included only in the uncertainties of $\langle T_{AA} \rangle$ and $\langle N_{part} \rangle$ as given in table 2.

7.2 Event selection

The uncertainties on the determination of the jet trigger efficiencies in different jet samples in the pp sample are evaluated in the analysis published in ref. [38]. The resulting uncertainty on the spectra from this contribution does not exceed 3%.

In 2011 the Pb+Pb events were recorded if the anti- k_t jet reconstruction algorithm found a jet with radius parameter $R = 0.2$ and $E_T > 20$ GeV after underlying-event subtraction. The trigger efficiency in Pb+Pb events was studied in the inclusive jet analysis published in ref. [37]. This reaches 90% for jets with $E_T > 40$ GeV and has a weak centrality dependence. The systematic uncertainties on the charged-particle spectra related to the jet trigger efficiency uncertainty is 1%, less than in pp , because only one jet trigger was used in the Pb+Pb data-taking.

7.3 Track selection

The uncertainty due to the track selection reflects possible differences in performance of the track reconstruction algorithms in data and in MC simulation. To estimate this uncertainty, the track quality requirements described in section 5.1 and the vertex pointing requirement described in section 5.2 were tightened or loosened in both data and MC simulation. The resulting uncertainty is below 1% at p_T below 10 GeV and rises with increasing p_T , reaching a maximum of 10% at the highest measured p_T for Pb+Pb and 4% for pp collisions.

Fake and secondary particles passing the tracking requirements create a small contamination at low p_T and are accounted for through the primary fraction correction. The uncertainty of this contamination is due to the unknown relative contributions of primary, secondary and fake tracks. The uncertainty is estimated by comparing the fraction of primary tracks, as defined in this paper, to the fraction of tracks with a reconstructed impact parameter consistent with the particle arising from the primary vertex. In central

collisions, the uncertainty is 5% at the lowest measured p_T and decreased to 0.5% at 1 GeV, in all centralities.

The uncertainty due to fake and secondary particles production at high p_T is highly correlated with the uncertainty associated with the procedure for matching generator-level particles to reconstructed tracks. The uncertainty is at most 3% at the highest measured p_T . In table 4, the high- p_T part of the uncertainty on fake and secondary particles is included in the uncertainty of the matching.

7.4 Correction procedure

These uncertainties reflect the possible impact of variations in the derivation of the applied corrections. The uncertainty associated with matching generated particles to reconstructed tracks is correlated with the uncertainty associated with fake and secondary particles at high p_T . The correlated part of the uncertainty was removed. To estimate this systematic uncertainty, generator-level to reconstructed-level matchings in simulation with different requirements were considered. The main contribution comes from additional constraints on the transverse momentum of reconstructed track, with respect to the generated transverse momentum of the particle to which the track is matched. The uncorrelated part of this uncertainty is below 1% up to 50 GeV and then rapidly increases with increasing p_T . At the highest measured p_T , it reaches 20% for Pb+Pb and 15% for pp yields.

The uncertainty associated with the unfolding reflects the need to choose a specific number of iterations to use in the unfolding procedure. It is estimated by changing the number of iterations, and observing the effect on the charged-particle yields. The uncertainty remains less than 1% at low p_T and increases at high p_T where it reaches 8%.

The uncertainty on the p_T resolution reflects possible differences in the distortion of track p_T in MC simulation and data. To estimate this uncertainty, the p_T resolution (the width of the $1 - p_T^{\text{gen}}/p_T^{\text{rec}}$ distribution) was increased to 1.1 times the nominal width. The 10% broadening was estimated from the resolution of muon p_T in the data. The uncertainty is 1% at low p_T , but reaches 20% at very high p_T .

The systematic uncertainty on the efficiency correction has several contributions. The first is the difference in the distributions for different η ranges and both charges before merging, as explained in section 6. This uncertainty is not higher than 2%. The second contribution is from the uncertainty on the particle composition, estimated from comparisons of the relative rates of different identified particles types between simulation and the data measured by the ALICE collaboration [42]. This uncertainty is at most 3%. Both corrections play an important role only at low p_T . The third uncertainty comes from the uncertainty associated with smoothing the track reconstruction efficiency correction at high p_T . This reaches 2% at the highest p_T . The more significant uncertainty at high p_T comes from the uncertainty associated with the cross sections of the MC samples. These were varied, which resulted in an uncertainty of 5% at the highest p_T due to the different acceptance and efficiency corrections of the MC samples.

The systematic uncertainty associated with possible mismodelling of the detector material is 2% for $|\eta| < 1$ and reaches 6% in the highest $|\eta|$ region [28].

In general, the uncertainties associated with individual sources do not exceed 10%. The exceptions are the track momentum resolution, on the fake tracks at high p_T and on the calculation of T_{AA} .

Systematic uncertainties [%]					
Source	Spectra		R_{CP}	R_{AA}	Strongest variation
	Pb+Pb	pp			
Luminosity		3		3	
$\langle T_{AA} \rangle$				1.5–13	centrality
$\langle T_{AA} \rangle / \langle T_{AA}^{60-80\%} \rangle$			3.8–12		centrality
Jet trigger efficiency	1	3	1	3	p_T
Track selection	10	4	10	10	p_T
Fake and secondary tracks	5	0.5	5	5	p_T , centrality
Matching gen – rec	20	15	15	13	p_T
Unfolding	8	2	4	2	p_T
p_T resolution	20	7	14	12	p_T
Efficiency correction	5	1	4	4	p_T , η
Detector material	2–6	2–6			η

Table 4. Maximum values of systematic uncertainties in percent for the charged-particle spectra and the nuclear modification factors R_{CP} and R_{AA} . “Fake and secondary tracks” reflect only the uncertainty at low p_T ; the high- p_T part is included in “Matching gen – rec”.

8 Results

The corrected charged-particle spectra measured in Pb+Pb collisions at $\sqrt{s_{NN}} = 2.76$ TeV are shown in figure 10 for the pseudorapidity range $|\eta| < 2$ and for five centrality intervals: 0–5%, 10–20%, 30–40%, 50–60% and 60–80% in the p_T range 0.5–150 GeV. In figure 11, charged-particle Pb+Pb spectra in the 0–5% centrality interval are shown for eight regions of $|\eta|$. Both figures show the spectra divided by the $\langle T_{AA} \rangle$ of the corresponding centrality interval compared with the charged-particle production cross sections measured in pp collisions at $\sqrt{s} = 2.76$ TeV.

The charged-hadron yields in peripheral Pb+Pb collisions, depicted by diamond markers in figure 10, show a p_T dependence similar to that of pp collisions. Going from peripheral to central collisions, the T_{AA} -scaled Pb+Pb yields increasingly deviate from the pp spectra. This deviation is largest for p_T less than 1 GeV and in the p_T range 3–30 GeV.

Figure 12 shows the nuclear modification factor R_{CP} for four centrality classes (0–5%, 10–20%, 30–40%, 50–60%) with respect to the 60–80% class. The R_{CP} as a function of p_T reaches a minimum of $0.22 \pm 0.03(\text{syst.})$ at $p_T \approx 7$ GeV in the 0–5% centrality class. The statistical uncertainty of the value at the minimum is negligible. The measurement of R_{CP} is restricted to $p_T < 95$ GeV because it is limited by the small sample size in the 60–80% centrality class.

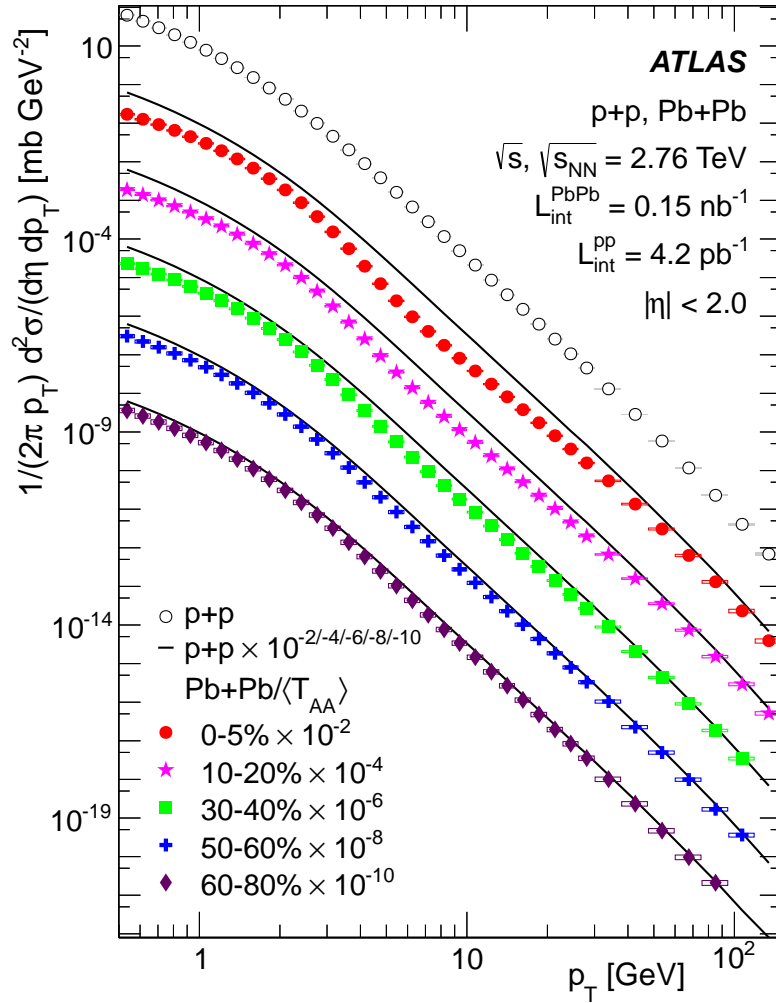


Figure 10. Fully corrected charged-particle transverse momentum spectra for $|\eta| < 2$ shown with filled markers in five centrality intervals: 0–5%, 10–20%, 30–40%, 50–60% and 60–80% as well as the fully corrected charged-particle transverse momentum pp cross section shown by open circles. Statistical uncertainties are smaller than the marker size. Systematic uncertainties are shown by open boxes. The different centrality intervals are scaled down by powers of ten for plot clarity. Each centrality interval is divided by the corresponding $\langle T_{AA} \rangle$ and plotted together with the pp cross section scaled by the same factor shown with solid lines. The total systematic uncertainty on the Pb+Pb spectra includes the uncertainty of $\langle T_{AA} \rangle$.

Figure 13 shows the nuclear modification factor R_{AA} as a function of p_T in five centrality intervals: 0–5%, 10–20%, 30–40%, 50–60% and 60–80% constructed as the ratio of the Pb+Pb to pp distributions from figure 10. Figure 14 shows R_{AA} for 0–5% collisions in eight $|\eta|$ ranges constructed as the ratio of the Pb+Pb to pp distributions from figure 11. The R_{AA} measured as a function of p_T shows a characteristic non-flat p_T shape which becomes more pronounced for more central collisions. They first increase with increasing p_T reaching a maximum at $p_T \approx 2$ GeV, a feature commonly associated with the Cronin

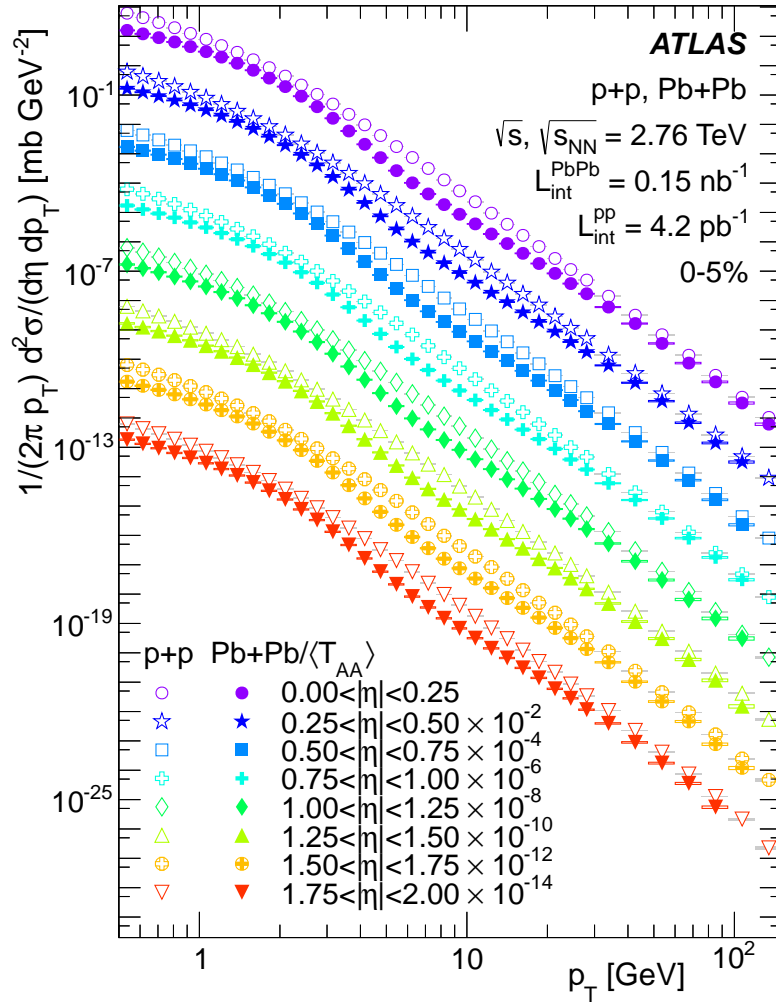


Figure 11. Fully corrected charged-particle transverse momentum spectra produced in eight $|\eta|$ ranges shown with filled markers for the centrality interval 0–5%. Statistical uncertainties are smaller than the marker size. Systematic uncertainties are shown with open boxes. The distributions in different $|\eta|$ intervals are scaled down by powers of ten for plot clarity. Pb+Pb spectra are divided by their corresponding $\langle T_{AA} \rangle$ and plotted together with the cross section measured in pp collisions. These results are shown with open markers of the same style. The total systematic uncertainty of the Pb+Pb spectra includes the uncertainty of $\langle T_{AA} \rangle$.

effect [43]. Then, R_{AA} decreases with higher p_T reaching a minimum at $p_T \approx 7$ GeV, where the charged-particle suppression is strongest. The rate of charged particles is noticeably suppressed even in the 60–80% centrality interval, reaching a minimum of $0.66 \pm 0.09(\text{stat.})$, where the effects of jet quenching are expected to be smallest. The suppression is strongest in the most central 0–5% collisions, where the minimum is $0.14 \pm 0.01(\text{stat.})$. The statistical uncertainties in this p_T region are negligible compared to the systematic uncertainties. Above this p_T , R_{AA} generally increases with increasing p_T up to ≈ 60 GeV and then reaches a plateau, consistent with zero slope, at a value of $0.55 \pm 0.01(\text{stat.}) \pm 0.04(\text{stat.})$ for the

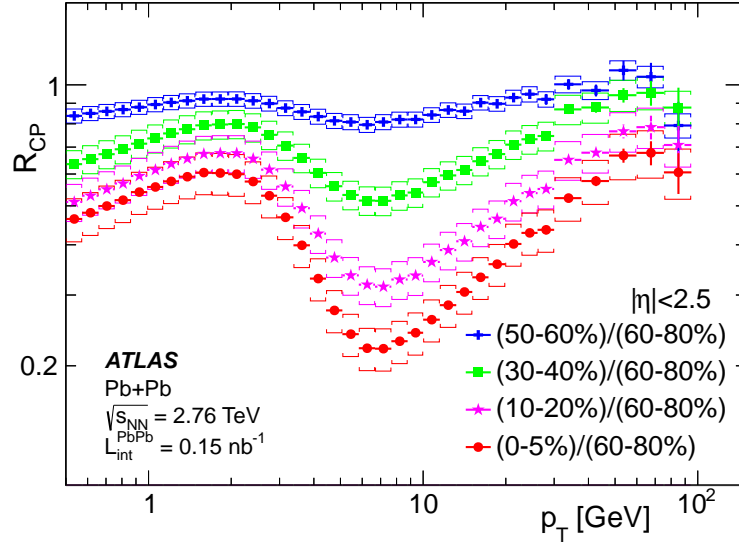


Figure 12. The dependence of the central-to-peripheral nuclear modification factor R_{CP} on p_T measured in the centrality intervals 0–5%, 10–20%, 30–40% and 50–60%. The centrality class 60–80% forms the denominator. Statistical uncertainties are shown with vertical bars and systematic uncertainties with brackets.

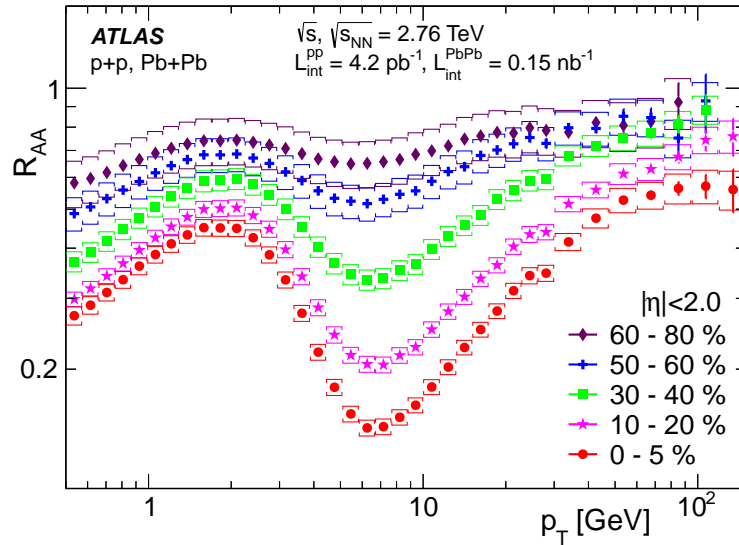


Figure 13. The dependence of the nuclear modification factor R_{AA} on p_T measured in the centrality intervals 0–5%, 10–20%, 30–40%, 50–60% and 60–80%. Statistical uncertainties are shown with vertical bars and systematic uncertainties with brackets.

most central collisions.

The comparison of the R_{AA} values with previous measurements from CMS [13] and ALICE [14] in the most central (0–5%) interval, common to all three experiments, is shown in figure 15. For this comparison the ATLAS R_{AA} values are evaluated in the

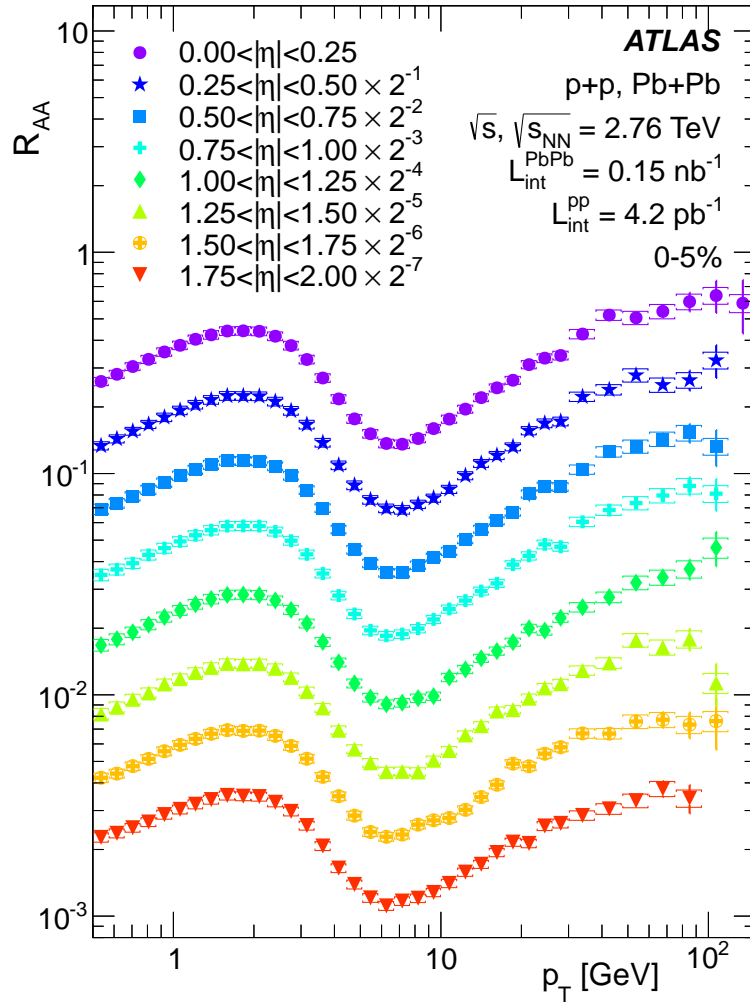


Figure 14. The R_{AA} dependence on p_T measured in eight $|\eta|$ ranges for the centrality interval 0–5%. Statistical uncertainties are shown with vertical bars and systematic uncertainties with brackets. The different $|\eta|$ ranges are scaled down by powers of two for plot clarity.

pseudorapidity interval $|\eta| < 1$, the interval used by the CMS experiment. The ALICE experiment used a similar pseudorapidity interval, $|\eta| < 0.8$. The comparison reveals agreement of the measurements within their uncertainties. In other centrality intervals common to ATLAS and ALICE, the results agree as well. The ATLAS results extend the p_T reach and precision of the previous measurements.

Figure 16 shows R_{AA} as a function of the mean number of participating nucleons, $\langle N_{\text{part}} \rangle$, in the four momentum intervals corresponding to the local *maximum* of R_{AA} in the region $1.7 < p_T < 2.0$ GeV, the local *minimum* in the region $6.7 < p_T < 7.7$ GeV, the *plateau* region $59.8 < p_T < 94.8$ GeV and to the p_T interval where R_{AA} has an *intermediate* magnitude, between the minimum and plateau value, in the region $19.9 < p_T < 22.8$ GeV. In all momentum intervals R_{AA} decreases with $\langle N_{\text{part}} \rangle$, however the decrease is strongest for the *minimum* interval and weakest in the *plateau* region. In the *maximum* and *intermediate*

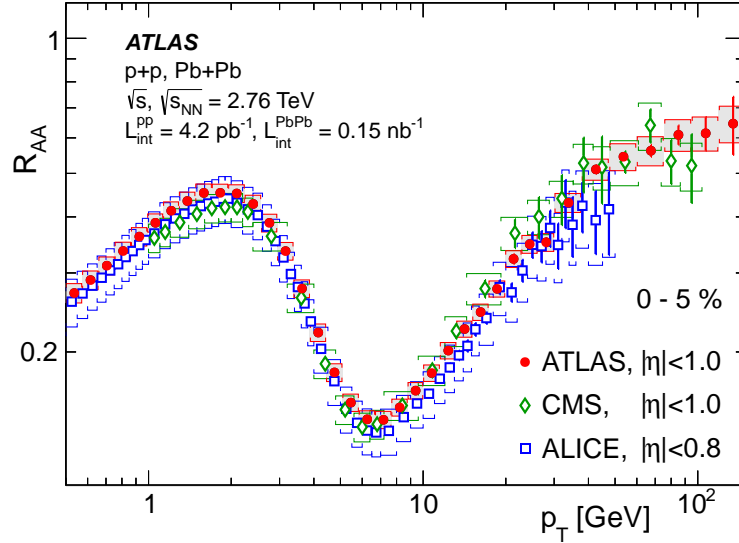


Figure 15. The R_{AA} dependence on p_T measured in the centrality interval 0–5%. The ATLAS (shown as full circles) and CMS results [13] (shown as open diamonds) correspond to the pseudorapidity range $|\eta| < 1$, the ALICE results [14] (open squares) to $|\eta| < 0.8$. Statistical uncertainties are shown with vertical bars and systematic uncertainties with brackets.

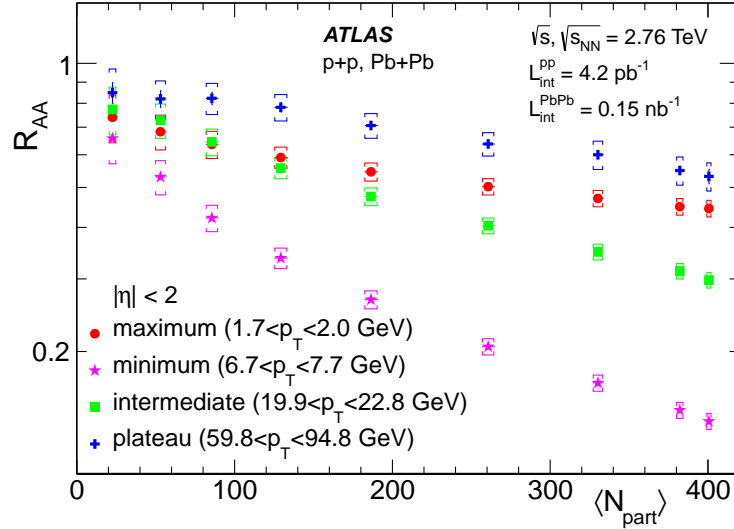


Figure 16. The R_{AA} values plotted as a function of $\langle N_{\text{part}} \rangle$ measured in four transverse momentum intervals corresponding to the *maximum* R_{AA} ($1.7 < p_T < 2.0$ GeV), *minimum* R_{AA} ($6.7 < p_T < 7.7$ GeV), *intermediate* R_{AA} ($19.9 < p_T < 22.8$ GeV) and *plateau* of R_{AA} ($59.8 < p_T < 94.8$ GeV). The statistical uncertainties, which are smaller than the size of markers in all but a few cases, are shown with vertical bars and the systematic uncertainties with brackets.

momentum ranges the R_{AA} values are consistent for $\langle N_{\text{part}} \rangle < 100$, but then deviate at larger $\langle N_{\text{part}} \rangle$. In the most central collisions, R_{AA} in the *maximum* interval is comparable

to that in the *plateau* p_T region. Comparing the *plateau* region to the R_{AA} dependence on $\langle N_{\text{part}} \rangle$ measured with the jets of comparable energy [9], both distributions show similar trend. They have also similar values for peripheral collisions, but in the more central collisions the jet R_{AA} reaches lower values.

To further investigate the nature of the suppression mechanism, the pseudorapidity dependence of R_{AA} was studied. Figure 17 shows the charged-particle cross section in pp collisions and the T_{AA} -scaled yield in Pb+Pb collisions, $d\sigma/d\eta$, measured in the same centrality intervals as the spectra and R_{AA} , integrated over the p_T intervals used to characterize the shape of R_{AA} in figure 16. The $d\sigma/d\eta$ distributions for Pb+Pb, divided by their corresponding $\langle T_{AA} \rangle$, are compared to the pp cross section. The shapes of the Pb+Pb $d\sigma/d\eta$ distributions change slightly within the four specified p_T ranges. At fixed p_T , the shapes agree for different centrality intervals as well as for the pp data.

Figure 18 shows R_{AA} measured in the four defined p_T intervals as a function of pseudorapidity. For all p_T intervals R_{AA} shows little dependence on $|\eta|$ and is generally consistent with a flat behaviour within the statistical and systematic uncertainties.

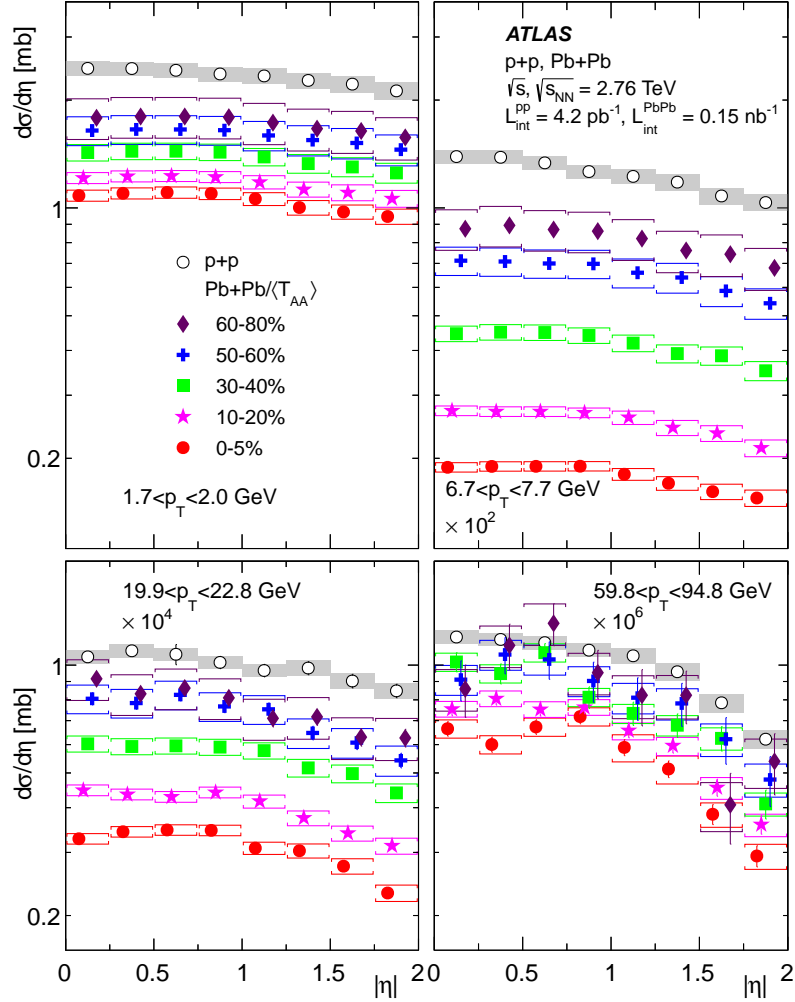


Figure 17. Fully corrected charged-particle pseudorapidity distributions for four transverse momentum intervals defined in the text: *maximum*, *minimum*, *intermediate* and *plateau*. The different p_T ranges are scaled down by powers of ten. Markers are shifted from the centres of the bin for plot clarity. For each p_T range, data are shown in the centrality intervals: 0–5%, 10–20%, 30–40%, 50–60% and 60–80%. The statistical uncertainties, which are typically smaller than the size of markers, are shown with vertical bars and the systematic uncertainties with brackets or grey bands. Pb+Pb spectra are divided by the corresponding $\langle T_{AA} \rangle$ and plotted together with the cross section measured in pp collisions, shown with the open circles. The total systematic uncertainty of the Pb+Pb spectra includes the uncertainty of $\langle T_{AA} \rangle$.

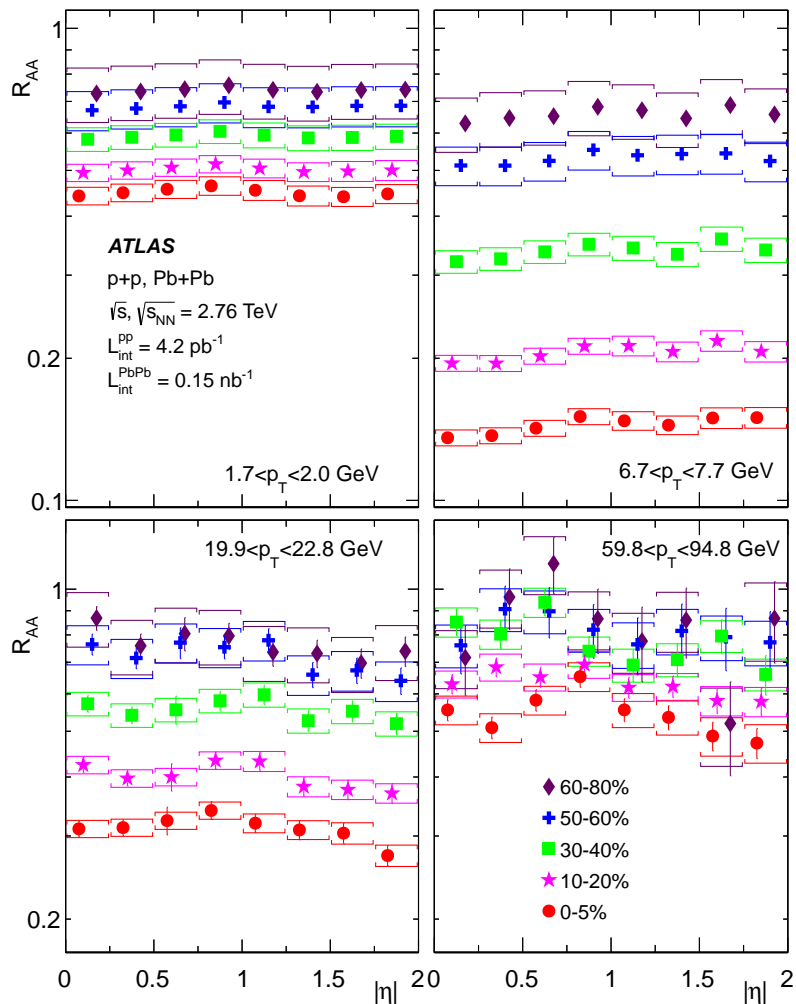


Figure 18. The R_{AA} dependence on η in four transverse momentum intervals defined in the text: *maximum*, *minimum*, *intermediate* and *plateau*. For each p_T range, data are shown in centrality intervals: 0–5%, 10–20%, 30–40%, 50–60% and 60–80%. Statistical uncertainties are shown with vertical bars and systematic uncertainties with brackets. Markers are shifted from the centres of the bin for plot clarity.

9 Summary

A precise measurement of inclusive charged-hadron production in Pb+Pb collisions at $\sqrt{s_{\text{NN}}} = 2.76$ TeV and in pp collisions at $\sqrt{s} = 2.76$ TeV is presented in the p_{T} interval from 0.5 to 150 GeV. The data were collected with the ATLAS detector at the LHC, and correspond to 0.15 nb^{-1} of Pb+Pb collisions and 4.2 pb^{-1} of pp collisions. The results extend those of previous analyses, having a wider reach in p_{T} and increased precision, and they are important input to theoretical calculations.

In all centrality and rapidity intervals studied, the nuclear modification factor, R_{AA} , shows a characteristic shape with a local maximum at $p_{\text{T}} \approx 2$ GeV decreasing to a minimum at $p_{\text{T}} \approx 7$ GeV. It increases again towards higher p_{T} with a change in the slope at $p_{\text{T}} \approx 60$ GeV, where the rise becomes much less steep. Above this p_{T} , the p_{T} dependence is consistent with a flat behaviour within statistical and systematic uncertainties. This shape is present in all measured centrality and pseudorapidity intervals, but it has the largest maximum-to-minimum ratio in the most central collisions. The R_{CP} distribution follows a similar pattern, although the suppression is milder.

For the 0–5% most central collisions R_{AA} reaches a value of $0.14 \pm 0.01(\text{syst.})$ at the minimum. Then R_{AA} increases with increasing p_{T} up to ≈ 60 GeV. Above this p_{T} , R_{AA} is consistent with reaching a plateau at the value of $R_{\text{AA}} = 0.55 \pm 0.01(\text{stat.}) \pm 0.04(\text{syst.})$.

In the individual p_{T} intervals the shape of the charged-hadron pseudorapidity distribution is similar in all Pb+Pb centrality intervals and in the pp data. At fixed p_{T} , the R_{AA} values are consistent with a flat behaviour in $|\eta|$, within the statistical and systematic uncertainties, in the pseudorapidity range $|\eta| < 2$. A similar flat behaviour was found for jet R_{AA} as well [9], although the p_{T} dependence is very different.

The R_{AA} values decrease with increasing $\langle N_{\text{part}} \rangle$ in all measured p_{T} intervals, but the $\langle N_{\text{part}} \rangle$ dependence is strongest around the minimum of R_{AA} ($p_{\text{T}} \approx 7$ GeV) and weakest in the p_{T} region above 60 GeV.

Acknowledgments

We thank CERN for the very successful operation of the LHC, as well as the support staff from our institutions without whom ATLAS could not be operated efficiently.

We acknowledge the support of ANPCyT, Argentina; YerPhI, Armenia; ARC, Australia; BMFWF and FWF, Austria; ANAS, Azerbaijan; SSTC, Belarus; CNPq and FAPESP, Brazil; NSERC, NRC and CFI, Canada; CERN; CONICYT, Chile; CAS, MOST and NSFC, China; COLCIENCIAS, Colombia; MSMT CR, MPO CR and VSC CR, Czech Republic; D NRF, DNSRC and Lundbeck Foundation, Denmark; EPLANET, ERC and NSRF, European Union; IN2P3-CNRS, CEA-DSM/IRFU, France; GNSF, Georgia; BMBF, DFG, HGF, MPG and AvH Foundation, Germany; GSRT and NSRF, Greece; RGC, Hong Kong SAR, China; ISF, MINERVA, GIF, I-CORE and Benoziyo Center, Israel; INFN, Italy; MEXT and JSPS, Japan; CNRST, Morocco; FOM and NWO, Netherlands; BRF and RCN, Norway; MNiSW and NCN, Poland; GRICES and FCT, Portugal; MNE/IFA, Romania; MES of Russia and NRC KI, Russian Federation; JINR; MSTB,

Serbia; MSSR, Slovakia; ARRS and MIZŠ, Slovenia; DST/NRF, South Africa; MINECO, Spain; SRC and Wallenberg Foundation, Sweden; SER, SNSF and Cantons of Bern and Geneva, Switzerland; NSC, Taiwan; TAEK, Turkey; STFC, the Royal Society and Leverhulme Trust, United Kingdom; DOE and NSF, United States of America.

The crucial computing support from all WLCG partners is acknowledged gratefully, in particular from CERN and the ATLAS Tier-1 facilities at TRIUMF (Canada), NDGF (Denmark, Norway, Sweden), CC-IN2P3 (France), KIT/GridKA (Germany), INFN-CNAF (Italy), NL-T1 (Netherlands), PIC (Spain), ASGC (Taiwan), RAL (UK) and BNL (USA) and in the Tier-2 facilities worldwide.

References

- [1] **BRAHMS** Collaboration, I. Arsene et al., *Quark gluon plasma and color glass condensate at RHIC? The Perspective from the BRAHMS experiment*, *Nucl. Phys. A* **757** (2005) 1–27, [[nucl-ex/0410020](#)].
- [2] **PHOBOS** Collaboration, B. Back et al., *The PHOBOS perspective on discoveries at RHIC*, *Nucl. Phys. A* **757** (2005) 28–101, [[nucl-ex/0410022](#)].
- [3] **STAR** Collaboration, J. Adams et al., *Experimental and theoretical challenges in the search for the quark gluon plasma: The STAR Collaboration’s critical assessment of the evidence from RHIC collisions*, *Nucl. Phys. A* **757** (2005) 102–183, [[nucl-ex/0501009](#)].
- [4] **PHENIX** Collaboration, K. Adcox et al., *Formation of dense partonic matter in relativistic nucleus-nucleus collisions at RHIC: Experimental evaluation by the PHENIX collaboration*, *Nucl. Phys. A* **757** (2005) 184–283, [[nucl-ex/0410003](#)].
- [5] D. G. d’Enterria, *High p_T leading hadron suppression in nuclear collisions at $\sqrt{s_{NN}} = 20$ GeV – 200 GeV Data versus parton energy loss models*, *Eur. Phys. J. C* **43** (2005) 295–302, [[nucl-ex/0504001](#)].
- [6] J. Casalderrey-Solana and C. A. Salgado, *Introductory lectures on jet quenching in heavy ion collisions*, *Acta Phys. Polon. B* **38** (2007) 3731–3794, [[arXiv:0712.3443](#)].
- [7] **ATLAS** Collaboration, *Observation of a centrality-dependent dijet asymmetry in lead-lead collisions at $\sqrt{s_{NN}} = 2.76$ TeV with the ATLAS detector at the LHC*, *Phys. Rev. Lett.* **105** (2010) 252303, [[arXiv:1011.6182](#)].
- [8] **CMS** Collaboration, *Observation and studies of jet quenching in PbPb collisions at $\sqrt{s_{NN}} = 2.76$ TeV*, *Phys. Rev. C* **84** (2011) 024906, [[arXiv:1102.1957](#)].
- [9] **ATLAS** Collaboration, *Measurements of the nuclear modification factor for jets in Pb+Pb collisions at $\sqrt{s_{NN}} = 2.76$ TeV with the ATLAS detector*, *Phys. Rev. Lett.* **114** (2015), no. 7 072302, [[arXiv:1411.2357](#)].
- [10] **ALICE** Collaboration, J. Adam et al., *Measurement of jet suppression in central Pb-Pb collisions at $\sqrt{s_{NN}} = 2.76$ TeV*, *Phys. Lett. B* **746** (2015) 1–14, [[arXiv:1502.01689](#)].
- [11] **ATLAS** Collaboration, *Measurement of inclusive jet charged-particle fragmentation functions in Pb+Pb collisions at $\sqrt{s_{NN}} = 2.76$ TeV with the ATLAS detector*, *Phys. Lett. B* **739** (2014) 320–342, [[arXiv:1406.2979](#)].
- [12] **CMS** Collaboration, *Measurement of jet fragmentation in PbPb and pp collisions at $\sqrt{s_{NN}} = 2.76$ TeV*, *Phys. Rev. C* **90** (2014) 024908, [[arXiv:1406.0932](#)].

- [13] **CMS** Collaboration, *Study of high- p_T charged particle suppression in PbPb compared to pp collisions at $\sqrt{s_{\text{NN}}} = 2.76$ TeV*, *Eur. Phys. J. C* **72** (2012) 1945, [[arXiv:1202.2554](#)].
- [14] **ALICE** Collaboration, B. Abelev et al., *Centrality Dependence of Charged Particle Production at Large Transverse Momentum in Pb–Pb Collisions at $\sqrt{s_{\text{NN}}} = 2.76$ TeV*, *Phys. Lett. B* **720** (2013) 52–62, [[arXiv:1208.2711](#)].
- [15] **JET** Collaboration, K. M. Burke et al., *Extracting the jet transport coefficient from jet quenching in high-energy heavy-ion collisions*, *Phys. Rev. C* **90** (2014), no. 1 014909, [[arXiv:1312.5003](#)].
- [16] Z.-B. Kang, R. Lashof-Regas, G. Ovanesyan, P. Saad, and I. Vitev, *Jet quenching phenomenology from soft-collinear effective theory with Glauber gluons*, [arXiv:1405.2612](#).
- [17] T. Renk, *The rapidity dependence of jet quenching*, [arXiv:1406.6784](#).
- [18] M. L. Miller, K. Reygers, S. J. Sanders, and P. Steinberg, *Glauber modeling in high-energy nuclear collisions*, *Ann. Rev. Nucl. Part. Sci.* **57** (2007) 205, [[nucl-ex/0701025](#)].
- [19] **ATLAS** Collaboration, *The ATLAS Experiment at the CERN Large Hadron Collider*, *JINST* **3** (2008) S08003.
- [20] **ATLAS** Collaboration, *Measurement of the jet radius and transverse momentum dependence of inclusive jet suppression in lead-lead collisions at $\sqrt{s_{\text{NN}}} = 2.76$ TeV with the ATLAS detector*, *Phys. Lett. B* **719** (2013) 220–241, [[arXiv:1208.1967](#)].
- [21] M. Cacciari, G. P. Salam, and G. Soyez, *The Anti- $k(t)$ jet clustering algorithm*, *JHEP* **0804** (2008) 063, [[arXiv:0802.1189](#)].
- [22] T. Sjostrand, S. Mrenna, and P. Skands, *PYTHIA 6.4 Physics and Manual*, *JHEP* **0605** (2006) 026, [[hep-ph/0603175](#)].
- [23] **ATLAS** Collaboration, *ATLAS tunes of PYTHIA 6 and Pythia 8 for MC11*, *ATL-PHYS-PUB-2011-009*.
- [24] X.-N. Wang and M. Gyulassy, *HIJING: A Monte Carlo model for multiple jet production in $p+p$, $p+A$ and $A+A$ collisions*, *Phys. Rev. D* **44** (1991) 3501–3516. HIJING version 1.38b with no additional tuning.
- [25] **ATLAS** Collaboration, *Measurement of the pseudorapidity and transverse momentum dependence of the elliptic flow of charged particles in lead-lead collisions at $\sqrt{s_{\text{NN}}} = 2.76$ TeV with the ATLAS detector*, *Phys. Lett. B* **707** (2012) 330–348, [[arXiv:1108.6018](#)].
- [26] **GEANT4** Collaboration, S. Agostinelli et al., *GEANT4: A simulation toolkit*, *Nucl. Ins. Meth. Phys. Res. A* **506** (2003) 250–303.
- [27] **ATLAS** Collaboration, *The ATLAS simulation infrastructure*, *Eur. Phys. J. C* **70** (2010) 823–874, [[arXiv:1005.4568](#)].
- [28] **ATLAS** Collaboration, *Charged-particle multiplicities in pp interactions measured with the ATLAS detector at the LHC*, *New J. Phys.* **13** (2011) 053033, [[arXiv:1012.5104](#)].
- [29] **ATLAS** Collaboration, *Measurement of the production and lepton charge asymmetry of W bosons in Pb+Pb collisions at $\sqrt{s_{\text{NN}}} = 2.76$ TeV with the ATLAS detector*, *Eur. Phys. J. C* **75** (2015) 23, [[arXiv:1408.4674](#)].
- [30] **ATLAS** Collaboration, *Measurement of Z boson Production in Pb+Pb Collisions at $\sqrt{s_{\text{NN}}} = 2.76$ TeV with the ATLAS Detector*, *Phys. Rev. Lett.* **110** (2013) 022301, [[arXiv:1210.6486](#)].

- [31] **CMS** Collaboration, *Study of W boson production in PbPb and pp collisions at $\sqrt{s_{NN}} = 2.76$ TeV*, *Phys. Lett.* **B 715** (2012) 66–87, [[arXiv:1205.6334](#)].
- [32] **CMS** Collaboration, *Study of Z production in PbPb and pp collisions at $\sqrt{s_{NN}} = 2.76$ TeV in the dimuon and dielectron decay channels*, *JHEP* **1503** (2015) 022, [[arXiv:1410.4825](#)].
- [33] **ATLAS** Collaboration, *Charged-particle multiplicities in pp interactions at $\sqrt{s} = 900$ GeV measured with the ATLAS detector at the LHC*, *Phys. Lett.* **B 688** (2010) 21–42, [[arXiv:1003.3124](#)].
- [34] **ATLAS** Collaboration, *Measurement of underlying event characteristics using charged particles in pp collisions at $\sqrt{s} = 900$ GeV and 7 TeV with the ATLAS detector*, *Phys. Rev.* **D 83** (2011) 112001, [[arXiv:1012.0791](#)].
- [35] **ATLAS** Collaboration, *Performance of primary vertex reconstruction in proton-proton collisions at $\sqrt{s} = 7$ TeV in the ATLAS experiment*, *ATLAS-CONF-2010-069*.
- [36] **ATLAS** Collaboration, *Jet energy measurement with the ATLAS detector in proton-proton collisions at $\sqrt{s} = 7$ TeV*, *Eur. Phys. J.* **C 73** (2013) 2304, [[arXiv:1112.6426](#)].
- [37] **ATLAS** Collaboration, *Measurement of the azimuthal angle dependence of inclusive jet yields in Pb+Pb collisions at $\sqrt{s_{NN}} = 2.76$ TeV with the ATLAS detector*, *Phys. Rev. Lett.* **111** (2013) 152301, [[arXiv:1306.6469](#)].
- [38] **ATLAS** Collaboration, *Measurement of the inclusive jet cross section in pp collisions at $\sqrt{s} = 2.76$ TeV and comparison to the inclusive jet cross section at $\sqrt{s} = 7$ TeV using the ATLAS detector*, *Eur. Phys. J.* **C 73** (2013) 2509, [[arXiv:1304.4739](#)].
- [39] G. D’Agostini, *A multidimensional unfolding method based on bayes’ theorem*, *Nucl. Instrum. Meth.* **A 362** (1995) 487.
- [40] **ATLAS** Collaboration, *Improved luminosity determination in pp collisions at $\sqrt{s} = 7$ TeV using the ATLAS detector at the LHC*, *Eur. Phys. J.* **C 73** (2013), no. 8 2518, [[arXiv:1302.4393](#)].
- [41] **ATLAS** Collaboration, *Measurement of the centrality dependence of the charged particle pseudorapidity distribution in lead-lead collisions at $\sqrt{s_{NN}} = 2.76$ TeV with the ATLAS detector*, *Phys. Lett.* **B 710** (2012) 363–382, [[arXiv:1108.6027](#)].
- [42] **ALICE** Collaboration, B. B. Abelev et al., *Production of charged pions, kaons and protons at large transverse momenta in pp and Pb–Pb collisions at $\sqrt{s_{NN}} = 2.76$ TeV*, *Phys. Lett.* **B 736** (2014) 196–207, [[arXiv:1401.1250](#)].
- [43] J. W. Cronin, H. J. Frisch, M. J. Shochet, J. P. Boymond, P. A. Piroué, and R. L. Sumner, *Production of hadrons at large transverse momentum at 200, 300, and 400 GeV*, *Phys. Rev.* **D 11** (Jun, 1975) 3105–3123.

The ATLAS Collaboration

G. Aad⁸⁵, B. Abbott¹¹³, J. Abdallah¹⁵², S. Abdel Khalek¹¹⁷, O. Abdinov¹¹, R. Aben¹⁰⁷, B. Abi¹¹⁴, M. Abolins⁹⁰, O.S. AbouZeid¹⁵⁹, H. Abramowicz¹⁵⁴, H. Abreu¹⁵³, R. Abreu³⁰, Y. Abulaiti^{147a,147b}, B.S. Acharya^{165a,165b,a}, L. Adamczyk^{38a}, D.L. Adams²⁵, J. Adelman¹⁰⁸, S. Adomeit¹⁰⁰, T. Adye¹³¹, T. Agatonovic-Jovin¹³, J.A. Aguilar-Saavedra^{126a,126f}, M. Agustoni¹⁷, S.P. Ahlen²², F. Ahmadov^{65,b}, G. Aielli^{134a,134b}, H. Akerstedt^{147a,147b}, T.P.A. Åkesson⁸¹, G. Akimoto¹⁵⁶, A.V. Akimov⁹⁶, G.L. Alberghi^{20a,20b}, J. Albert¹⁷⁰, S. Albrand⁵⁵, M.J. Alconada Verzini⁷¹, M. Aleksa³⁰, I.N. Aleksandrov⁶⁵, C. Alexa^{26a}, G. Alexander¹⁵⁴, G. Alexandre⁴⁹, T. Alexopoulos¹⁰, M. Alhroob¹¹³, G. Alimonti^{91a}, L. Alio⁸⁵, J. Alison³¹, B.M.M. Allbrooke¹⁸, L.J. Allison⁷², P.P. Allport⁷⁴, A. Aloisio^{104a,104b}, A. Alonso³⁶, F. Alonso⁷¹, C. Alpigiani⁷⁶, A. Altheimer³⁵, B. Alvarez Gonzalez⁹⁰, M.G. Alviggi^{104a,104b}, K. Amako⁶⁶, Y. Amaral Coutinho^{24a}, C. Amelung²³, D. Amidei⁸⁹, S.P. Amor Dos Santos^{126a,126c}, A. Amorim^{126a,126b}, S. Amoroso⁴⁸, N. Amram¹⁵⁴, G. Amundsen²³, C. Anastopoulos¹⁴⁰, L.S. Ancu⁴⁹, N. Andari³⁰, T. Andeen³⁵, C.F. Anders^{58b}, G. Anders³⁰, K.J. Anderson³¹, A. Andreazza^{91a,91b}, V. Andrei^{58a}, X.S. Anduaga⁷¹, S. Angelidakis⁹, I. Angelozzi¹⁰⁷, P. Anger⁴⁴, A. Angerami³⁵, F. Anghinolfi³⁰, A.V. Anisenkov^{109,c}, N. Anjos¹², A. Annovi^{124a,124b}, M. Antonelli⁴⁷, A. Antonov⁹⁸, J. Antos^{145b}, F. Anulli^{133a}, M. Aoki⁶⁶, L. Aperio Bella¹⁸, G. Arabidze⁹⁰, Y. Arai⁶⁶, J.P. Araque^{126a}, A.T.H. Arce⁴⁵, F.A. Arduh⁷¹, J-F. Arguin⁹⁵, S. Argyropoulos⁴², M. Arik^{19a}, A.J. Armbruster³⁰, O. Arnaez³⁰, V. Arnal⁸², H. Arnold⁴⁸, M. Arratia²⁸, O. Arslan²¹, A. Artamonov⁹⁷, G. Artoni²³, S. Asai¹⁵⁶, N. Asbah⁴², A. Ashkenazi¹⁵⁴, B. Åsman^{147a,147b}, L. Asquith¹⁵⁰, K. Assamagan²⁵, R. Astalos^{145a}, M. Atkinson¹⁶⁶, N.B. Atlay¹⁴², B. Auerbach⁶, K. Augsten¹²⁸, M. Auresseau^{146b}, G. Avolio³⁰, B. Axen¹⁵, M.K. Ayoub¹¹⁷, G. Azuelos^{95,d}, M.A. Baak³⁰, A.E. Baas^{58a}, C. Bacci^{135a,135b}, H. Bachacou¹³⁷, K. Bachas¹⁵⁵, M. Backes³⁰, M. Backhaus³⁰, P. Bagiachi^{133a,133b}, P. Bagnaia^{133a,133b}, Y. Bai^{33a}, T. Bain³⁵, J.T. Baines¹³¹, O.K. Baker¹⁷⁷, P. Balek¹²⁹, T. Balestri¹⁴⁹, F. Balli⁸⁴, E. Banas³⁹, Sw. Banerjee¹⁷⁴, A.A.E. Bannoura¹⁷⁶, H.S. Bansil¹⁸, L. Barak¹⁷³, E.L. Barberio⁸⁸, D. Barberis^{50a,50b}, M. Barbero⁸⁵, T. Barillari¹⁰¹, M. Barisonzi^{165a,165b}, T. Barklow¹⁴⁴, N. Barlow²⁸, S.L. Barnes⁸⁴, B.M. Barnett¹³¹, R.M. Barnett¹⁵, Z. Barnovska⁵, A. Baroncelli^{135a}, G. Barone⁴⁹, A.J. Barr¹²⁰, F. Barreiro⁸², J. Barreiro Guimarães da Costa⁵⁷, R. Bartoldus¹⁴⁴, A.E. Barton⁷², P. Bartos^{145a}, A. Bassalat¹¹⁷, A. Basye¹⁶⁶, R.L. Bates⁵³, S.J. Batista¹⁵⁹, J.R. Batley²⁸, M. Battaglia¹³⁸, M. Baucé^{133a,133b}, F. Bauer¹³⁷, H.S. Bawa^{144,e}, J.B. Beacham¹¹¹, M.D. Beattie⁷², T. Beau⁸⁰, P.H. Beauchemin¹⁶², R. Beccherle^{124a,124b}, P. Bechtel²¹, H.P. Beck^{17,f}, K. Becker¹²⁰, S. Becker¹⁰⁰, M. Beckingham¹⁷¹, C. Becot¹¹⁷, A.J. Beddall^{19c}, A. Beddall^{19c}, V.A. Bednyakov⁶⁵, C.P. Bee¹⁴⁹, L.J. Beamster¹⁰⁷, T.A. Beermann¹⁷⁶, M. Begel²⁵, J.K. Behr¹²⁰, C. Belanger-Champagne⁸⁷, P.J. Bell⁴⁹, W.H. Bell⁴⁹, G. Bella¹⁵⁴, L. Bellagamba^{20a}, A. Bellerive²⁹, M. Bellomo⁸⁶, K. Belotskiy⁹⁸, O. Beltramello³⁰, O. Benary¹⁵⁴, D. Bencheikroun^{136a}, M. Bender¹⁰⁰, K. Bendtz^{147a,147b}, N. Benekos¹⁰, Y. Benhammou¹⁵⁴, E. Benhar Nocchioli⁴⁹, J.A. Benitez Garcia^{160b}, D.P. Benjamin⁴⁵, J.R. Bensinger²³, S. Bentvelsen¹⁰⁷, L. Beresford¹²⁰, M. Beretta⁴⁷,

D. Berge¹⁰⁷, E. Bergeaas Kuutmann¹⁶⁷, N. Berger⁵, F. Berghaus¹⁷⁰, J. Beringer¹⁵,
 C. Bernard²², N.R. Bernard⁸⁶, C. Bernius¹¹⁰, F.U. Bernlochner²¹, T. Berry⁷⁷,
 P. Berta¹²⁹, C. Bertella⁸³, G. Bertoli^{147a,147b}, F. Bertolucci^{124a,124b}, C. Bertsche¹¹³,
 D. Bertsche¹¹³, M.I. Besana^{91a}, G.J. Besjes¹⁰⁶, O. Bessidskaia Bylund^{147a,147b},
 M. Bessner⁴², N. Besson¹³⁷, C. Betancourt⁴⁸, S. Bethke¹⁰¹, A.J. Bevan⁷⁶, W. Bhimji⁴⁶,
 R.M. Bianchi¹²⁵, L. Bianchini²³, M. Bianco³⁰, O. Biebel¹⁰⁰, S.P. Bieniek⁷⁸,
 M. Biglietti^{135a}, J. Bilbao De Mendizabal⁴⁹, H. Bilokon⁴⁷, M. Bindi⁵⁴, S. Binet¹¹⁷,
 A. Bingul^{19c}, C. Bini^{133a,133b}, C.W. Black¹⁵¹, J.E. Black¹⁴⁴, K.M. Black²²,
 D. Blackburn¹³⁹, R.E. Blair⁶, J.-B. Blanchard¹³⁷, J.E. Blanco⁷⁷, T. Blazek^{145a}, I. Bloch⁴²,
 C. Blocker²³, W. Blum^{83,*}, U. Blumenschein⁵⁴, G.J. Bobbink¹⁰⁷, V.S. Bobrovnikov^{109,c},
 S.S. Bocchetta⁸¹, A. Bocci⁴⁵, C. Bock¹⁰⁰, C.R. Boddy¹²⁰, M. Boehler⁴⁸, J.A. Bogaerts³⁰,
 A.G. Bogdanchikov¹⁰⁹, C. Boehm^{147a}, V. Boisvert⁷⁷, T. Bold^{38a}, V. Boldea^{26a},
 A.S. Boldyrev⁹⁹, M. Bomben⁸⁰, M. Bona⁷⁶, M. Boonekamp¹³⁷, A. Borisov¹³⁰,
 G. Borissov⁷², S. Borroni⁴², J. Bortfeldt¹⁰⁰, V. Bortolotto^{60a}, K. Bos¹⁰⁷, D. Boscherini^{20a},
 M. Bosman¹², J. Boudreau¹²⁵, J. Bouffard², E.V. Bouhova-Thacker⁷², D. Boumediene³⁴,
 C. Bourdarios¹¹⁷, N. Bousson¹¹⁴, S. Boutouil^{136d}, A. Boveia³⁰, J. Boyd³⁰, I.R. Boyko⁶⁵,
 I. Bozic¹³, J. Bracinik¹⁸, A. Brandt⁸, G. Brandt¹⁵, O. Brandt^{58a}, U. Bratzler¹⁵⁷,
 B. Brau⁸⁶, J.E. Brau¹¹⁶, H.M. Braun^{176,*}, S.F. Brazzale^{165a,165c}, K. Brendlinger¹²²,
 A.J. Brennan⁸⁸, L. Brenner¹⁰⁷, R. Brenner¹⁶⁷, S. Bressler¹⁷³, K. Bristow^{146c},
 T.M. Bristow⁴⁶, D. Britton⁵³, D. Britzger⁴², F.M. Brochu²⁸, I. Brock²¹, R. Brock⁹⁰,
 J. Bronner¹⁰¹, G. Brooijmans³⁵, T. Brooks⁷⁷, W.K. Brooks^{32b}, J. Brosamer¹⁵,
 E. Brost¹¹⁶, J. Brown⁵⁵, P.A. Bruckman de Renstrom³⁹, D. Bruncko^{145b}, R. Bruneliere⁴⁸,
 A. Bruni^{20a}, G. Bruni^{20a}, M. Bruschi^{20a}, L. Bryngemark⁸¹, T. Buanes¹⁴, Q. Buat¹⁴³,
 F. Bucci⁴⁹, P. Buchholz¹⁴², A.G. Buckley⁵³, S.I. Buda^{26a}, I.A. Budagov⁶⁵, F. Buehrer⁴⁸,
 L. Bugge¹¹⁹, M.K. Bugge¹¹⁹, O. Bulekov⁹⁸, H. Burckhart³⁰, S. Burdin⁷⁴,
 B. Burghgrave¹⁰⁸, S. Burke¹³¹, I. Burmeister⁴³, E. Busato³⁴, D. Büscher⁴⁸, V. Büscher⁸³,
 P. Bussey⁵³, C.P. Buszello¹⁶⁷, J.M. Butler²², A.I. Butt³, C.M. Buttar⁵³,
 J.M. Butterworth⁷⁸, P. Butti¹⁰⁷, W. Buttinger²⁵, A. Buzatu⁵³, S. Cabrera Urbán¹⁶⁸,
 D. Caforio¹²⁸, O. Cakir^{4a}, P. Calafiura¹⁵, A. Calandri¹³⁷, G. Calderini⁸⁰, P. Calfayan¹⁰⁰,
 L.P. Caloba^{24a}, D. Calvet³⁴, S. Calvet³⁴, R. Camacho Toro⁴⁹, S. Camarda⁴²,
 D. Cameron¹¹⁹, L.M. Caminada¹⁵, R. Caminal Armadans¹², S. Campana³⁰,
 M. Campanelli⁷⁸, A. Campoverde¹⁴⁹, V. Canale^{104a,104b}, A. Canepa^{160a}, M. Cano Bret⁷⁶,
 J. Cantero⁸², R. Cantrill^{126a}, T. Cao⁴⁰, M.D.M. Capeans Garrido³⁰, I. Caprini^{26a},
 M. Caprini^{26a}, M. Capua^{37a,37b}, R. Caputo⁸³, R. Cardarelli^{134a}, T. Carli³⁰, G. Carlino^{104a},
 L. Carminati^{91a,91b}, S. Caron¹⁰⁶, E. Carquin^{32a}, G.D. Carrillo-Montoya^{146c}, J.R. Carter²⁸,
 J. Carvalho^{126a,126c}, D. Casadei⁷⁸, M.P. Casado¹², M. Casolino¹²,
 E. Castaneda-Miranda^{146b}, A. Castelli¹⁰⁷, V. Castillo Gimenez¹⁶⁸, N.F. Castro^{126a,g},
 P. Catastini⁵⁷, A. Catinaccio³⁰, J.R. Catmore¹¹⁹, A. Cattai³⁰, G. Cattani^{134a,134b},
 J. Caudron⁸³, V. Cavaliere¹⁶⁶, D. Cavalli^{91a}, M. Cavalli-Sforza¹², V. Cavasinni^{124a,124b},
 F. Ceradini^{135a,135b}, B.C. Cerio⁴⁵, K. Cerny¹²⁹, A.S. Cerqueira^{24b}, A. Cerri¹⁵⁰,
 L. Cerrito⁷⁶, F. Cerutti¹⁵, M. Cerv³⁰, A. Cervelli¹⁷, S.A. Cetin^{19b}, A. Chafaq^{136a},
 D. Chakraborty¹⁰⁸, I. Chalupkova¹²⁹, P. Chang¹⁶⁶, B. Chapleau⁸⁷, J.D. Chapman²⁸,
 D. Charfeddine¹¹⁷, D.G. Charlton¹⁸, C.C. Chau¹⁵⁹, C.A. Chavez Barajas¹⁵⁰,

S. Cheatham¹⁵³, A. Chegwidden⁹⁰, S. Chekanov⁶, S.V. Chekulaev^{160a}, G.A. Chelkov^{65,h},
 M.A. Chelstowska⁸⁹, C. Chen⁶⁴, H. Chen²⁵, K. Chen¹⁴⁹, L. Chen^{33d,i}, S. Chen^{33c},
 X. Chen^{33f}, Y. Chen⁶⁷, H.C. Cheng⁸⁹, Y. Cheng³¹, A. Cheplakov⁶⁵, E. Cheremushkina¹³⁰,
 R. Cherkaoui El Moursli^{136e}, V. Chernyatin^{25,*}, E. Cheu⁷, L. Chevalier¹³⁷, V. Chiarella⁴⁷,
 J.T. Childers⁶, A. Chilingarov⁷², G. Chiodini^{73a}, A.S. Chisholm¹⁸, R.T. Chislett⁷⁸,
 A. Chitan^{26a}, M.V. Chizhov⁶⁵, K. Choi⁶¹, S. Chouridou⁹, B.K.B. Chow¹⁰⁰,
 D. Chromek-Burckhart³⁰, M.L. Chu¹⁵², J. Chudoba¹²⁷, J.J. Chwastowski³⁹, L. Chytka¹¹⁵,
 G. Ciapetti^{133a,133b}, A.K. Ciftci^{4a}, D. Cinca⁵³, V. Cindro⁷⁵, A. Ciocio¹⁵, Z.H. Citron¹⁷³,
 M. Ciubancan^{26a}, A. Clark⁴⁹, P.J. Clark⁴⁶, R.N. Clarke¹⁵, W. Cleland¹²⁵,
 C. Clement^{147a,147b}, Y. Coadou⁸⁵, M. Cobal^{165a,165c}, A. Coccaro¹³⁹, J. Cochran⁶⁴,
 L. Coffey²³, J.G. Cogan¹⁴⁴, B. Cole³⁵, S. Cole¹⁰⁸, A.P. Colijn¹⁰⁷, J. Collot⁵⁵,
 T. Colombo^{58c}, G. Compostella¹⁰¹, P. Conde Muiño^{126a,126b}, E. Coniavitis⁴⁸,
 S.H. Connell^{146b}, I.A. Connelly⁷⁷, S.M. Consonni^{91a,91b}, V. Consorti⁴⁸,
 S. Constantinescu^{26a}, C. Conta^{121a,121b}, G. Conti³⁰, F. Conventi^{104a,j}, M. Cooke¹⁵,
 B.D. Cooper⁷⁸, A.M. Cooper-Sarkar¹²⁰, K. Copic¹⁵, T. Cornelissen¹⁷⁶, M. Corradi^{20a},
 F. Corriveau^{87,k}, A. Corso-Radu¹⁶⁴, A. Cortes-Gonzalez¹², G. Cortiana¹⁰¹, G. Costa^{91a},
 M.J. Costa¹⁶⁸, D. Costanzo¹⁴⁰, D. Côté⁸, G. Cottin²⁸, G. Cowan⁷⁷, B.E. Cox⁸⁴,
 K. Cranmer¹¹⁰, G. Cree²⁹, S. Crépe-Renaudin⁵⁵, F. Crescioli⁸⁰, W.A. Cribbs^{147a,147b},
 M. Crispin Ortuzar¹²⁰, M. Cristinziani²¹, V. Croft¹⁰⁶, G. Crosetti^{37a,37b},
 T. Cuhadar Donszelmann¹⁴⁰, J. Cummings¹⁷⁷, M. Curatolo⁴⁷, C. Cuthbert¹⁵¹,
 H. Cziri¹⁴², P. Czodrowski³, S. D'Auria⁵³, M. D'Onofrio⁷⁴,
 M.J. Da Cunha Sargedas De Sousa^{126a,126b}, C. Da Via⁸⁴, W. Dabrowski^{38a}, A. Dafinca¹²⁰,
 T. Dai⁸⁹, O. Dale¹⁴, F. Dallaire⁹⁵, C. Dallapiccola⁸⁶, M. Dam³⁶, J.R. Dandoy³¹,
 A.C. Daniells¹⁸, M. Danninger¹⁶⁹, M. Dano Hoffmann¹³⁷, V. Dao⁴⁸, G. Darbo^{50a},
 S. Darmora⁸, J. Dassoulas³, A. Dattagupta⁶¹, W. Davey²¹, C. David¹⁷⁰, T. Davidek¹²⁹,
 E. Davies^{120,l}, M. Davies¹⁵⁴, O. Davignon⁸⁰, P. Davison⁷⁸, Y. Davygora^{58a}, E. Dawe¹⁴³,
 I. Dawson¹⁴⁰, R.K. Daya-Ishmukhametova⁸⁶, K. De⁸, R. de Asmundis^{104a},
 S. De Castro^{20a,20b}, S. De Cecco⁸⁰, N. De Groot¹⁰⁶, P. de Jong¹⁰⁷, H. De la Torre⁸²,
 F. De Lorenzi⁶⁴, L. De Nooij¹⁰⁷, D. De Pedis^{133a}, A. De Salvo^{133a}, U. De Sanctis¹⁵⁰,
 A. De Santo¹⁵⁰, J.B. De Vivie De Regie¹¹⁷, W.J. Dearnaley⁷², R. Debbe²⁵,
 C. Debenedetti¹³⁸, D.V. Dedovich⁶⁵, I. Deigaard¹⁰⁷, J. Del Peso⁸², T. Del Prete^{124a,124b},
 D. Delgove¹¹⁷, F. Deliot¹³⁷, C.M. Delitzsch⁴⁹, M. Deliyergiyev⁷⁵, A. Dell'Acqua³⁰,
 L. Dell'Asta²², M. Dell'Orso^{124a,124b}, M. Della Pietra^{104a,j}, D. della Volpe⁴⁹,
 M. Delmastro⁵, P.A. Delsart⁵⁵, C. Deluca¹⁰⁷, D.A. DeMarco¹⁵⁹, S. Demers¹⁷⁷,
 M. Demichev⁶⁵, A. Demilly⁸⁰, S.P. Denisov¹³⁰, D. Derendarz³⁹, J.E. Derkaoui^{136d},
 F. Derue⁸⁰, P. Dervan⁷⁴, K. Desch²¹, C. Deterre⁴², P.O. Deviveiros³⁰, A. Dewhurst¹³¹,
 S. Dhaliwal²³, A. Di Ciaccio^{134a,134b}, L. Di Ciaccio⁵, A. Di Domenico^{133a,133b},
 C. Di Donato^{104a,104b}, A. Di Girolamo³⁰, B. Di Girolamo³⁰, A. Di Mattia¹⁵³,
 B. Di Micco^{135a,135b}, R. Di Nardo⁴⁷, A. Di Simone⁴⁸, R. Di Sipio¹⁵⁹, D. Di Valentino²⁹,
 C. Diaconu⁸⁵, M. Diamond¹⁵⁹, F.A. Dias⁴⁶, M.A. Diaz^{32a}, E.B. Diehl⁸⁹, J. Dietrich¹⁶,
 T.A. Dietzsch^{58a}, S. Diglio⁸⁵, A. Dimitrievska¹³, J. Dingfelder²¹, P. Dita^{26a}, S. Dita^{26a},
 F. Dittus³⁰, F. Djama⁸⁵, T. Djobava^{51b}, J.I. Djuvsland^{58a}, M.A.B. do Vale^{24c}, D. Dobos³⁰,
 M. Dobre^{26a}, C. Doglioni⁴⁹, T. Doherty⁵³, T. Dohmae¹⁵⁶, J. Dolejsi¹²⁹, Z. Dolezal¹²⁹,

B.A. Dolgoshein^{98,*}, M. Donadelli^{24d}, S. Donati^{124a,124b}, P. Dondero^{121a,121b}, J. Donini³⁴,
 J. Dopke¹³¹, A. Doria^{104a}, M.T. Dova⁷¹, A.T. Doyle⁵³, M. Dris¹⁰, E. Dubreuil³⁴,
 E. Duchovni¹⁷³, G. Duckeck¹⁰⁰, O.A. Ducu^{26a}, D. Duda¹⁷⁶, A. Dudarev³⁰, L. Duflot¹¹⁷,
 L. Duguid⁷⁷, M. Dührssen³⁰, M. Dunford^{58a}, H. Duran Yildiz^{4a}, M. Düren⁵²,
 A. Durglishvili^{51b}, D. Duschinger⁴⁴, M. Dwuznik^{38a}, M. Dyndal^{38a}, K.M. Ecker¹⁰¹,
 W. Edson², N.C. Edwards⁴⁶, W. Ehrenfeld²¹, T. Eifert³⁰, G. Eigen¹⁴, K. Einsweiler¹⁵,
 T. Ekelof¹⁶⁷, M. El Kacimi^{136c}, M. Ellert¹⁶⁷, S. Elles⁵, F. Ellinghaus⁸³, A.A. Elliot¹⁷⁰,
 N. Ellis³⁰, J. Elmsheuser¹⁰⁰, M. Elsing³⁰, D. Emeliyanov¹³¹, Y. Enari¹⁵⁶, O.C. Endner⁸³,
 M. Endo¹¹⁸, J. Erdmann⁴³, A. Ereditato¹⁷, D. Eriksson^{147a}, G. Ernis¹⁷⁶, J. Ernst²,
 M. Ernst²⁵, S. Errede¹⁶⁶, E. Ertel⁸³, M. Escalier¹¹⁷, H. Esch⁴³, C. Escobar¹²⁵,
 B. Esposito⁴⁷, A.I. Etienvre¹³⁷, E. Etzion¹⁵⁴, H. Evans⁶¹, A. Ezhilov¹²³, L. Fabbri^{20a,20b},
 G. Facini³¹, R.M. Fakhruddinov¹³⁰, S. Falciano^{133a}, R.J. Falla⁷⁸, J. Faltova¹²⁹,
 Y. Fang^{33a}, M. Fanti^{91a,91b}, A. Farbin⁸, A. Farilla^{135a}, T. Farooque¹², S. Farrell¹⁵,
 S.M. Farrington¹⁷¹, P. Farthouat³⁰, F. Fassi^{136e}, P. Fassnacht³⁰, D. Fassouliotis⁹,
 A. Favareto^{50a,50b}, L. Fayard¹¹⁷, P. Federic^{145a}, O.L. Fedin^{123,m}, W. Fedorko¹⁶⁹,
 S. Feigl³⁰, L. Feligioni⁸⁵, C. Feng^{33d}, E.J. Feng⁶, H. Feng⁸⁹, A.B. Fenyuk¹³⁰,
 P. Fernandez Martinez¹⁶⁸, S. Fernandez Perez³⁰, S. Ferrag⁵³, J. Ferrando⁵³, A. Ferrari¹⁶⁷,
 P. Ferrari¹⁰⁷, R. Ferrari^{121a}, D.E. Ferreira de Lima⁵³, A. Ferrer¹⁶⁸, D. Ferrere⁴⁹,
 C. Ferretti⁸⁹, A. Ferretto Parodi^{50a,50b}, M. Fiascaris³¹, F. Fiedler⁸³, A. Filipčič⁷⁵,
 M. Filipuzzi⁴², F. Filthaut¹⁰⁶, M. Fincke-Keeler¹⁷⁰, K.D. Finelli¹⁵¹,
 M.C.N. Fiolhais^{126a,126c}, L. Fiorini¹⁶⁸, A. Firan⁴⁰, A. Fischer², C. Fischer¹², J. Fischer¹⁷⁶,
 W.C. Fisher⁹⁰, E.A. Fitzgerald²³, M. Flechl⁴⁸, I. Fleck¹⁴², P. Fleischmann⁸⁹,
 S. Fleischmann¹⁷⁶, G.T. Fletcher¹⁴⁰, G. Fletcher⁷⁶, T. Flick¹⁷⁶, A. Floderus⁸¹,
 L.R. Flores Castillo^{60a}, M.J. Flowerdew¹⁰¹, A. Formica¹³⁷, A. Forti⁸⁴, D. Fournier¹¹⁷,
 H. Fox⁷², S. Fracchia¹², P. Francavilla⁸⁰, M. Franchini^{20a,20b}, D. Francis³⁰, L. Franconi¹¹⁹,
 M. Franklin⁵⁷, M. Fraternali^{121a,121b}, D. Freeborn⁷⁸, S.T. French²⁸, F. Friedrich⁴⁴,
 D. Froidevaux³⁰, J.A. Frost¹²⁰, C. Fukunaga¹⁵⁷, E. Fullana Torregrosa⁸³, B.G. Fulsom¹⁴⁴,
 J. Fuster¹⁶⁸, C. Gabaldon⁵⁵, O. Gabizon¹⁷⁶, A. Gabrielli^{20a,20b}, A. Gabrielli^{133a,133b},
 S. Gadatsch¹⁰⁷, S. Gadomski⁴⁹, G. Gagliardi^{50a,50b}, P. Gagnon⁶¹, C. Galea¹⁰⁶,
 B. Galhardo^{126a,126c}, E.J. Gallas¹²⁰, B.J. Gallop¹³¹, P. Gallus¹²⁸, G. Galster³⁶,
 K.K. Gan¹¹¹, J. Gao^{33b,85}, Y.S. Gao^{144,e}, F.M. Garay Walls⁴⁶, F. Garbersen¹⁷⁷,
 C. García¹⁶⁸, J.E. García Navarro¹⁶⁸, M. Garcia-Sciveres¹⁵, R.W. Gardner³¹,
 N. Garelli¹⁴⁴, V. Garonne³⁰, C. Gatti⁴⁷, G. Gaudio^{121a}, B. Gaur¹⁴², L. Gauthier⁹⁵,
 P. Gauzzi^{133a,133b}, I.L. Gavrilenko⁹⁶, C. Gay¹⁶⁹, G. Gaycken²¹, E.N. Gazis¹⁰, P. Ge^{33d},
 Z. Gece¹⁶⁹, C.N.P. Gee¹³¹, D.A.A. Geerts¹⁰⁷, Ch. Geich-Gimbel²¹, C. Gemme^{50a},
 M.H. Genest⁵⁵, S. Gentile^{133a,133b}, M. George⁵⁴, S. George⁷⁷, D. Gerbaudo¹⁶⁴,
 A. Gershon¹⁵⁴, H. Ghazlane^{136b}, N. Ghodbane³⁴, B. Giacobbe^{20a}, S. Giagu^{133a,133b},
 V. Giangiobbe¹², P. Giannetti^{124a,124b}, F. Gianotti³⁰, B. Gibbard²⁵, S.M. Gibson⁷⁷,
 M. Gilchriese¹⁵, T.P.S. Gillam²⁸, D. Gillberg³⁰, G. Gilles³⁴, D.M. Gingrich^{3,d},
 N. Giokaris⁹, M.P. Giordani^{165a,165c}, F.M. Giorgi^{20a}, F.M. Giorgi¹⁶, P.F. Giraud¹³⁷,
 D. Giugni^{91a}, C. Giuliani⁴⁸, M. Giulini^{58b}, B.K. Gjelsten¹¹⁹, S. Gkaitatzis¹⁵⁵,
 I. Gkialas¹⁵⁵, E.L. Gkoukousis¹¹⁷, L.K. Gladilin⁹⁹, C. Glasman⁸², J. Glatzer³⁰,
 P.C.F. Glaysher⁴⁶, A. Glazov⁴², M. Goblirsch-Kolb¹⁰¹, J.R. Goddard⁷⁶, J. Godlewski³⁹,

S. Goldfarb⁸⁹, T. Golling⁴⁹, D. Golubkov¹³⁰, A. Gomes^{126a,126b,126d}, R. Gonçalo^{126a},
 J. Goncalves Pinto Firmino Da Costa¹³⁷, L. Gonella²¹, S. González de la Hoz¹⁶⁸,
 G. Gonzalez Parra¹², S. Gonzalez-Sevilla⁴⁹, L. Goossens³⁰, P.A. Gorbounov⁹⁷,
 H.A. Gordon²⁵, I. Gorelov¹⁰⁵, B. Gorini³⁰, E. Gorini^{73a,73b}, A. Gorišek⁷⁵, E. Gornicki³⁹,
 A.T. Goshaw⁴⁵, C. Gössling⁴³, M.I. Gostkin⁶⁵, M. Gouighri^{136a}, D. Goujdami^{136c},
 A.G. Goussiou¹³⁹, H.M.X. Grabas¹³⁸, L. Graber⁵⁴, I. Grabowska-Bold^{38a},
 P. Grafström^{20a,20b}, K.-J. Grahn⁴², J. Gramling⁴⁹, E. Gramstad¹¹⁹, S. Grancagnolo¹⁶,
 V. Grassi¹⁴⁹, V. Gratchev¹²³, H.M. Gray³⁰, E. Graziani^{135a}, Z.D. Greenwood^{79,n},
 K. Gregersen⁷⁸, I.M. Gregor⁴², P. Grenier¹⁴⁴, J. Griffiths⁸, A.A. Grillo¹³⁸, K. Grimm⁷²,
 S. Grinstein^{12,o}, Ph. Gris³⁴, J.-F. Grivaz¹¹⁷, J.P. Grohs⁴⁴, A. Grohsjean⁴², E. Gross¹⁷³,
 J. Grosse-Knetter⁵⁴, G.C. Grossi^{134a,134b}, Z.J. Grout¹⁵⁰, L. Guan^{33b}, J. Guenther¹²⁸,
 F. Guescini⁴⁹, D. Guest¹⁷⁷, O. Gueta¹⁵⁴, E. Guido^{50a,50b}, T. Guillemin¹¹⁷, S. Guindon²,
 U. Gul⁵³, C. Gumpert⁴⁴, J. Guo^{33e}, S. Gupta¹²⁰, P. Gutierrez¹¹³, N.G. Gutierrez Ortiz⁵³,
 C. Gutschow⁴⁴, N. Guttman¹⁵⁴, C. Guyot¹³⁷, C. Gwenlan¹²⁰, C.B. Gwilliam⁷⁴,
 A. Haas¹¹⁰, C. Haber¹⁵, H.K. Hadavand⁸, N. Haddad^{136e}, P. Haefner²¹, S. Hageböck²¹,
 Z. Hajduk³⁹, H. Hakobyan¹⁷⁸, M. Haleem⁴², J. Haley¹¹⁴, D. Hall¹²⁰, G. Halladjian⁹⁰,
 G.D. Hallewell⁸⁵, K. Hamacher¹⁷⁶, P. Hamal¹¹⁵, K. Hamano¹⁷⁰, M. Hamer⁵⁴,
 A. Hamilton^{146a}, S. Hamilton¹⁶², G.N. Hamity^{146c}, P.G. Hamnett⁴², L. Han^{33b},
 K. Hanagaki¹¹⁸, K. Hanawa¹⁵⁶, M. Hance¹⁵, P. Hanke^{58a}, R. Hanna¹³⁷, J.B. Hansen³⁶,
 J.D. Hansen³⁶, P.H. Hansen³⁶, K. Hara¹⁶¹, A.S. Hard¹⁷⁴, T. Harenberg¹⁷⁶, F. Hariri¹¹⁷,
 S. Harkusha⁹², R.D. Harrington⁴⁶, P.F. Harrison¹⁷¹, F. Hartjes¹⁰⁷, M. Hasegawa⁶⁷,
 S. Hasegawa¹⁰³, Y. Hasegawa¹⁴¹, A. Hasib¹¹³, S. Hassani¹³⁷, S. Haug¹⁷, R. Hauser⁹⁰,
 L. Hauswald⁴⁴, M. Havranek¹²⁷, C.M. Hawkes¹⁸, R.J. Hawkings³⁰, A.D. Hawkins⁸¹,
 T. Hayashi¹⁶¹, D. Hayden⁹⁰, C.P. Hays¹²⁰, J.M. Hays⁷⁶, H.S. Hayward⁷⁴,
 S.J. Haywood¹³¹, S.J. Head¹⁸, T. Heck⁸³, V. Hedberg⁸¹, L. Heelan⁸, S. Heim¹²²,
 T. Heim¹⁷⁶, B. Heinemann¹⁵, L. Heinrich¹¹⁰, J. Hejbal¹²⁷, L. Helary²², M. Heller³⁰,
 S. Hellman^{147a,147b}, D. Hellmich²¹, C. Hensens³⁰, J. Henderson¹²⁰, R.C.W. Henderson⁷²,
 Y. Heng¹⁷⁴, C. Hengler⁴², A. Henrichs¹⁷⁷, A.M. Henriques Correia³⁰,
 S. Henrot-Versille¹¹⁷, G.H. Herbert¹⁶, Y. Hernández Jiménez¹⁶⁸, R. Herrberg-Schubert¹⁶,
 G. Herten⁴⁸, R. Hertenberger¹⁰⁰, L. Hervas³⁰, G.G. Hesketh⁷⁸, N.P. Hesse¹⁰⁷,
 R. Hickling⁷⁶, E. Higón-Rodríguez¹⁶⁸, E. Hill¹⁷⁰, J.C. Hill²⁸, K.H. Hiller⁴², S.J. Hillier¹⁸,
 I. Hinchliffe¹⁵, E. Hines¹²², R.R. Hinman¹⁵, M. Hirose¹⁵⁸, D. Hirschbuehl¹⁷⁶, J. Hobbs¹⁴⁹,
 N. Hod¹⁰⁷, M.C. Hodgkinson¹⁴⁰, P. Hodgson¹⁴⁰, A. Hoecker³⁰, M.R. Hoferkamp¹⁰⁵,
 F. Hoenig¹⁰⁰, M. Hohlfeld⁸³, T.R. Holmes¹⁵, T.M. Hong¹²², L. Hooft van Huysduynen¹¹⁰,
 W.H. Hopkins¹¹⁶, Y. Horii¹⁰³, A.J. Horton¹⁴³, J.-Y. Hostachy⁵⁵, S. Hou¹⁵²,
 A. Hoummada^{136a}, J. Howard¹²⁰, J. Howarth⁴², M. Hrabovsky¹¹⁵, I. Hristova¹⁶,
 J. Hrivnac¹¹⁷, T. Hryn'ova⁵, A. Hrynevich⁹³, C. Hsu^{146c}, P.J. Hsu^{152,p}, S.-C. Hsu¹³⁹,
 D. Hu³⁵, Q. Hu^{33b}, X. Hu⁸⁹, Y. Huang⁴², Z. Hubacek³⁰, F. Hubaut⁸⁵, F. Huegging²¹,
 T.B. Huffman¹²⁰, E.W. Hughes³⁵, G. Hughes⁷², M. Huhtinen³⁰, T.A. Hülsing⁸³,
 N. Huseynov^{65,b}, J. Huston⁹⁰, J. Huth⁵⁷, G. Iacobucci⁴⁹, G. Iakovidis²⁵, I. Ibragimov¹⁴²,
 L. Iconomidou-Fayard¹¹⁷, E. Ideal¹⁷⁷, Z. Idrissi^{136e}, P. Iengo^{104a}, O. Igonkina¹⁰⁷,
 T. Iizawa¹⁷², Y. Ikegami⁶⁶, K. Ikematsu¹⁴², M. Ikeno⁶⁶, Y. Ilchenko^{31,q}, D. Iliadis¹⁵⁵,
 N. Ilic¹⁵⁹, Y. Inamaru⁶⁷, T. Ince¹⁰¹, P. Ioannou⁹, M. Iodice^{135a}, K. Iordanidou⁹,

V. Ippolito⁵⁷, A. Irlles Quiles¹⁶⁸, C. Isaksson¹⁶⁷, M. Ishino⁶⁸, M. Ishitsuka¹⁵⁸,
 R. Ishmukhametov¹¹¹, C. Issever¹²⁰, S. Istin^{19a}, J.M. Iturbe Ponce⁸⁴, R. Iuppa^{134a,134b},
 J. Ivarsson⁸¹, W. Iwanski³⁹, H. Iwasaki⁶⁶, J.M. Izen⁴¹, V. Izzo^{104a}, S. Jabbar³,
 B. Jackson¹²², M. Jackson⁷⁴, P. Jackson¹, M.R. Jaekel³⁰, V. Jain², K. Jakobs⁴⁸,
 S. Jakobsen³⁰, T. Jakoubek¹²⁷, J. Jakubek¹²⁸, D.O. Jamin¹⁵², D.K. Jana⁷⁹, E. Jansen⁷⁸,
 R.W. Jansky⁶², J. Janssen²¹, M. Janus¹⁷¹, G. Jarlskog⁸¹, N. Javadov^{65,b}, T. Javůrek⁴⁸,
 L. Jeanty¹⁵, J. Jejelava^{51a,r}, G.-Y. Jeng¹⁵¹, D. Jennens⁸⁸, P. Jenni^{48,s}, J. Jentzsch⁴³,
 C. Jeske¹⁷¹, S. Jézéquel⁵, H. Ji¹⁷⁴, J. Jia¹⁴⁹, Y. Jiang^{33b}, J. Jimenez Pena¹⁶⁸, S. Jin^{33a},
 A. Jinaru^{26a}, O. Jinnouchi¹⁵⁸, M.D. Joergensen³⁶, P. Johansson¹⁴⁰, K.A. Johns⁷,
 K. Jon-And^{147a,147b}, G. Jones¹⁷¹, R.W.L. Jones⁷², T.J. Jones⁷⁴, J. Jongmanns^{58a},
 P.M. Jorge^{126a,126b}, K.D. Joshi⁸⁴, J. Jovicevic¹⁴⁸, X. Ju¹⁷⁴, C.A. Jung⁴³, P. Jussel⁶²,
 A. Juste Rozas^{12,o}, M. Kaci¹⁶⁸, A. Kaczmarek³⁹, M. Kado¹¹⁷, H. Kagan¹¹¹,
 M. Kagan¹⁴⁴, S.J. Kahn⁸⁵, E. Kajomovitz⁴⁵, C.W. Kalderon¹²⁰, S. Kama⁴⁰,
 A. Kamenshchikov¹³⁰, N. Kanaya¹⁵⁶, M. Kaneda³⁰, S. Kaneti²⁸, V.A. Kantserov⁹⁸,
 J. Kanzaki⁶⁶, B. Kaplan¹¹⁰, A. Kapliy³¹, D. Kar⁵³, K. Karakostas¹⁰, A. Karamaoun³,
 N. Karastathis^{10,107}, M.J. Kareem⁵⁴, M. Karnevskiy⁸³, S.N. Karpov⁶⁵, Z.M. Karpova⁶⁵,
 K. Karthik¹¹⁰, V. Kartvelishvili⁷², A.N. Karyukhin¹³⁰, L. Kashif¹⁷⁴, R.D. Kass¹¹¹,
 A. Kastanas¹⁴, Y. Kataoka¹⁵⁶, A. Katre⁴⁹, J. Katzy⁴², K. Kawagoe⁷⁰, T. Kawamoto¹⁵⁶,
 G. Kawamura⁵⁴, S. Kazama¹⁵⁶, V.F. Kazanin^{109,c}, M.Y. Kazarinov⁶⁵, R. Keeler¹⁷⁰,
 R. Kehoe⁴⁰, J.S. Keller⁴², J.J. Kempster⁷⁷, H. Keoshkerian⁸⁴, O. Kepka¹²⁷,
 B.P. Kerševan⁷⁵, S. Kersten¹⁷⁶, R.A. Keyes⁸⁷, F. Khalil-zada¹¹, H. Khandanyan^{147a,147b},
 A. Khanov¹¹⁴, A.G. Kharlamov^{109,c}, A. Khodinov⁹⁸, A. Khomich^{58a}, T.J. Khoo²⁸,
 V. Khovanskiy⁹⁷, E. Khramov⁶⁵, J. Khubua^{51b,t}, H.Y. Kim⁸, H. Kim^{147a,147b},
 S.H. Kim¹⁶¹, Y. Kim³¹, N. Kimura¹⁵⁵, O.M. Kind¹⁶, B.T. King⁷⁴, M. King¹⁶⁸,
 R.S.B. King¹²⁰, S.B. King¹⁶⁹, J. Kirk¹³¹, A.E. Kiryunin¹⁰¹, T. Kishimoto⁶⁷,
 D. Kisielewska^{38a}, F. Kiss⁴⁸, K. Kiuchi¹⁶¹, E. Kladiva^{145b}, M.H. Klein³⁵, M. Klein⁷⁴,
 U. Klein⁷⁴, K. Kleinknecht⁸³, P. Klimek^{147a,147b}, A. Klimentov²⁵, R. Klingenberg⁴³,
 J.A. Klinger⁸⁴, T. Klioutchnikova³⁰, P.F. Klok¹⁰⁶, E.-E. Kluge^{58a}, P. Kluit¹⁰⁷,
 S. Kluth¹⁰¹, E. Kneringer⁶², E.B.F.G. Knoops⁸⁵, A. Knue⁵³, D. Kobayashi¹⁵⁸,
 T. Kobayashi¹⁵⁶, M. Kobel⁴⁴, M. Kocian¹⁴⁴, P. Kodys¹²⁹, T. Koffas²⁹, E. Koffeman¹⁰⁷,
 L.A. Kogan¹²⁰, S. Kohlmann¹⁷⁶, Z. Kohout¹²⁸, T. Kohriki⁶⁶, T. Koi¹⁴⁴, H. Kolanoski¹⁶,
 I. Koletsou⁵, A.A. Komar^{96,*}, Y. Komori¹⁵⁶, T. Kondo⁶⁶, N. Kondrashova⁴²,
 K. Köneke⁴⁸, A.C. König¹⁰⁶, S. König⁸³, T. Kono^{66,u}, R. Konoplich^{110,v},
 N. Konstantinidis⁷⁸, R. Kopeliansky¹⁵³, S. Koperny^{38a}, L. Köpke⁸³, A.K. Kopp⁴⁸,
 K. Korcyl³⁹, K. Kordas¹⁵⁵, A. Korn⁷⁸, A.A. Korol^{109,c}, I. Korolkov¹², E.V. Korolkova¹⁴⁰,
 O. Kortner¹⁰¹, S. Kortner¹⁰¹, T. Kosek¹²⁹, V.V. Kostyukhin²¹, V.M. Kotov⁶⁵,
 A. Kotwal⁴⁵, A. Kourkouveli-Charalampidi¹⁵⁵, C. Kourkouvelis⁹, V. Kouskoura²⁵,
 A. Koutsman^{160a}, R. Kowalewski¹⁷⁰, T.Z. Kowalski^{38a}, W. Kozanecki¹³⁷, A.S. Kozhin¹³⁰,
 V.A. Kramarenko⁹⁹, G. Kramberger⁷⁵, D. Krasnopevtsev⁹⁸, M.W. Krasny⁸⁰,
 A. Krasznahorkay³⁰, J.K. Kraus²¹, A. Kravchenko²⁵, S. Kreiss¹¹⁰, M. Kretz^{58c},
 J. Kretzschmar⁷⁴, K. Kreutzfeldt⁵², P. Krieger¹⁵⁹, K. Krizka³¹, K. Kroeninger⁴³,
 H. Kroha¹⁰¹, J. Kroll¹²², J. Kroseberg²¹, J. Krstic¹³, U. Kruchonak⁶⁵, H. Krüger²¹,
 N. Krumnack⁶⁴, Z.V. Krumshteyn⁶⁵, A. Kruse¹⁷⁴, M.C. Kruse⁴⁵, M. Kruskal²²,

T. Kubota⁸⁸, H. Kucuk⁷⁸, S. Kunday^{4c}, S. Kuehn⁴⁸, A. Kugel^{58c}, F. Kuger¹⁷⁵, A. Kuhl¹³⁸,
 T. Kuhl⁴², V. Kukhtin⁶⁵, Y. Kulchitsky⁹², S. Kuleshov^{32b}, M. Kuna^{133a,133b}, T. Kunigo⁶⁸,
 A. Kupco¹²⁷, H. Kurashige⁶⁷, Y.A. Kurochkin⁹², R. Kurumida⁶⁷, V. Kus¹²⁷,
 E.S. Kuwertz¹⁴⁸, M. Kuze¹⁵⁸, J. Kvita¹¹⁵, T. Kwan¹⁷⁰, D. Kyriazopoulos¹⁴⁰,
 A. La Rosa⁴⁹, J.L. La Rosa Navarro^{24d}, L. La Rotonda^{37a,37b}, C. Lacasta¹⁶⁸,
 F. Lacava^{133a,133b}, J. Lacey²⁹, H. Lacker¹⁶, D. Lacour⁸⁰, V.R. Lacuesta¹⁶⁸, E. Ladygin⁶⁵,
 R. Lafaye⁵, B. Laforge⁸⁰, T. Lagouri¹⁷⁷, S. Lai⁴⁸, L. Lambourne⁷⁸, S. Lammers⁶¹,
 C.L. Lampen⁷, W. Lampl⁷, E. Lançon¹³⁷, U. Landgraf⁴⁸, M.P.J. Landon⁷⁶, V.S. Lang^{58a},
 A.J. Lankford¹⁶⁴, F. Lanni²⁵, K. Lantzschi³⁰, S. Laplace⁸⁰, C. Lapoire³⁰, J.F. Laporte¹³⁷,
 T. Lari^{91a}, F. Lasagni Manghi^{20a,20b}, M. Lassnig³⁰, P. Laurelli⁴⁷, W. Lavrijsen¹⁵,
 A.T. Law¹³⁸, P. Laycock⁷⁴, O. Le Dortz⁸⁰, E. Le Guirriec⁸⁵, E. Le Menedeu¹²,
 T. LeCompte⁶, F. Ledroit-Guillon⁵⁵, C.A. Lee^{146b}, S.C. Lee¹⁵², L. Lee¹, G. Lefebvre⁸⁰,
 M. Lefebvre¹⁷⁰, F. Legger¹⁰⁰, C. Leggett¹⁵, A. Lehan⁷⁴, G. Lehmann Miotto³⁰, X. Lei⁷,
 W.A. Leight²⁹, A. Leisos¹⁵⁵, A.G. Leister¹⁷⁷, M.A.L. Leite^{24d}, R. Leitner¹²⁹,
 D. Lellouch¹⁷³, B. Lemmer⁵⁴, K.J.C. Leney⁷⁸, T. Lenz²¹, B. Lenzi³⁰, R. Leone⁷,
 S. Leone^{124a,124b}, C. Leonidopoulos⁴⁶, S. Leontsinis¹⁰, C. Leroy⁹⁵, C.G. Lester²⁸,
 M. Levchenko¹²³, J. Levêque⁵, D. Levin⁸⁹, L.J. Levinson¹⁷³, M. Levy¹⁸, A. Lewis¹²⁰,
 A.M. Leyko²¹, M. Leyton⁴¹, B. Li^{33b,w}, B. Li⁸⁵, H. Li¹⁴⁹, H.L. Li³¹, L. Li⁴⁵, L. Li^{33e},
 S. Li⁴⁵, Y. Li^{33c,x}, Z. Liang¹³⁸, H. Liao³⁴, B. Liberti^{134a}, P. Lichard³⁰, K. Lie¹⁶⁶,
 J. Liebal²¹, W. Liebig¹⁴, C. Limbach²¹, A. Limosani¹⁵¹, S.C. Lin^{152,y}, T.H. Lin⁸³,
 F. Linde¹⁰⁷, B.E. Lindquist¹⁴⁹, J.T. Linnemann⁹⁰, E. Lipeles¹²², A. Lipniacka¹⁴,
 M. Lisovyi⁴², T.M. Liss¹⁶⁶, D. Lissauer²⁵, A. Lister¹⁶⁹, A.M. Litke¹³⁸, B. Liu^{152,z},
 D. Liu¹⁵², J. Liu⁸⁵, J.B. Liu^{33b}, K. Liu⁸⁵, L. Liu⁸⁹, M. Liu⁴⁵, M. Liu^{33b}, Y. Liu^{33b},
 M. Livan^{121a,121b}, A. Lleres⁵⁵, J. Llorente Merino⁸², S.L. Lloyd⁷⁶, F. Lo Sterzo¹⁵²,
 E. Lobodzinska⁴², P. Loch⁷, W.S. Lockman¹³⁸, F.K. Loebinger⁸⁴,
 A.E. Loevschall-Jensen³⁶, A. Loginov¹⁷⁷, T. Lohse¹⁶, K. Lohwasser⁴², M. Lokajicek¹²⁷,
 B.A. Long²², J.D. Long⁸⁹, R.E. Long⁷², K.A. Looper¹¹¹, L. Lopes^{126a}, D. Lopez Mateos⁵⁷,
 B. Lopez Paredes¹⁴⁰, I. Lopez Paz¹², J. Lorenz¹⁰⁰, N. Lorenzo Martinez⁶¹, M. Losada¹⁶³,
 P. Loscutoff¹⁵, P.J. Lösel¹⁰⁰, X. Lou^{33a}, A. Lounis¹¹⁷, J. Love⁶, P.A. Love⁷², N. Lu⁸⁹,
 H.J. Lubatti¹³⁹, C. Luci^{133a,133b}, A. Lucotte⁵⁵, F. Luehring⁶¹, W. Lukas⁶²,
 L. Luminari^{133a}, O. Lundberg^{147a,147b}, B. Lund-Jensen¹⁴⁸, M. Lungwitz⁸³, D. Lynn²⁵,
 R. Lysak¹²⁷, E. Lytken⁸¹, H. Ma²⁵, L.L. Ma^{33d}, G. Maccarrone⁴⁷, A. Macchiolo¹⁰¹,
 C.M. Macdonald¹⁴⁰, J. Machado Miguens^{126a,126b}, D. Macina³⁰, D. Madaffari⁸⁵,
 R. Madar³⁴, H.J. Maddocks⁷², W.F. Mader⁴⁴, A. Madsen¹⁶⁷, T. Maeno²⁵, A. Maevskiy⁹⁹,
 E. Magradze⁵⁴, K. Mahboubi⁴⁸, J. Mahlstedt¹⁰⁷, S. Mahmoud⁷⁴, C. Maiani¹³⁷,
 C. Maidantchik^{24a}, A.A. Maier¹⁰¹, T. Maier¹⁰⁰, A. Maio^{126a,126b,126d}, S. Majewski¹¹⁶,
 Y. Makida⁶⁶, N. Makovec¹¹⁷, B. Malaescu⁸⁰, Pa. Malecki³⁹, V.P. Maleev¹²³, F. Malek⁵⁵,
 U. Mallik⁶³, D. Malon⁶, C. Malone¹⁴⁴, S. Maltezos¹⁰, V.M. Malyshev¹⁰⁹, S. Malyukov³⁰,
 J. Mamuzic⁴², G. Mancini⁴⁷, B. Mandelli³⁰, L. Mandelli^{91a}, I. Mandić⁷⁵, R. Mandrysch⁶³,
 J. Maneira^{126a,126b}, A. Manfredini¹⁰¹, L. Manhaes de Andrade Filho^{24b},
 J. Manjarres Ramos^{160b}, A. Mann¹⁰⁰, P.M. Manning¹³⁸, A. Manousakis-Katsikakis⁹,
 B. Mansoulie¹³⁷, R. Mantifel⁸⁷, M. Mantoani⁵⁴, L. Mapelli³⁰, L. March^{146c},
 G. Marchiori⁸⁰, M. Marcisovsky¹²⁷, C.P. Marino¹⁷⁰, M. Marjanovic¹³, F. Marroquim^{24a},

S.P. Marsden⁸⁴, Z. Marshall¹⁵, L.F. Marti¹⁷, S. Marti-Garcia¹⁶⁸, B. Martin⁹⁰,
 T.A. Martin¹⁷¹, V.J. Martin⁴⁶, B. Martin dit Latour¹⁴, H. Martinez¹³⁷, M. Martinez^{12,o},
 S. Martin-Haugh¹³¹, V.S. Martoiu^{26a}, A.C. Martyniuk⁷⁸, M. Marx¹³⁹, F. Marzano^{133a},
 A. Marzin³⁰, L. Masetti⁸³, T. Mashimo¹⁵⁶, R. Mashinistov⁹⁶, J. Masik⁸⁴,
 A.L. Maslennikov^{109,c}, I. Massa^{20a,20b}, L. Massa^{20a,20b}, N. Massol⁵, P. Mastrandrea¹⁴⁹,
 A. Mastroberardino^{37a,37b}, T. Masubuchi¹⁵⁶, P. Mättig¹⁷⁶, J. Mattmann⁸³, J. Maurer^{26a},
 S.J. Maxfield⁷⁴, D.A. Maximov^{109,c}, R. Mazini¹⁵², S.M. Mazza^{91a,91b},
 L. Mazzaferro^{134a,134b}, G. Mc Goldrick¹⁵⁹, S.P. Mc Kee⁸⁹, A. McCarn⁸⁹,
 R.L. McCarthy¹⁴⁹, T.G. McCarthy²⁹, N.A. McCubbin¹³¹, K.W. McFarlane^{56,*},
 J.A. Mcfayden⁷⁸, G. Mchedlidze⁵⁴, S.J. McMahon¹³¹, R.A. McPherson^{170,k},
 J. Mechnich¹⁰⁷, M. Medinnis⁴², S. Meehan^{146a}, S. Mehlhase¹⁰⁰, A. Mehta⁷⁴, K. Meier^{58a},
 C. Meineck¹⁰⁰, B. Meirose⁴¹, C. Melachrinou³¹, B.R. Mellado Garcia^{146c}, F. Meloni¹⁷,
 A. Mengarelli^{20a,20b}, S. Menke¹⁰¹, E. Meoni¹⁶², K.M. Mercurio⁵⁷, S. Mergelmeyer²¹,
 N. Meric¹³⁷, P. Mermod⁴⁹, L. Merola^{104a,104b}, C. Meroni^{91a}, F.S. Merritt³¹, H. Merritt¹¹¹,
 A. Messina^{30,aa}, J. Metcalfe²⁵, A.S. Mete¹⁶⁴, C. Meyer⁸³, C. Meyer¹²², J-P. Meyer¹³⁷,
 J. Meyer¹⁰⁷, R.P. Middleton¹³¹, S. Migas⁷⁴, S. Miglioranza^{165a,165c}, L. Mijović²¹,
 G. Mikenberg¹⁷³, M. Mikestikova¹²⁷, M. Mikuž⁷⁵, A. Milic³⁰, D.W. Miller³¹, C. Mills⁴⁶,
 A. Milov¹⁷³, D.A. Milstead^{147a,147b}, A.A. Minaenko¹³⁰, Y. Minami¹⁵⁶, I.A. Minashvili⁶⁵,
 A.I. Mincer¹¹⁰, B. Mindur^{38a}, M. Mineev⁶⁵, Y. Ming¹⁷⁴, L.M. Mir¹², G. Mirabelli^{133a},
 T. Mitani¹⁷², J. Mitrevski¹⁰⁰, V.A. Mitsou¹⁶⁸, A. Miucci⁴⁹, P.S. Miyagawa¹⁴⁰,
 J.U. Mjörnmärk⁸¹, T. Moa^{147a,147b}, K. Mochizuki⁸⁵, S. Mohapatra³⁵, W. Mohr⁴⁸,
 S. Molander^{147a,147b}, R. Moles-Valls¹⁶⁸, K. Mönig⁴², C. Monini⁵⁵, J. Monk³⁶,
 E. Monnier⁸⁵, J. Montejo Berlingen¹², F. Monticelli⁷¹, S. Monzani^{133a,133b}, R.W. Moore³,
 N. Morange¹¹⁷, D. Moreno¹⁶³, M. Moreno Llácer⁵⁴, P. Morettini^{50a}, M. Morgenstern⁴⁴,
 M. Morii⁵⁷, V. Morisbak¹¹⁹, S. Moritz⁸³, A.K. Morley¹⁴⁸, G. Mornacchi³⁰, J.D. Morris⁷⁶,
 A. Morton⁵³, L. Morvaj¹⁰³, M. Mosidze^{51b}, J. Moss¹¹¹, K. Motohashi¹⁵⁸, R. Mount¹⁴⁴,
 E. Mountricha²⁵, S.V. Mouraviev^{96,*}, E.J.W. Moyse⁸⁶, S. Muanza⁸⁵, R.D. Mudd¹⁸,
 F. Mueller¹⁰¹, J. Mueller¹²⁵, K. Mueller²¹, R.S.P. Mueller¹⁰⁰, T. Mueller²⁸,
 D. Muenstermann⁴⁹, P. Mullen⁵³, Y. Munwes¹⁵⁴, J.A. Murillo Quijada¹⁸,
 W.J. Murray^{171,131}, H. Musheghyan⁵⁴, E. Musto¹⁵³, A.G. Myagkov^{130,ab}, M. Myska¹²⁸,
 O. Nackenhorst⁵⁴, J. Nadal⁵⁴, K. Nagai¹²⁰, R. Nagai¹⁵⁸, Y. Nagai⁸⁵, K. Nagano⁶⁶,
 A. Nagarkar¹¹¹, Y. Nagasaka⁵⁹, K. Nagata¹⁶¹, M. Nagel¹⁰¹, E. Nagy⁸⁵, A.M. Nairz³⁰,
 Y. Nakahama³⁰, K. Nakamura⁶⁶, T. Nakamura¹⁵⁶, I. Nakano¹¹², H. Namasivayam⁴¹,
 G. Nanava²¹, R.F. Naranjo Garcia⁴², R. Narayan^{58b}, T. Nattermann²¹, T. Naumann⁴²,
 G. Navarro¹⁶³, R. Nayyar⁷, H.A. Neal⁸⁹, P.Yu. Nechaeva⁹⁶, T.J. Neep⁸⁴, P.D. Nef¹⁴⁴,
 A. Negri^{121a,121b}, M. Negrini^{20a}, S. Nektarijevic¹⁰⁶, C. Nellist¹¹⁷, A. Nelson¹⁶⁴,
 S. Nemecek¹²⁷, P. Nemethy¹¹⁰, A.A. Nepomuceno^{24a}, M. Nessi^{30,ac}, M.S. Neubauer¹⁶⁶,
 M. Neumann¹⁷⁶, R.M. Neves¹¹⁰, P. Nevski²⁵, P.R. Newman¹⁸, D.H. Nguyen⁶,
 R.B. Nickerson¹²⁰, R. Nicolaidou¹³⁷, B. Nicquevert³⁰, J. Nielsen¹³⁸, N. Nikiforou³⁵,
 A. Nikiforov¹⁶, V. Nikolaenko^{130,ab}, I. Nikolic-Audit⁸⁰, K. Nikolopoulos¹⁸, P. Nilsson²⁵,
 Y. Ninomiya¹⁵⁶, A. Nisati^{133a}, R. Nisius¹⁰¹, T. Nobe¹⁵⁸, M. Nomachi¹¹⁸, I. Nomidis²⁹,
 T. Nooney⁷⁶, S. Norberg¹¹³, M. Nordberg³⁰, O. Novgorodova⁴⁴, S. Nowak¹⁰¹,
 M. Nozaki⁶⁶, L. Nozka¹¹⁵, K. Ntekas¹⁰, G. Nunes Hanninger⁸⁸, T. Nunnemann¹⁰⁰,

E. Nurse⁷⁸, F. Nuti⁸⁸, B.J. O'Brien⁴⁶, F. O'grady⁷, D.C. O'Neil¹⁴³, V. O'Shea⁵³,
 F.G. Oakham^{29,d}, H. Oberlack¹⁰¹, T. Obermann²¹, J. Ocariz⁸⁰, A. Ochi⁶⁷, I. Ochoa⁷⁸,
 S. Oda⁷⁰, S. Odaka⁶⁶, H. Ogren⁶¹, A. Oh⁸⁴, S.H. Oh⁴⁵, C.C. Ohm¹⁵, H. Ohman¹⁶⁷,
 H. Oide³⁰, W. Okamura¹¹⁸, H. Okawa¹⁶¹, Y. Okumura³¹, T. Okuyama¹⁵⁶, A. Olariu^{26a},
 S.A. Olivares Pino⁴⁶, D. Oliveira Damazio²⁵, E. Oliver Garcia¹⁶⁸, A. Olszewski³⁹,
 J. Olszowska³⁹, A. Onofre^{126a,126e}, P.U.E. Onyisi^{31,q}, C.J. Oram^{160a}, M.J. Oreglia³¹,
 Y. Oren¹⁵⁴, D. Orestano^{135a,135b}, N. Orlando¹⁵⁵, C. Oropeza Barrera⁵³, R.S. Orr¹⁵⁹,
 B. Osculati^{50a,50b}, R. Ospanov⁸⁴, G. Otero y Garzon²⁷, H. Otono⁷⁰, M. Ouchrif^{136d},
 E.A. Ouellette¹⁷⁰, F. Ould-Saada¹¹⁹, A. Ouraou¹³⁷, K.P. Oussoren¹⁰⁷, Q. Ouyang^{33a},
 A. Ovcharova¹⁵, M. Owen⁵³, R.E. Owen¹⁸, V.E. Ozcan^{19a}, N. Ozturk⁸, K. Pachal¹²⁰,
 A. Pacheco Pages¹², C. Padilla Aranda¹², M. Pagáčová⁴⁸, S. Pagan Griso¹⁵,
 E. Paganis¹⁴⁰, C. Pahl¹⁰¹, F. Paige²⁵, P. Pais⁸⁶, K. Pajchel¹¹⁹, G. Palacino^{160b},
 S. Palestini³⁰, M. Palka^{38b}, D. Pallin³⁴, A. Palma^{126a,126b}, Y.B. Pan¹⁷⁴,
 E. Panagiotopoulou¹⁰, C.E. Pandini⁸⁰, J.G. Panduro Vazquez⁷⁷, P. Pani^{147a,147b},
 N. Panikashvili⁸⁹, S. Panitkin²⁵, D. Pantea^{26a}, L. Paolozzi^{134a,134b},
 Th.D. Papadopoulou¹⁰, K. Papageorgiou¹⁵⁵, A. Paramonov⁶, D. Paredes Hernandez¹⁵⁵,
 M.A. Parker²⁸, K.A. Parker¹⁴⁰, F. Parodi^{50a,50b}, J.A. Parsons³⁵, U. Parzefall⁴⁸,
 E. Pasqualucci^{133a}, S. Passaggio^{50a}, F. Pastore^{135a,135b,*}, Fr. Pastore⁷⁷, G. Pásztor²⁹,
 S. Pataraiia¹⁷⁶, N.D. Patel¹⁵¹, J.R. Pater⁸⁴, T. Pauly³⁰, J. Pearce¹⁷⁰, B. Pearson¹¹³,
 L.E. Pedersen³⁶, M. Pedersen¹¹⁹, S. Pedraza Lopez¹⁶⁸, R. Pedro^{126a,126b},
 S.V. Peleganchuk^{109,c}, D. Pelikan¹⁶⁷, H. Peng^{33b}, B. Penning³¹, J. Penwell⁶¹,
 D.V. Perepelitsa²⁵, E. Perez Codina^{160a}, M.T. Pérez García-Estañ¹⁶⁸, L. Perini^{91a,91b},
 H. Pernegger³⁰, S. Perrella^{104a,104b}, R. Peschke⁴², V.D. Peshekhonov⁶⁵, K. Peters³⁰,
 R.F.Y. Peters⁸⁴, B.A. Petersen³⁰, T.C. Petersen³⁶, E. Petit⁴², A. Petridis^{147a,147b},
 C. Petridou¹⁵⁵, E. Petrolo^{133a}, F. Petrucci^{135a,135b}, N.E. Pettersson¹⁵⁸, R. Pezoa^{32b},
 P.W. Phillips¹³¹, G. Piacquadio¹⁴⁴, E. Pianori¹⁷¹, A. Picazio⁴⁹, E. Piccaro⁷⁶,
 M. Piccinini^{20a,20b}, M.A. Pickering¹²⁰, R. Piegaiia²⁷, D.T. Pignotti¹¹¹, J.E. Pilcher³¹,
 A.D. Pilkington⁷⁸, J. Pina^{126a,126b,126d}, M. Pinamonti^{165a,165c,ad}, J.L. Pinfeld³,
 A. Pingel³⁶, B. Pinto^{126a}, S. Pires⁸⁰, M. Pitt¹⁷³, C. Pizio^{91a,91b}, L. Plazak^{145a},
 M.-A. Pleier²⁵, V. Pleskot¹²⁹, E. Plotnikova⁶⁵, P. Plucinski^{147a,147b}, D. Pluth⁶⁴,
 R. Poettgen⁸³, L. Poggioli¹¹⁷, D. Pohl²¹, G. Polesello^{121a}, A. Policicchio^{37a,37b},
 R. Polifka¹⁵⁹, A. Polini^{20a}, C.S. Pollard⁵³, V. Polychronakos²⁵, K. Pommès³⁰,
 L. Pontecorvo^{133a}, B.G. Pope⁹⁰, G.A. Popeneciu^{26b}, D.S. Popovic¹³, A. Poppleton³⁰,
 S. Pospisil¹²⁸, K. Potamianos¹⁵, I.N. Potrap⁶⁵, C.J. Potter¹⁵⁰, C.T. Potter¹¹⁶,
 G. Poulard³⁰, J. Poveda³⁰, V. Pozdnyakov⁶⁵, P. Pralavorio⁸⁵, A. Pranko¹⁵, S. Prasad³⁰,
 S. Prell⁶⁴, D. Price⁸⁴, J. Price⁷⁴, L.E. Price⁶, M. Primavera^{73a}, S. Prince⁸⁷, M. Proissl⁴⁶,
 K. Prokofiev^{60c}, F. Prokoshin^{32b}, E. Protopapadaki¹³⁷, S. Protopopescu²⁵, J. Proudfoot⁶,
 M. Przybycien^{38a}, E. Ptacek¹¹⁶, D. PuDDu^{135a,135b}, E. Pueschel⁸⁶, D. Puldon¹⁴⁹,
 M. Purohit^{25,ae}, P. Puzo¹¹⁷, J. Qian⁸⁹, G. Qin⁵³, Y. Qin⁸⁴, A. Quadri⁵⁴, D.R. Quarrie¹⁵,
 W.B. Quayle^{165a,165b}, M. Queitsch-Maitland⁸⁴, D. Quilty⁵³, A. Qureshi^{160b}, V. Radeka²⁵,
 V. Radescu⁴², S.K. Radhakrishnan¹⁴⁹, P. Radloff¹¹⁶, P. Rados⁸⁸, F. Ragusa^{91a,91b},
 G. Rahal¹⁷⁹, S. Rajagopalan²⁵, M. Rammensee³⁰, C. Rangel-Smith¹⁶⁷, F. Rauscher¹⁰⁰,
 S. Rave⁸³, T.C. Rave⁴⁸, T. Ravenscroft⁵³, M. Raymond³⁰, A.L. Read¹¹⁹, N.P. Readioff⁷⁴,

D.M. Rebuzzi^{121a,121b}, A. Redelbach¹⁷⁵, G. Redlinger²⁵, R. Reece¹³⁸, K. Reeves⁴¹,
 L. Rehnisch¹⁶, H. Reisin²⁷, M. Relich¹⁶⁴, C. Rembser³⁰, H. Ren^{33a}, A. Renaud¹¹⁷,
 M. Rescigno^{133a}, S. Resconi^{91a}, O.L. Rezanova^{109,c}, P. Reznicek¹²⁹, R. Rezvani⁹⁵,
 R. Richter¹⁰¹, E. Richter-Was^{38b}, M. Ridel⁸⁰, P. Rieck¹⁶, C.J. Riegel¹⁷⁶, J. Rieger⁵⁴,
 M. Rijssenbeek¹⁴⁹, A. Rimoldi^{121a,121b}, L. Rinaldi^{20a}, E. Ritsch⁶², I. Riu¹²,
 F. Rizatdinova¹¹⁴, E. Rizvi⁷⁶, S.H. Robertson^{87,k}, A. Robichaud-Veronneau⁸⁷,
 D. Robinson²⁸, J.E.M. Robinson⁸⁴, A. Robson⁵³, C. Roda^{124a,124b}, L. Rodrigues³⁰,
 S. Roe³⁰, O. Røhne¹¹⁹, S. Rolli¹⁶², A. Romaniouk⁹⁸, M. Romano^{20a,20b},
 S.M. Romano Saez³⁴, E. Romero Adam¹⁶⁸, N. Rompotis¹³⁹, M. Ronzani⁴⁸, L. Roos⁸⁰,
 E. Ros¹⁶⁸, S. Rosati^{133a}, K. Rosbach⁴⁸, P. Rose¹³⁸, P.L. Rosendahl¹⁴, O. Rosenthal¹⁴²,
 V. Rossetti^{147a,147b}, E. Rossi^{104a,104b}, L.P. Rossi^{50a}, R. Rosten¹³⁹, M. Rotaru^{26a},
 I. Roth¹⁷³, J. Rothberg¹³⁹, D. Rousseau¹¹⁷, C.R. Royon¹³⁷, A. Rozanov⁸⁵, Y. Rozen¹⁵³,
 X. Ruan^{146c}, F. Rubbo¹⁴⁴, I. Rubinskiy⁴², V.I. Rud⁹⁹, C. Rudolph⁴⁴, M.S. Rudolph¹⁵⁹,
 F. Rühr⁴⁸, A. Ruiz-Martinez³⁰, Z. Rurikova⁴⁸, N.A. Rusakovich⁶⁵, A. Ruschke¹⁰⁰,
 H.L. Russell¹³⁹, J.P. Rutherford⁷, N. Ruthmann⁴⁸, Y.F. Ryabov¹²³, M. Rybar¹²⁹,
 G. Rybkin¹¹⁷, N.C. Ryder¹²⁰, A.F. Saavedra¹⁵¹, G. Sabato¹⁰⁷, S. Sacerdoti²⁷,
 A. Saddique³, H.F.W. Sadrozinski¹³⁸, R. Sadykov⁶⁵, F. Safai Tehrani^{133a},
 M. Saimpert¹³⁷, H. Sakamoto¹⁵⁶, Y. Sakurai¹⁷², G. Salamanna^{135a,135b}, A. Salamon^{134a},
 M. Saleem¹¹³, D. Salek¹⁰⁷, P.H. Sales De Bruin¹³⁹, D. Salihagic¹⁰¹, A. Salnikov¹⁴⁴,
 J. Salt¹⁶⁸, D. Salvatore^{37a,37b}, F. Salvatore¹⁵⁰, A. Salvucci¹⁰⁶, A. Salzburger³⁰,
 D. Sampsonidis¹⁵⁵, A. Sanchez^{104a,104b}, J. Sánchez¹⁶⁸, V. Sanchez Martinez¹⁶⁸,
 H. Sandaker¹⁴, R.L. Sandbach⁷⁶, H.G. Sander⁸³, M.P. Sanders¹⁰⁰, M. Sandhoff¹⁷⁶,
 C. Sandoval¹⁶³, R. Sandstroem¹⁰¹, D.P.C. Sankey¹³¹, A. Sansoni⁴⁷, C. Santoni³⁴,
 R. Santonico^{134a,134b}, H. Santos^{126a}, I. Santoyo Castillo¹⁵⁰, K. Sapp¹²⁵, A. Sapronov⁶⁵,
 J.G. Saraiva^{126a,126d}, B. Sarrazin²¹, O. Sasaki⁶⁶, Y. Sasaki¹⁵⁶, K. Sato¹⁶¹, G. Sauvage^{5,*},
 E. Sauvan⁵, G. Savage⁷⁷, P. Savard^{159,d}, C. Sawyer¹²⁰, L. Sawyer^{79,n}, D.H. Saxon⁵³,
 J. Saxon³¹, C. Sbarra^{20a}, A. Sbrizzi^{20a,20b}, T. Scanlon⁷⁸, D.A. Scannicchio¹⁶⁴,
 M. Scarcella¹⁵¹, V. Scarfone^{37a,37b}, J. Schaarschmidt¹⁷³, P. Schacht¹⁰¹, D. Schaefer³⁰,
 R. Schaefer⁴², J. Schaeffer⁸³, S. Schaepe²¹, S. Schaezel^{58b}, U. Schäfer⁸³, A.C. Schaffer¹¹⁷,
 D. Schaile¹⁰⁰, R.D. Schamberger¹⁴⁹, V. Scharf^{58a}, V.A. Schegelsky¹²³, D. Scheirich¹²⁹,
 M. Schernau¹⁶⁴, C. Schiavi^{50a,50b}, C. Schillo⁴⁸, M. Schioppa^{37a,37b}, S. Schlenker³⁰,
 E. Schmidt⁴⁸, K. Schmieden³⁰, C. Schmitt⁸³, S. Schmitt^{58b}, S. Schmitt⁴²,
 B. Schneider^{160a}, Y.J. Schnellbach⁷⁴, U. Schnoor⁴⁴, L. Schoeffel¹³⁷, A. Schoening^{58b},
 B.D. Schoenrock⁹⁰, A.L.S. Schorlemmer⁵⁴, M. Schott⁸³, D. Schouten^{160a}, J. Schovancova⁸,
 S. Schramm¹⁵⁹, M. Schreyer¹⁷⁵, C. Schroeder⁸³, N. Schuh⁸³, M.J. Schultens²¹,
 H.-C. Schultz-Coulon^{58a}, H. Schulz¹⁶, M. Schumacher⁴⁸, B.A. Schumm¹³⁸, Ph. Schune¹³⁷,
 C. Schwanenberger⁸⁴, A. Schwartzman¹⁴⁴, T.A. Schwarz⁸⁹, Ph. Schwegler¹⁰¹,
 Ph. Schwemling¹³⁷, R. Schwienhorst⁹⁰, J. Schwindling¹³⁷, T. Schwindt²¹, M. Schwoerer⁵,
 F.G. Sciacca¹⁷, E. Scifo¹¹⁷, G. Sciolla²³, F. Scuri^{124a,124b}, F. Scutti²¹, J. Searcy⁸⁹,
 G. Sedov⁴², E. Sedykh¹²³, P. Seema²¹, S.C. Seidel¹⁰⁵, A. Seiden¹³⁸, F. Seifert¹²⁸,
 J.M. Seixas^{24a}, G. Sekhniaidze^{104a}, S.J. Sekula⁴⁰, K.E. Selbach⁴⁶, D.M. Seliverstov^{123,*},
 N. Semprini-Cesari^{20a,20b}, C. Serfon³⁰, L. Serin¹¹⁷, L. Serkin⁵⁴, T. Serre⁸⁵, R. Seuster^{160a},
 H. Severini¹¹³, T. Sfiligoi⁷⁵, F. Sforza¹⁰¹, A. Sfyrla³⁰, E. Shabalina⁵⁴, M. Shamim¹¹⁶,

L.Y. Shan^{33a}, R. Shang¹⁶⁶, J.T. Shank²², M. Shapiro¹⁵, P.B. Shatalov⁹⁷, K. Shaw^{165a,165b},
 A. Shcherbakova^{147a,147b}, C.Y. Shehu¹⁵⁰, P. Sherwood⁷⁸, L. Shi^{152,af}, S. Shimizu⁶⁷,
 C.O. Shimmin¹⁶⁴, M. Shimojima¹⁰², M. Shiyakova⁶⁵, A. Shmeleva⁹⁶, D. Shoaleh Saadi⁹⁵,
 M.J. Shochet³¹, S. Shojaii^{91a,91b}, S. Shrestha¹¹¹, E. Shulga⁹⁸, M.A. Shupe⁷,
 S. Shushkevich⁴², P. Sicho¹²⁷, O. Sidiropoulou¹⁷⁵, D. Sidorov¹¹⁴, A. Sidoti^{20a,20b},
 F. Siegert⁴⁴, Dj. Sijacki¹³, J. Silva^{126a,126d}, Y. Silver¹⁵⁴, D. Silverstein¹⁴⁴,
 S.B. Silverstein^{147a}, V. Simak¹²⁸, O. Simard⁵, Lj. Simic¹³, S. Simion¹¹⁷, E. Simioni⁸³,
 B. Simmons⁷⁸, D. Simon³⁴, R. Simoniello^{91a,91b}, P. Sinervo¹⁵⁹, N.B. Sinev¹¹⁶,
 G. Siragusa¹⁷⁵, A. Sircar⁷⁹, A.N. Sisakyan^{65,*}, S.Yu. Sivoklov⁹⁹, J. Sjölin^{147a,147b},
 T.B. Sjursen¹⁴, M.B. Skinner⁷², H.P. Skottowe⁵⁷, P. Skubic¹¹³, M. Slater¹⁸,
 T. Slavicek¹²⁸, M. Slawinska¹⁰⁷, K. Sliwa¹⁶², V. Smakhtin¹⁷³, B.H. Smart⁴⁶, L. Smestad¹⁴,
 S.Yu. Smirnov⁹⁸, Y. Smirnov⁹⁸, L.N. Smirnova^{99,ag}, O. Smirnova⁸¹, K.M. Smith⁵³,
 M.N.K. Smith³⁵, M. Smizanska⁷², K. Smolek¹²⁸, A.A. Snesarev⁹⁶, G. Snidero⁷⁶,
 S. Snyder²⁵, R. Sobie^{170,k}, F. Socher⁴⁴, A. Soffer¹⁵⁴, D.A. Soh^{152,af}, C.A. Solans³⁰,
 M. Solar¹²⁸, J. Solc¹²⁸, E.Yu. Soldatov⁹⁸, U. Soldevila¹⁶⁸, A.A. Solodkov¹³⁰,
 A. Soloshenko⁶⁵, O.V. Solovyanov¹³⁰, V. Solovyev¹²³, P. Sommer⁴⁸, H.Y. Song^{33b},
 N. Soni¹, A. Sood¹⁵, A. Sopczak¹²⁸, B. Sopko¹²⁸, V. Sopko¹²⁸, V. Sorin¹², D. Sosa^{58b},
 M. Sosebee⁸, C.L. Sotiropoulou¹⁵⁵, R. Soualah^{165a,165c}, P. Soueid⁹⁵, A.M. Soukharev^{109,c},
 D. South⁴², S. Spagnolo^{73a,73b}, F. Spanò⁷⁷, W.R. Spearman⁵⁷, F. Spettel¹⁰¹, R. Spighi^{20a},
 G. Spigo³⁰, L.A. Spiller⁸⁸, M. Spousta¹²⁹, T. Spreitzer¹⁵⁹, R.D. St. Denis^{53,*}, S. Staerz⁴⁴,
 J. Stahlman¹²², R. Stamen^{58a}, S. Stamm¹⁶, E. Stanecka³⁹, C. Stanescu^{135a},
 M. Stanescu-Bellu⁴², M.M. Stanitzki⁴², S. Stapnes¹¹⁹, E.A. Starchenko¹³⁰, J. Stark⁵⁵,
 P. Staroba¹²⁷, P. Starovoitov⁴², R. Staszewski³⁹, P. Stavina^{145a,*}, P. Steinberg²⁵,
 B. Stelzer¹⁴³, H.J. Stelzer³⁰, O. Stelzer-Chilton^{160a}, H. Stenzel⁵², S. Stern¹⁰¹,
 G.A. Stewart⁵³, J.A. Stillings²¹, M.C. Stockton⁸⁷, M. Stoebe⁸⁷, G. Stoicea^{26a}, P. Stolte⁵⁴,
 S. Stonjek¹⁰¹, A.R. Stradling⁸, A. Straessner⁴⁴, M.E. Stramaglia¹⁷, J. Strandberg¹⁴⁸,
 S. Strandberg^{147a,147b}, A. Strandlie¹¹⁹, E. Strauss¹⁴⁴, M. Strauss¹¹³, P. Strizeneč^{145b},
 R. Ströhmer¹⁷⁵, D.M. Strom¹¹⁶, R. Stroynowski⁴⁰, A. Strubig¹⁰⁶, S.A. Stucci¹⁷,
 B. Stugu¹⁴, N.A. Styles⁴², D. Su¹⁴⁴, J. Su¹²⁵, R. Subramaniam⁷⁹, A. Succurro¹²,
 Y. Sugaya¹¹⁸, C. Suhr¹⁰⁸, M. Suk¹²⁸, V.V. Sulin⁹⁶, S. Sultansoy^{4d}, T. Sumida⁶⁸, S. Sun⁵⁷,
 X. Sun^{33a}, J.E. Sundermann⁴⁸, K. Suruliz¹⁵⁰, G. Susinno^{37a,37b}, M.R. Sutton¹⁵⁰,
 Y. Suzuki⁶⁶, M. Svatos¹²⁷, S. Swedish¹⁶⁹, M. Swiatlowski¹⁴⁴, I. Sykora^{145a}, T. Sykora¹²⁹,
 D. Ta⁹⁰, C. Taccini^{135a,135b}, K. Tackmann⁴², J. Taenzer¹⁵⁹, A. Taffard¹⁶⁴, R. Tafirout^{160a},
 N. Taiblum¹⁵⁴, H. Takai²⁵, R. Takashima⁶⁹, H. Takeda⁶⁷, T. Takeshita¹⁴¹, Y. Takubo⁶⁶,
 M. Talby⁸⁵, A.A. Talyshev^{109,c}, J.Y.C. Tam¹⁷⁵, K.G. Tan⁸⁸, J. Tanaka¹⁵⁶, R. Tanaka¹¹⁷,
 S. Tanaka¹³², S. Tanaka⁶⁶, A.J. Tanasijczuk¹⁴³, B.B. Tannenwald¹¹¹, N. Tannoury²¹,
 S. Tapprogge⁸³, S. Tarem¹⁵³, F. Tarrade²⁹, G.F. Tartarelli^{91a}, P. Tas¹²⁹, M. Tasevsky¹²⁷,
 T. Tashiro⁶⁸, E. Tassi^{37a,37b}, A. Tavares Delgado^{126a,126b}, Y. Tayalati^{136d}, F.E. Taylor⁹⁴,
 G.N. Taylor⁸⁸, W. Taylor^{160b}, F.A. Teischinger³⁰, M. Teixeira Dias Castanheira⁷⁶,
 P. Teixeira-Dias⁷⁷, K.K. Temming⁴⁸, H. Ten Kate³⁰, P.K. Teng¹⁵², J.J. Teoh¹¹⁸,
 F. Tepel¹⁷⁶, S. Terada⁶⁶, K. Terashi¹⁵⁶, J. Terron⁸², S. Terzo¹⁰¹, M. Testa⁴⁷,
 R.J. Teuscher^{159,k}, J. Therhaag²¹, T. Theveneaux-Pelzer³⁴, J.P. Thomas¹⁸,
 J. Thomas-Wilsker⁷⁷, E.N. Thompson³⁵, P.D. Thompson¹⁸, R.J. Thompson⁸⁴,

A.S. Thompson⁵³, L.A. Thomsen³⁶, E. Thomson¹²², M. Thomson²⁸, W.M. Thong⁸⁸,
 R.P. Thun^{89,*}, F. Tian³⁵, M.J. Tibbetts¹⁵, R.E. Ticse Torres⁸⁵, V.O. Tikhomirov^{96,ah},
 Yu.A. Tikhonov^{109,c}, S. Timoshenko⁹⁸, E. Tiouchichine⁸⁵, P. Tipton¹⁷⁷, S. Tisserant⁸⁵,
 T. Todorov^{5,*}, S. Todorova-Nova¹²⁹, J. Tojo⁷⁰, S. Tokár^{145a}, K. Tokushuku⁶⁶,
 K. Tollefson⁹⁰, E. Tolley⁵⁷, L. Tomlinson⁸⁴, M. Tomoto¹⁰³, L. Tompkins^{144,ai},
 K. Toms¹⁰⁵, E. Torrence¹¹⁶, H. Torres¹⁴³, E. Torró Pastor¹⁶⁸, J. Toth^{85,aj}, F. Touchard⁸⁵,
 D.R. Tovey¹⁴⁰, H.L. Tran¹¹⁷, T. Trefzger¹⁷⁵, L. Tremblet³⁰, A. Tricoli³⁰, I.M. Trigger^{160a},
 S. Trincaz-Duvoid⁸⁰, M.F. Tripiana¹², W. Trischuk¹⁵⁹, B. Trocmé⁵⁵, C. Troncon^{91a},
 M. Trotter-McDonald¹⁵, M. Trovatelli^{135a,135b}, P. True⁹⁰, M. Trzebinski³⁹, A. Trzuppek³⁹,
 C. Tsarouchas³⁰, J.C-L. Tseng¹²⁰, P.V. Tsiareshka⁹², D. Tsionou¹⁵⁵, G. Tsipolitis¹⁰,
 N. Tsirintanis⁹, S. Tsiskaridze¹², V. Tsiskaridze⁴⁸, E.G. Tskhadadze^{51a}, I.I. Tsukerman⁹⁷,
 V. Tsulaia¹⁵, S. Tsuno⁶⁶, D. Tsybychev¹⁴⁹, A. Tudorache^{26a}, V. Tudorache^{26a},
 A.N. Tuna¹²², S.A. Tuppuri^{20a,20b}, S. Turchikhin^{99,ag}, D. Turecek¹²⁸, R. Turra^{91a,91b},
 A.J. Turvey⁴⁰, P.M. Tuts³⁵, A. Tykhonov⁴⁹, M. Tylmad^{147a,147b}, M. Tyndel¹³¹,
 I. Ueda¹⁵⁶, R. Ueno²⁹, M. Ughetto^{147a,147b}, M. Ugland¹⁴, M. Uhlenbrock²¹,
 F. Ukegawa¹⁶¹, G. Unal³⁰, A. Undrus²⁵, G. Unel¹⁶⁴, F.C. Ungaro⁴⁸, Y. Unno⁶⁶,
 C. Unverdorben¹⁰⁰, J. Urban^{145b}, P. Urquijo⁸⁸, P. Urrejola⁸³, G. Usai⁸, A. Usanova⁶²,
 L. Vacavant⁸⁵, V. Vacek¹²⁸, B. Vachon⁸⁷, N. Valencic¹⁰⁷, S. Valentinetti^{20a,20b},
 A. Valero¹⁶⁸, L. Valery¹², S. Valkar¹²⁹, E. Valladolid Gallego¹⁶⁸, S. Vallecorsa⁴⁹,
 J.A. Valls Ferrer¹⁶⁸, W. Van Den Wollenberg¹⁰⁷, P.C. Van Der Deijl¹⁰⁷,
 R. van der Geer¹⁰⁷, H. van der Graaf¹⁰⁷, R. Van Der Leeuw¹⁰⁷, N. van Eldik³⁰,
 P. van Gemmeren⁶, J. Van Nieuwkoop¹⁴³, I. van Vulpen¹⁰⁷, M.C. van Woerden³⁰,
 M. Vanadia^{133a,133b}, W. Vandelli³⁰, R. Vanguri¹²², A. Vaniachine⁶, F. Vannucci⁸⁰,
 G. Vardanyan¹⁷⁸, R. Vari^{133a}, E.W. Varnes⁷, T. Varol⁴⁰, D. Varouchas⁸⁰, A. Vartapetian⁸,
 K.E. Varvell¹⁵¹, F. Vazeille³⁴, T. Vazquez Schroeder⁵⁴, J. Veatch⁷, F. Veloso^{126a,126c},
 T. Velz²¹, S. Veneziano^{133a}, A. Ventura^{73a,73b}, D. Ventura⁸⁶, M. Venturi¹⁷⁰, N. Venturi¹⁵⁹,
 A. Venturini²³, V. Vercesi^{121a}, M. Verducci^{133a,133b}, W. Verkerke¹⁰⁷, J.C. Vermeulen¹⁰⁷,
 A. Vest⁴⁴, M.C. Vetterli^{143,d}, O. Viazlo⁸¹, I. Vichou¹⁶⁶, T. Vickey^{146c,ak},
 O.E. Vickey Boeriu^{146c}, G.H.A. Viehhauser¹²⁰, S. Viel¹⁵, R. Vigne³⁰, M. Villa^{20a,20b},
 M. Villaplana Perez^{91a,91b}, E. Vilucchi⁴⁷, M.G. Vincter²⁹, V.B. Vinogradov⁶⁵, J. Virzi¹⁵,
 I. Vivarelli¹⁵⁰, F. Vives Vaque³, S. Vlachos¹⁰, D. Vladoiu¹⁰⁰, M. Vlasak¹²⁸, M. Vogel^{32a},
 P. Vokac¹²⁸, G. Volpi^{124a,124b}, M. Volpi⁸⁸, H. von der Schmitt¹⁰¹, H. von Radziewski⁴⁸,
 E. von Toerne²¹, V. Vorobel¹²⁹, K. Vorobev⁹⁸, M. Vos¹⁶⁸, R. Voss³⁰, J.H. Vosseveld⁷⁴,
 N. Vranjes¹³, M. Vranjes Milosavljevic¹³, V. Vrba¹²⁷, M. Vreeswijk¹⁰⁷, R. Vuillemet³⁰,
 I. Vukotic³¹, Z. Vykydal¹²⁸, P. Wagner²¹, W. Wagner¹⁷⁶, H. Wahlberg⁷¹, S. Wahrmund⁴⁴,
 J. Wakabayashi¹⁰³, J. Walder⁷², R. Walker¹⁰⁰, W. Walkowiak¹⁴², C. Wang^{33c},
 F. Wang¹⁷⁴, H. Wang¹⁵, H. Wang⁴⁰, J. Wang⁴², J. Wang^{33a}, K. Wang⁸⁷, R. Wang¹⁰⁵,
 S.M. Wang¹⁵², T. Wang²¹, X. Wang¹⁷⁷, C. Wanotayaroj¹¹⁶, A. Warburton⁸⁷,
 C.P. Ward²⁸, D.R. Wardrope⁷⁸, M. Warsinsky⁴⁸, A. Washbrook⁴⁶, C. Wasicki⁴²,
 P.M. Watkins¹⁸, A.T. Watson¹⁸, I.J. Watson¹⁵¹, M.F. Watson¹⁸, G. Watts¹³⁹, S. Watts⁸⁴,
 B.M. Waugh⁷⁸, S. Webb⁸⁴, M.S. Weber¹⁷, S.W. Weber¹⁷⁵, J.S. Webster³¹,
 A.R. Weidberg¹²⁰, B. Weinert⁶¹, J. Weingarten⁵⁴, C. Weiser⁴⁸, H. Weits¹⁰⁷, P.S. Wells³⁰,
 T. Wenaus²⁵, D. Wendland¹⁶, T. Wengler³⁰, S. Wenig³⁰, N. Wermes²¹, M. Werner⁴⁸,

P. Werner³⁰, M. Wessels^{58a}, J. Wetter¹⁶², K. Whalen²⁹, A.M. Wharton⁷², A. White⁸, M.J. White¹, R. White^{32b}, S. White^{124a,124b}, D. Whiteson¹⁶⁴, D. Wicke¹⁷⁶, F.J. Wickens¹³¹, W. Wiedenmann¹⁷⁴, M. Wielers¹³¹, P. Wienemann²¹, C. Wiglesworth³⁶, L.A.M. Wiik-Fuchs²¹, A. Wildauer¹⁰¹, H.G. Wilkens³⁰, H.H. Williams¹²², S. Williams¹⁰⁷, C. Willis⁹⁰, S. Willocq⁸⁶, A. Wilson⁸⁹, J.A. Wilson¹⁸, I. Wingerter-Seez⁵, F. Winklmeier¹¹⁶, B.T. Winter²¹, M. Wittgen¹⁴⁴, J. Wittkowski¹⁰⁰, S.J. Wollstadt⁸³, M.W. Wolter³⁹, H. Wolters^{126a,126c}, B.K. Wosiek³⁹, J. Wotschack³⁰, M.J. Woudstra⁸⁴, K.W. Wozniak³⁹, M. Wu⁵⁵, M. Wu³¹, S.L. Wu¹⁷⁴, X. Wu⁴⁹, Y. Wu⁸⁹, T.R. Wyatt⁸⁴, B.M. Wynne⁴⁶, S. Xella³⁶, D. Xu^{33a}, L. Xu^{33b,al}, B. Yabsley¹⁵¹, S. Yacooob^{146b,am}, R. Yakabe⁶⁷, M. Yamada⁶⁶, Y. Yamaguchi¹¹⁸, A. Yamamoto⁶⁶, S. Yamamoto¹⁵⁶, T. Yamanaka¹⁵⁶, K. Yamauchi¹⁰³, Y. Yamazaki⁶⁷, Z. Yan²², H. Yang^{33e}, H. Yang¹⁷⁴, Y. Yang¹⁵², S. Yanush⁹³, L. Yao^{33a}, W-M. Yao¹⁵, Y. Yasu⁶⁶, E. Yatsenko⁴², K.H. Yau Wong²¹, J. Ye⁴⁰, S. Ye²⁵, I. Yeletsikh⁶⁵, A.L. Yen⁵⁷, E. Yildirim⁴², K. Yorita¹⁷², R. Yoshida⁶, K. Yoshihara¹²², C. Young¹⁴⁴, C.J.S. Young³⁰, S. Youssef²², D.R. Yu¹⁵, J. Yu⁸, J.M. Yu⁸⁹, J. Yu¹¹⁴, L. Yuan⁶⁷, A. Yurkewicz¹⁰⁸, I. Yusuff^{28,an}, B. Zabinski³⁹, R. Zaidan⁶³, A.M. Zaitsev^{130,ab}, A. Zaman¹⁴⁹, S. Zambito²³, L. Zanello^{133a,133b}, D. Zanzi⁸⁸, C. Zeitnitz¹⁷⁶, M. Zeman¹²⁸, A. Zemla^{38a}, K. Zengel²³, O. Zenin¹³⁰, T. Ženiš^{145a}, D. Zerwas¹¹⁷, D. Zhang⁸⁹, F. Zhang¹⁷⁴, J. Zhang⁶, L. Zhang¹⁵², R. Zhang^{33b}, X. Zhang^{33d}, Z. Zhang¹¹⁷, X. Zhao⁴⁰, Y. Zhao^{33d,117}, Z. Zhao^{33b}, A. Zhemchugov⁶⁵, J. Zhong¹²⁰, B. Zhou⁸⁹, C. Zhou⁴⁵, L. Zhou³⁵, L. Zhou⁴⁰, N. Zhou¹⁶⁴, C.G. Zhu^{33d}, H. Zhu^{33a}, J. Zhu⁸⁹, Y. Zhu^{33b}, X. Zhuang^{33a}, K. Zhukov⁹⁶, A. Zibell¹⁷⁵, D. Zieminska⁶¹, N.I. Zimine⁶⁵, C. Zimmermann⁸³, R. Zimmermann²¹, S. Zimmermann⁴⁸, Z. Zinonos⁵⁴, M. Zinser⁸³, M. Ziolkowski¹⁴², L. Živković¹³, G. Zobernig¹⁷⁴, A. Zoccoli^{20a,20b}, M. zur Nedden¹⁶, G. Zurzolo^{104a,104b}, L. Zwalinski³⁰.

¹ Department of Physics, University of Adelaide, Adelaide, Australia

² Physics Department, SUNY Albany, Albany NY, United States of America

³ Department of Physics, University of Alberta, Edmonton AB, Canada

⁴ ^(a) Department of Physics, Ankara University, Ankara; ^(c) Istanbul Aydin University, Istanbul; ^(d) Division of Physics, TOBB University of Economics and Technology, Ankara, Turkey

⁵ LAPP, CNRS/IN2P3 and Université Savoie Mont Blanc, Annecy-le-Vieux, France

⁶ High Energy Physics Division, Argonne National Laboratory, Argonne IL, United States of America

⁷ Department of Physics, University of Arizona, Tucson AZ, United States of America

⁸ Department of Physics, The University of Texas at Arlington, Arlington TX, United States of America

⁹ Physics Department, University of Athens, Athens, Greece

¹⁰ Physics Department, National Technical University of Athens, Zografou, Greece

¹¹ Institute of Physics, Azerbaijan Academy of Sciences, Baku, Azerbaijan

¹² Institut de Física d'Altes Energies and Departament de Física de la Universitat Autònoma de Barcelona, Barcelona, Spain

¹³ Institute of Physics, University of Belgrade, Belgrade, Serbia

- ¹⁴ Department for Physics and Technology, University of Bergen, Bergen, Norway
- ¹⁵ Physics Division, Lawrence Berkeley National Laboratory and University of California, Berkeley CA, United States of America
- ¹⁶ Department of Physics, Humboldt University, Berlin, Germany
- ¹⁷ Albert Einstein Center for Fundamental Physics and Laboratory for High Energy Physics, University of Bern, Bern, Switzerland
- ¹⁸ School of Physics and Astronomy, University of Birmingham, Birmingham, United Kingdom
- ¹⁹ ^(a) Department of Physics, Bogazici University, Istanbul; ^(b) Department of Physics, Dogus University, Istanbul; ^(c) Department of Physics Engineering, Gaziantep University, Gaziantep, Turkey
- ²⁰ ^(a) INFN Sezione di Bologna; ^(b) Dipartimento di Fisica e Astronomia, Università di Bologna, Bologna, Italy
- ²¹ Physikalisches Institut, University of Bonn, Bonn, Germany
- ²² Department of Physics, Boston University, Boston MA, United States of America
- ²³ Department of Physics, Brandeis University, Waltham MA, United States of America
- ²⁴ ^(a) Universidade Federal do Rio De Janeiro COPPE/EE/IF, Rio de Janeiro; ^(b) Electrical Circuits Department, Federal University of Juiz de Fora (UFJF), Juiz de Fora; ^(c) Federal University of Sao Joao del Rei (UFSJ), Sao Joao del Rei; ^(d) Instituto de Fisica, Universidade de Sao Paulo, Sao Paulo, Brazil
- ²⁵ Physics Department, Brookhaven National Laboratory, Upton NY, United States of America
- ²⁶ ^(a) National Institute of Physics and Nuclear Engineering, Bucharest; ^(b) National Institute for Research and Development of Isotopic and Molecular Technologies, Physics Department, Cluj Napoca; ^(c) University Politehnica Bucharest, Bucharest; ^(d) West University in Timisoara, Timisoara, Romania
- ²⁷ Departamento de Física, Universidad de Buenos Aires, Buenos Aires, Argentina
- ²⁸ Cavendish Laboratory, University of Cambridge, Cambridge, United Kingdom
- ²⁹ Department of Physics, Carleton University, Ottawa ON, Canada
- ³⁰ CERN, Geneva, Switzerland
- ³¹ Enrico Fermi Institute, University of Chicago, Chicago IL, United States of America
- ³² ^(a) Departamento de Física, Pontificia Universidad Católica de Chile, Santiago; ^(b) Departamento de Física, Universidad Técnica Federico Santa María, Valparaíso, Chile
- ³³ ^(a) Institute of High Energy Physics, Chinese Academy of Sciences, Beijing; ^(b) Department of Modern Physics, University of Science and Technology of China, Anhui; ^(c) Department of Physics, Nanjing University, Jiangsu; ^(d) School of Physics, Shandong University, Shandong; ^(e) Department of Physics and Astronomy, Shanghai Key Laboratory for Particle Physics and Cosmology, Shanghai Jiao Tong University, Shanghai; ^(f) Physics Department, Tsinghua University, Beijing 100084, China
- ³⁴ Laboratoire de Physique Corpusculaire, Clermont Université and Université Blaise Pascal and CNRS/IN2P3, Clermont-Ferrand, France
- ³⁵ Nevis Laboratory, Columbia University, Irvington NY, United States of America
- ³⁶ Niels Bohr Institute, University of Copenhagen, Kobenhavn, Denmark

- ³⁷ (a) INFN Gruppo Collegato di Cosenza, Laboratori Nazionali di Frascati; (b) Dipartimento di Fisica, Università della Calabria, Rende, Italy
- ³⁸ (a) AGH University of Science and Technology, Faculty of Physics and Applied Computer Science, Krakow; (b) Marian Smoluchowski Institute of Physics, Jagiellonian University, Krakow, Poland
- ³⁹ Institute of Nuclear Physics Polish Academy of Sciences, Krakow, Poland
- ⁴⁰ Physics Department, Southern Methodist University, Dallas TX, United States of America
- ⁴¹ Physics Department, University of Texas at Dallas, Richardson TX, United States of America
- ⁴² DESY, Hamburg and Zeuthen, Germany
- ⁴³ Institut für Experimentelle Physik IV, Technische Universität Dortmund, Dortmund, Germany
- ⁴⁴ Institut für Kern- und Teilchenphysik, Technische Universität Dresden, Dresden, Germany
- ⁴⁵ Department of Physics, Duke University, Durham NC, United States of America
- ⁴⁶ SUPA - School of Physics and Astronomy, University of Edinburgh, Edinburgh, United Kingdom
- ⁴⁷ INFN Laboratori Nazionali di Frascati, Frascati, Italy
- ⁴⁸ Fakultät für Mathematik und Physik, Albert-Ludwigs-Universität, Freiburg, Germany
- ⁴⁹ Section de Physique, Université de Genève, Geneva, Switzerland
- ⁵⁰ (a) INFN Sezione di Genova; (b) Dipartimento di Fisica, Università di Genova, Genova, Italy
- ⁵¹ (a) E. Andronikashvili Institute of Physics, Iv. Javakhishvili Tbilisi State University, Tbilisi; (b) High Energy Physics Institute, Tbilisi State University, Tbilisi, Georgia
- ⁵² II Physikalisches Institut, Justus-Liebig-Universität Giessen, Giessen, Germany
- ⁵³ SUPA - School of Physics and Astronomy, University of Glasgow, Glasgow, United Kingdom
- ⁵⁴ II Physikalisches Institut, Georg-August-Universität, Göttingen, Germany
- ⁵⁵ Laboratoire de Physique Subatomique et de Cosmologie, Université Grenoble-Alpes, CNRS/IN2P3, Grenoble, France
- ⁵⁶ Department of Physics, Hampton University, Hampton VA, United States of America
- ⁵⁷ Laboratory for Particle Physics and Cosmology, Harvard University, Cambridge MA, United States of America
- ⁵⁸ (a) Kirchhoff-Institut für Physik, Ruprecht-Karls-Universität Heidelberg, Heidelberg; (b) Physikalisches Institut, Ruprecht-Karls-Universität Heidelberg, Heidelberg; (c) ZITI Institut für technische Informatik, Ruprecht-Karls-Universität Heidelberg, Mannheim, Germany
- ⁵⁹ Faculty of Applied Information Science, Hiroshima Institute of Technology, Hiroshima, Japan
- ⁶⁰ (a) Department of Physics, The Chinese University of Hong Kong, Shatin, N.T., Hong Kong; (b) Department of Physics, The University of Hong Kong, Hong Kong; (c) Department of Physics, The Hong Kong University of Science and Technology, Clear

Water Bay, Kowloon, Hong Kong, China

⁶¹ Department of Physics, Indiana University, Bloomington IN, United States of America

⁶² Institut für Astro- und Teilchenphysik, Leopold-Franzens-Universität, Innsbruck, Austria

⁶³ University of Iowa, Iowa City IA, United States of America

⁶⁴ Department of Physics and Astronomy, Iowa State University, Ames IA, United States of America

⁶⁵ Joint Institute for Nuclear Research, JINR Dubna, Dubna, Russia

⁶⁶ KEK, High Energy Accelerator Research Organization, Tsukuba, Japan

⁶⁷ Graduate School of Science, Kobe University, Kobe, Japan

⁶⁸ Faculty of Science, Kyoto University, Kyoto, Japan

⁶⁹ Kyoto University of Education, Kyoto, Japan

⁷⁰ Department of Physics, Kyushu University, Fukuoka, Japan

⁷¹ Instituto de Física La Plata, Universidad Nacional de La Plata and CONICET, La Plata, Argentina

⁷² Physics Department, Lancaster University, Lancaster, United Kingdom

⁷³ ^(a) INFN Sezione di Lecce; ^(b) Dipartimento di Matematica e Fisica, Università del Salento, Lecce, Italy

⁷⁴ Oliver Lodge Laboratory, University of Liverpool, Liverpool, United Kingdom

⁷⁵ Department of Physics, Jožef Stefan Institute and University of Ljubljana, Ljubljana, Slovenia

⁷⁶ School of Physics and Astronomy, Queen Mary University of London, London, United Kingdom

⁷⁷ Department of Physics, Royal Holloway University of London, Surrey, United Kingdom

⁷⁸ Department of Physics and Astronomy, University College London, London, United Kingdom

⁷⁹ Louisiana Tech University, Ruston LA, United States of America

⁸⁰ Laboratoire de Physique Nucléaire et de Hautes Energies, UPMC and Université Paris-Diderot and CNRS/IN2P3, Paris, France

⁸¹ Fysiska institutionen, Lunds universitet, Lund, Sweden

⁸² Departamento de Física Teórica C-15, Universidad Autónoma de Madrid, Madrid, Spain

⁸³ Institut für Physik, Universität Mainz, Mainz, Germany

⁸⁴ School of Physics and Astronomy, University of Manchester, Manchester, United Kingdom

⁸⁵ CPPM, Aix-Marseille Université and CNRS/IN2P3, Marseille, France

⁸⁶ Department of Physics, University of Massachusetts, Amherst MA, United States of America

⁸⁷ Department of Physics, McGill University, Montreal QC, Canada

⁸⁸ School of Physics, University of Melbourne, Victoria, Australia

⁸⁹ Department of Physics, The University of Michigan, Ann Arbor MI, United States of America

⁹⁰ Department of Physics and Astronomy, Michigan State University, East Lansing MI,

United States of America

⁹¹ ^(a) INFN Sezione di Milano; ^(b) Dipartimento di Fisica, Università di Milano, Milano, Italy

⁹² B.I. Stepanov Institute of Physics, National Academy of Sciences of Belarus, Minsk, Republic of Belarus

⁹³ National Scientific and Educational Centre for Particle and High Energy Physics, Minsk, Republic of Belarus

⁹⁴ Department of Physics, Massachusetts Institute of Technology, Cambridge MA, United States of America

⁹⁵ Group of Particle Physics, University of Montreal, Montreal QC, Canada

⁹⁶ P.N. Lebedev Institute of Physics, Academy of Sciences, Moscow, Russia

⁹⁷ Institute for Theoretical and Experimental Physics (ITEP), Moscow, Russia

⁹⁸ National Research Nuclear University MEPhI, Moscow, Russia

⁹⁹ D.V. Skobeltsyn Institute of Nuclear Physics, M.V. Lomonosov Moscow State University, Moscow, Russia

¹⁰⁰ Fakultät für Physik, Ludwig-Maximilians-Universität München, München, Germany

¹⁰¹ Max-Planck-Institut für Physik (Werner-Heisenberg-Institut), München, Germany

¹⁰² Nagasaki Institute of Applied Science, Nagasaki, Japan

¹⁰³ Graduate School of Science and Kobayashi-Maskawa Institute, Nagoya University, Nagoya, Japan

¹⁰⁴ ^(a) INFN Sezione di Napoli; ^(b) Dipartimento di Fisica, Università di Napoli, Napoli, Italy

¹⁰⁵ Department of Physics and Astronomy, University of New Mexico, Albuquerque NM, United States of America

¹⁰⁶ Institute for Mathematics, Astrophysics and Particle Physics, Radboud University Nijmegen/Nikhef, Nijmegen, Netherlands

¹⁰⁷ Nikhef National Institute for Subatomic Physics and University of Amsterdam, Amsterdam, Netherlands

¹⁰⁸ Department of Physics, Northern Illinois University, DeKalb IL, United States of America

¹⁰⁹ Budker Institute of Nuclear Physics, SB RAS, Novosibirsk, Russia

¹¹⁰ Department of Physics, New York University, New York NY, United States of America

¹¹¹ Ohio State University, Columbus OH, United States of America

¹¹² Faculty of Science, Okayama University, Okayama, Japan

¹¹³ Homer L. Dodge Department of Physics and Astronomy, University of Oklahoma, Norman OK, United States of America

¹¹⁴ Department of Physics, Oklahoma State University, Stillwater OK, United States of America

¹¹⁵ Palacký University, RCPTM, Olomouc, Czech Republic

¹¹⁶ Center for High Energy Physics, University of Oregon, Eugene OR, United States of America

¹¹⁷ LAL, Université Paris-Sud and CNRS/IN2P3, Orsay, France

¹¹⁸ Graduate School of Science, Osaka University, Osaka, Japan

- 119 Department of Physics, University of Oslo, Oslo, Norway
- 120 Department of Physics, Oxford University, Oxford, United Kingdom
- 121 ^(a) INFN Sezione di Pavia; ^(b) Dipartimento di Fisica, Università di Pavia, Pavia, Italy
- 122 Department of Physics, University of Pennsylvania, Philadelphia PA, United States of America
- 123 National Research Centre "Kurchatov Institute" B.P.Konstantinov Petersburg Nuclear Physics Institute, St. Petersburg, Russia
- 124 ^(a) INFN Sezione di Pisa; ^(b) Dipartimento di Fisica E. Fermi, Università di Pisa, Pisa, Italy
- 125 Department of Physics and Astronomy, University of Pittsburgh, Pittsburgh PA, United States of America
- 126 ^(a) Laboratório de Instrumentação e Física Experimental de Partículas - LIP, Lisboa; ^(b) Faculdade de Ciências, Universidade de Lisboa, Lisboa; ^(c) Department of Physics, University of Coimbra, Coimbra; ^(d) Centro de Física Nuclear da Universidade de Lisboa, Lisboa; ^(e) Departamento de Física, Universidade do Minho, Braga; ^(f) Departamento de Física Teórica y del Cosmos and CAFPE, Universidad de Granada, Granada (Spain); ^(g) Dep Física and CEFITEC of Faculdade de Ciências e Tecnologia, Universidade Nova de Lisboa, Caparica, Portugal
- 127 Institute of Physics, Academy of Sciences of the Czech Republic, Praha, Czech Republic
- 128 Czech Technical University in Prague, Praha, Czech Republic
- 129 Faculty of Mathematics and Physics, Charles University in Prague, Praha, Czech Republic
- 130 State Research Center Institute for High Energy Physics, Protvino, Russia
- 131 Particle Physics Department, Rutherford Appleton Laboratory, Didcot, United Kingdom
- 132 Ritsumeikan University, Kusatsu, Shiga, Japan
- 133 ^(a) INFN Sezione di Roma; ^(b) Dipartimento di Fisica, Sapienza Università di Roma, Roma, Italy
- 134 ^(a) INFN Sezione di Roma Tor Vergata; ^(b) Dipartimento di Fisica, Università di Roma Tor Vergata, Roma, Italy
- 135 ^(a) INFN Sezione di Roma Tre; ^(b) Dipartimento di Matematica e Fisica, Università Roma Tre, Roma, Italy
- 136 ^(a) Faculté des Sciences Ain Chock, Réseau Universitaire de Physique des Hautes Energies - Université Hassan II, Casablanca; ^(b) Centre National de l'Energie des Sciences Techniques Nucleaires, Rabat; ^(c) Faculté des Sciences Semlalia, Université Cadi Ayyad, LPHEA-Marrakech; ^(d) Faculté des Sciences, Université Mohamed Premier and LTPM, Oujda; ^(e) Faculté des sciences, Université Mohammed V-Agdal, Rabat, Morocco
- 137 DSM/IRFU (Institut de Recherches sur les Lois Fondamentales de l'Univers), CEA Saclay (Commissariat à l'Energie Atomique et aux Energies Alternatives), Gif-sur-Yvette, France
- 138 Santa Cruz Institute for Particle Physics, University of California Santa Cruz, Santa Cruz CA, United States of America

- 139 Department of Physics, University of Washington, Seattle WA, United States of America
- 140 Department of Physics and Astronomy, University of Sheffield, Sheffield, United Kingdom
- 141 Department of Physics, Shinshu University, Nagano, Japan
- 142 Fachbereich Physik, Universität Siegen, Siegen, Germany
- 143 Department of Physics, Simon Fraser University, Burnaby BC, Canada
- 144 SLAC National Accelerator Laboratory, Stanford CA, United States of America
- 145 ^(a) Faculty of Mathematics, Physics & Informatics, Comenius University, Bratislava; ^(b) Department of Subnuclear Physics, Institute of Experimental Physics of the Slovak Academy of Sciences, Kosice, Slovak Republic
- 146 ^(a) Department of Physics, University of Cape Town, Cape Town; ^(b) Department of Physics, University of Johannesburg, Johannesburg; ^(c) School of Physics, University of the Witwatersrand, Johannesburg, South Africa
- 147 ^(a) Department of Physics, Stockholm University; ^(b) The Oskar Klein Centre, Stockholm, Sweden
- 148 Physics Department, Royal Institute of Technology, Stockholm, Sweden
- 149 Departments of Physics & Astronomy and Chemistry, Stony Brook University, Stony Brook NY, United States of America
- 150 Department of Physics and Astronomy, University of Sussex, Brighton, United Kingdom
- 151 School of Physics, University of Sydney, Sydney, Australia
- 152 Institute of Physics, Academia Sinica, Taipei, Taiwan
- 153 Department of Physics, Technion: Israel Institute of Technology, Haifa, Israel
- 154 Raymond and Beverly Sackler School of Physics and Astronomy, Tel Aviv University, Tel Aviv, Israel
- 155 Department of Physics, Aristotle University of Thessaloniki, Thessaloniki, Greece
- 156 International Center for Elementary Particle Physics and Department of Physics, The University of Tokyo, Tokyo, Japan
- 157 Graduate School of Science and Technology, Tokyo Metropolitan University, Tokyo, Japan
- 158 Department of Physics, Tokyo Institute of Technology, Tokyo, Japan
- 159 Department of Physics, University of Toronto, Toronto ON, Canada
- 160 ^(a) TRIUMF, Vancouver BC; ^(b) Department of Physics and Astronomy, York University, Toronto ON, Canada
- 161 Faculty of Pure and Applied Sciences, University of Tsukuba, Tsukuba, Japan
- 162 Department of Physics and Astronomy, Tufts University, Medford MA, United States of America
- 163 Centro de Investigaciones, Universidad Antonio Narino, Bogota, Colombia
- 164 Department of Physics and Astronomy, University of California Irvine, Irvine CA, United States of America
- 165 ^(a) INFN Gruppo Collegato di Udine, Sezione di Trieste, Udine; ^(b) ICTP, Trieste; ^(c) Dipartimento di Chimica, Fisica e Ambiente, Università di Udine, Udine, Italy

- ¹⁶⁶ Department of Physics, University of Illinois, Urbana IL, United States of America
- ¹⁶⁷ Department of Physics and Astronomy, University of Uppsala, Uppsala, Sweden
- ¹⁶⁸ Instituto de Física Corpuscular (IFIC) and Departamento de Física Atómica, Molecular y Nuclear and Departamento de Ingeniería Electrónica and Instituto de Microelectrónica de Barcelona (IMB-CNM), University of Valencia and CSIC, Valencia, Spain
- ¹⁶⁹ Department of Physics, University of British Columbia, Vancouver BC, Canada
- ¹⁷⁰ Department of Physics and Astronomy, University of Victoria, Victoria BC, Canada
- ¹⁷¹ Department of Physics, University of Warwick, Coventry, United Kingdom
- ¹⁷² Waseda University, Tokyo, Japan
- ¹⁷³ Department of Particle Physics, The Weizmann Institute of Science, Rehovot, Israel
- ¹⁷⁴ Department of Physics, University of Wisconsin, Madison WI, United States of America
- ¹⁷⁵ Fakultät für Physik und Astronomie, Julius-Maximilians-Universität, Würzburg, Germany
- ¹⁷⁶ Fachbereich C Physik, Bergische Universität Wuppertal, Wuppertal, Germany
- ¹⁷⁷ Department of Physics, Yale University, New Haven CT, United States of America
- ¹⁷⁸ Yerevan Physics Institute, Yerevan, Armenia
- ¹⁷⁹ Centre de Calcul de l'Institut National de Physique Nucléaire et de Physique des Particules (IN2P3), Villeurbanne, France
- ^a Also at Department of Physics, King's College London, London, United Kingdom
- ^b Also at Institute of Physics, Azerbaijan Academy of Sciences, Baku, Azerbaijan
- ^c Also at Novosibirsk State University, Novosibirsk, Russia
- ^d Also at TRIUMF, Vancouver BC, Canada
- ^e Also at Department of Physics, California State University, Fresno CA, United States of America
- ^f Also at Department of Physics, University of Fribourg, Fribourg, Switzerland
- ^g Also at Departamento de Física e Astronomia, Faculdade de Ciências, Universidade do Porto, Portugal
- ^h Also at Tomsk State University, Tomsk, Russia
- ⁱ Also at CPPM, Aix-Marseille Université and CNRS/IN2P3, Marseille, France
- ^j Also at Università di Napoli Parthenope, Napoli, Italy
- ^k Also at Institute of Particle Physics (IPP), Canada
- ^l Also at Particle Physics Department, Rutherford Appleton Laboratory, Didcot, United Kingdom
- ^m Also at Department of Physics, St. Petersburg State Polytechnical University, St. Petersburg, Russia
- ⁿ Also at Louisiana Tech University, Ruston LA, United States of America
- ^o Also at Institutio Catalana de Recerca i Estudis Avancats, ICREA, Barcelona, Spain
- ^p Also at Department of Physics, National Tsing Hua University, Taiwan
- ^q Also at Department of Physics, The University of Texas at Austin, Austin TX, United States of America
- ^r Also at Institute of Theoretical Physics, Ilia State University, Tbilisi, Georgia

- ^s Also at CERN, Geneva, Switzerland
- ^t Also at Georgian Technical University (GTU), Tbilisi, Georgia
- ^u Also at Ochanomizu Academic Production, Ochanomizu University, Tokyo, Japan
- ^v Also at Manhattan College, New York NY, United States of America
- ^w Also at Institute of Physics, Academia Sinica, Taipei, Taiwan
- ^x Also at LAL, Université Paris-Sud and CNRS/IN2P3, Orsay, France
- ^y Also at Academia Sinica Grid Computing, Institute of Physics, Academia Sinica, Taipei, Taiwan
- ^z Also at School of Physics, Shandong University, Shandong, China
- ^{aa} Also at Dipartimento di Fisica, Sapienza Università di Roma, Roma, Italy
- ^{ab} Also at Moscow Institute of Physics and Technology State University, Dolgoprudny, Russia
- ^{ac} Also at Section de Physique, Université de Genève, Geneva, Switzerland
- ^{ad} Also at International School for Advanced Studies (SISSA), Trieste, Italy
- ^{ae} Also at Department of Physics and Astronomy, University of South Carolina, Columbia SC, United States of America
- ^{af} Also at School of Physics and Engineering, Sun Yat-sen University, Guangzhou, China
- ^{ag} Also at Faculty of Physics, M.V.Lomonosov Moscow State University, Moscow, Russia
- ^{ah} Also at National Research Nuclear University MEPhI, Moscow, Russia
- ^{ai} Also at Department of Physics, Stanford University, Stanford CA, United States of America
- ^{aj} Also at Institute for Particle and Nuclear Physics, Wigner Research Centre for Physics, Budapest, Hungary
- ^{ak} Also at Department of Physics, Oxford University, Oxford, United Kingdom
- ^{al} Also at Department of Physics, The University of Michigan, Ann Arbor MI, United States of America
- ^{am} Also at Discipline of Physics, University of KwaZulu-Natal, Durban, South Africa
- ^{an} Also at University of Malaya, Department of Physics, Kuala Lumpur, Malaysia
- * Deceased